Topology Optimization of 2D Elastic Structures Using Boundary Elements

Luis Carretero Neches[1] and Adrián P. Cisilino[2]

[1]Group of Elasticity and Strength of Materials, Department of Continuum Mechanics
Industrial Engineering School, University of Seville
Avda. de los Descubrimientos s/n, E-41092, Seville, Spain

[2]Welding and Fracture Division, Faculty of Engineering, University of Mar del Plata
Av. Juan B. Justo 4302
7600 Mar del Plata, Argentina
email: cisilino@fi.mdp.edu.ar

Keywords: topology optimization, topological derivative, boundary elements, elasticity

Abstract. Topological Optimization provides a powerful framework to obtain the optimal domain topology for several engineering problems. The Topological Derivative is a function which characterizes the sensitivity of a given problem to the change of its topology, like opening a small hole in a continuum or changing the connectivity of rods in a truss. A numerical approach for the topological optimization of 2D linear elastic problems using Boundary Elements is presented in this work. The formulation of the problem is based on recent results which allow computing the topological derivative from strain and stress results. The Boundary Element analysis is done using a standard direct formulation. Models are discretized using linear elements and a periodic distribution of internal points over the domain. The total potential energy is selected as cost function. The evaluation of the topological derivative at internal points is performed as a post-processing procedure. Afterwards, material is removed from the model by deleting the internal points with the lowest values of the topological derivate. The new geometry is then remeshed using a weighted Delaunay triangularization algorithm capable of detecting "holes" at those positions where internal points have been removed. The procedure is repeated until a given stopping criteria is satisfied. The proposed strategy proved to be flexible and robust. A number of examples are solved and results are compared to those available in the literature.

Introduction

Structural optimization is a major concern in the design of mechanical systems. The classical problem in engineering design consists in finding the optimum geometric configuration of a body that maximizes or minimizes a given cost function while it satisfies the problem boundary conditions. During the last twenty years a number of numerical techniques have been developed to solve the problem efficiently [1].

The topological derivative provides an alternative approach for classical shape optimization methods. It was firstly introduced by Ceá et al. [2] by combining a fixed point method with the natural extension of the classical shape gradient. The basic idea behind the topological derivative is the evaluation of cost function sensitivity to the creation of a hole. In this way, wherever this sensitivity is low enough (or high enough depending on the nature of the problem) the material can be progressively eliminated. Topological derivative methods aim to solve the aforementioned limitations of the homogenization methods.

A numerical approach for the topological optimization of 2D elastic problems using Boundary Elements is presented in this work. The formulation of the problem is based on the results by Novotny et al. [3], who introduced a new procedure for computing the topological derivative which allows overcoming some mathematical difficulties involved in its classical definition. The boundary element analysis is done using a standard direct formulation. Models are discretized using linear elements and a periodic distribution of internal points over the domain. The total strain energy is selected as cost function. Afterwards, material is removed from the model by deleting the internal points with the lowest (or highest) values of the topological derivate. The new geometry is remeshed using an Extended Delaunay Tessellation algorithm capable of detecting "holes" at those positions where internal points and nodes have been removed. In this way, the procedure avoids using intermediate densities, the classical limitation of the homogenization methods. The

procedure is repeated until a given stopping criteria is satisfied. The performance of the proposed strategy is illustrated for a number of examples and their results compared to solutions available in the literature.

Topological Sensitivity Analysis

The original definition of the topological derivative, D_T, relates the sensitivity of a cost function $\psi(\Omega)$ when the topology of the optimization domain Ω is altered by creating a small cavity or hole. However, the direct application and implementation of this concept is not straightforward, as it is not possible to establish a homeomorphism between the domains with different topologies (domains with and without the hole).
Novotny et al [3,4] proposed an alternative definition of the D_T that overcomes the problem. They assimilated the creation of a hole to the perturbation of a pre-existing hole whose radius tends to zero (see Figure 1). Therefore, both topologies of the optimization domain Ω are now similar and it is possible to establish a homeomorphism between them. According to this new definition, the expression for the D_T is

$$D_T(x) = \lim_{\substack{\varepsilon \to 0 \\ \delta\varepsilon \to 0}} \frac{\psi(\Omega_{\varepsilon+\delta\varepsilon}) - \psi(\Omega_\varepsilon)}{f(\varepsilon+\delta\varepsilon) - f(\varepsilon)} \tag{1}$$

where $\psi(\Omega_\varepsilon)$ and $\psi(\Omega_{\varepsilon+\delta\varepsilon})$ are the cost function evaluated for the reference and perturbed domain, ε is the initial radius of the hole, $\delta\varepsilon$ is a small perturbation of the hole radius and f is a regularization function. The function f is problem dependent and $f(\varepsilon) \to 0$ when $\varepsilon \to 0$.
It could be argued that the new definition of the D_T in equation (1) merely provides the sensitivity of the problem when the size of the hole is perturbed and not when it is effectively created (as one has in the original definition of the topological derivative). However, it is understood that to expand a hole of radius ε, when $\varepsilon \to 0$, is nothing more than creating it. The advantage of the novel definition for the topological derivative given by Eq. (1) is that the whole mathematical framework developed for the shape sensitivity analysis can now be used to compute the D_T.

The Topological Derivative For Elasticity Problems

Let Ω_ε be the domain of a deformable body with a small hole with boundary ∂B_ε. The boundary $\Gamma_\varepsilon = \Gamma_N \cup \Gamma_D \cup \partial B_\varepsilon$ is submitted to a set of surface tractions $\bar{t}$ on the Neumann boundary Γ_N and displacement constraints on the Dirichlet boundary Γ_D. An homogeneous Neumann condition $\bar{t} = 0$ is imposed on the hole boundary ∂B_ε. Then, in absence of body forces the mechanical model can be described using the following variational formulation in terms of the displacement field u_ε: find u_ε such that

$$\int_{\Omega_\varepsilon} \sigma_\varepsilon(u_\varepsilon) \cdot \varepsilon_\varepsilon(w_\varepsilon)\, d\Omega_\varepsilon = \int_{\Gamma_N} \bar{t} \cdot w_\varepsilon\, d\Gamma_\varepsilon, \tag{2}$$

where w_ε is a field of admissible displacement variations which satisfies the condition $w_\varepsilon = 0$ on Γ_D; and σ_ε and ε_ε are the stress and strain fields respectively.
The boundary-value problem given in Equation (2) for the reference configuration Ω_ε, must also be satisfied in the perturbed configuration $\Omega_{\varepsilon+\delta\varepsilon}$, assuming that the external loads remain fixed during the shape change. The cost function $\psi(\Omega)$ is, in a certain way, arbitrary. For the case of elasticity problems the total strain energy can be adopted. The expression of the total strain energy for the reference domain is

$$\psi(\Omega_\varepsilon) = \frac{1}{2} \int_{\Omega_\varepsilon} \sigma_\varepsilon(u_\varepsilon) \cdot \varepsilon_\varepsilon(u_\varepsilon)\, d\Omega_\varepsilon - \int_{\Gamma_N} \bar{t} u_\varepsilon\, d\Gamma_\varepsilon \tag{3}$$

where the domain integral in the right hand side represents the total strain energy stored in the body and the boundary integral represents the external work. This objective function is equivalent to optimize the mean compliance of the problem.

The optimization problem can be stated as the minimization of the total potential energy (3) with the weak (variational) form of the state equations for the reference and perturbed configurations (see equation 2) as constraints. All these three equations can be used to derive the expression for the D_T using equation (1). This result was obtained by Novotny et al [3] using Reynold's transport theorem and the concept of material derivatives of spatial fields. Then from the asymptotic analysis when $\varepsilon \to 0$ the final expression for the D_T in the original domain Ω (without the hole) are obtained:

$$D_T(x) = \frac{2}{1+\nu}\boldsymbol{\sigma}\cdot\boldsymbol{\varepsilon} + \frac{3\nu-1}{2\left(1-\nu^2\right)} tr\boldsymbol{\sigma}\, tr\boldsymbol{\varepsilon} \tag{4}$$

for plane stress. A similar expression is obtained for the plane strain condition.

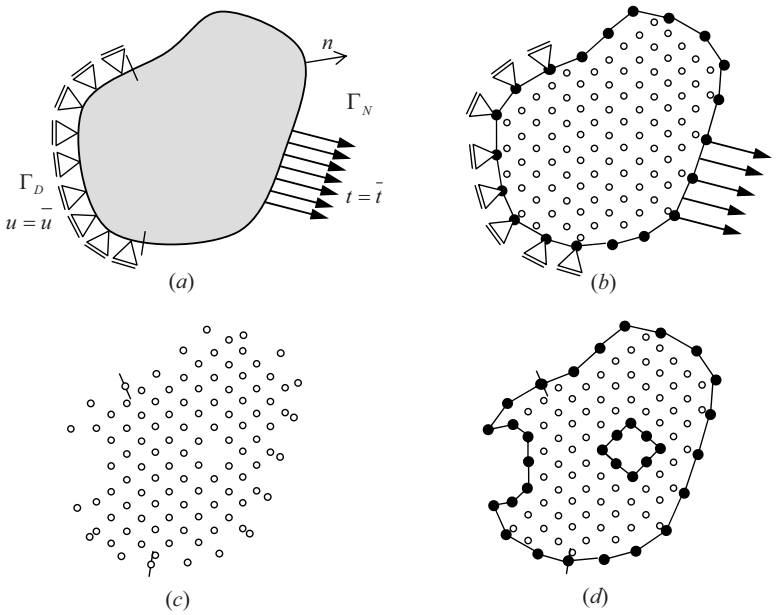

Figure 2: BEM implementation: (*a*) Problem definition and boundary conditions, (*b*) Initial BEM model, (*c*) Elimination internal points, (*d*) BEM model remeshing.

BEM Implementation

The implemented algorithm solves the optimization problem incrementally, by progressively removing a small portion of the domain per increment (usually known as *hard kill* algorithm [5]). In addition to the constrains mentioned in the previous section, it is necessary to consider some additional constraint in the problem in order to avoid that the algorithm leads merely to the trivial solution of the problem, i.e. the complete extinction of the optimization domain. The simple way used in this work to tackle this problem

consists in introducing a stopping criteria consisting in a goal minimum material volume fraction $\gamma_{\min} = \frac{vol\left(\Omega^{final}\right)}{vol\left(\Omega^{0}\right)}$.

The algorithm can be summarized as follows (the index j stands for increment number):

i. Provide an initial domain $\Omega^{j=0}$ and the stopping criterion (Figure 1*a*).
ii. Solve the BEM model for the Ω^{j} domain (Figure 1*b*). Compute the stress $\boldsymbol{\sigma}$ and strain $\boldsymbol{\varepsilon}$ fields at internal and boundary points.
iii. Compute the $D_T\left(x\right)$ using expression (4)
iv. Select the points with the minimum values of D_T (a few percent of the total number of points)
v. Create holes by removing the points selected in step iv (Figure 1*c*).
vi. Check stopping criterion. If necessary, make $j = j+1$, define a new domain Ω^{j}, remesh the BEM model (Figure 1*d*) and go to step ii.
vii. At this stage the desired final topology is obtained.

The model discretization and remeshing strategies are key issues for the performance of the implemented algorithm. The initial BEM model is discretized using two-node linear elements and a regular array of internal points following the pattern depicted in Figure 1*b*. The removal of internal and boundary points in every increment is followed by a model remeshing. With this purpose the program MeshSuite, based on an α-shapes algorithm is employed [6]. Alpha shapes can be viewed as Delaunay triangularization of a point set weighted by the parameter α. Alpha shapes formalize the intuitive notion of shape, and for varying parameter α, it ranges from crude to fine shapes. The most crude shape is the convex hull itself, which is obtained for very large values of α. As α decreases, the shape shrinks and develops cavities that may join to form holes. In this work the parameter α is selected as the average distance between boundary nodes. This is the reason why internal points are distributed on the model domain using a regular array.

Example

This first validation example consists in the short cantilever beam illustrated in Figure 3 (dotted lines). The optimization domain is a square of size $10m \times 10m$, discretized using 400 boundary elements and 9801 internal points following the pattern shown in Figure 1*b*. The left side of the domain was fixed (zero displacement boundary condition) and a total vertical load $P = 40\ N$ was applied at the middle of the right side. The specified minimum material volume fraction is $\gamma_{\min}$=0.2. The problem was solved removing 5%, 1% and 0.2% of the initial model volume in every increment.

Figure 4 displays the evolution of the normalized cost function in terms of the material volume fraction for all the three material removal rates. Besides, Figure 3 illustrates the corresponding intermediate results and the final optimized geometries. The results in Figure 4 allow verifying the convergence of the optimization scheme. The three sets of results obtained using the constant method show that the overall value of cost function diminishes with the reduction of the amount of material removed per increment. At the same time it can be seen that the three sets of results behave similarly up the volume fraction $\gamma \approx 0.50$ and then they start diverging. In essence, the 5% solution starts producing more "expensive" results when compared to 1% and 0.2% removal rates. This observation is in accordance with the geometries illustrated in Figure 3. The intermediate results show that the 1% and 0.2% geometries respond to the same basic design: two principal ">-shape" structures connected by auxiliary beams (see Figures 3*b*-1 and *c*-1), while the 5% approach produced a different design consisting in a single exterior ">-shape" structure with an internal regular lattice (see Figure 3*a*-1). Similarly, the final geometries resulting from the 1% and 0.2% solutions are almost identical (see Figures 3*b*-2 and *c*-2), and they present a significant improvement in terms of the cost-function minimization when compared to the 5% solution (see Figure 4).

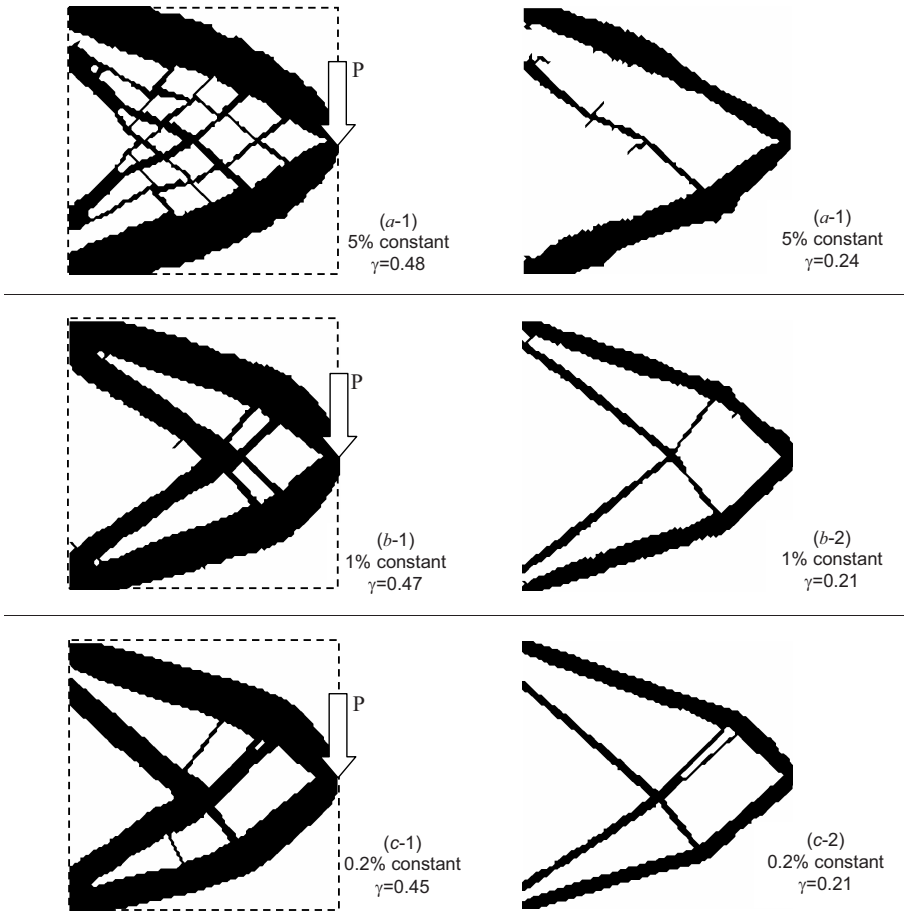

Figure 3: Intermediate and final geometries computed using different material removal rates with the constant method.

Conclusions

An effective BEM implementation for the topological optimization of 2D elastic structures was presented in this work. The optimization problem is solved incrementally, by progressively removing a small portion of the domain per increment. BEM models are discretized using linear elements and a regular array of internal points. The topological derivative is computed at boundary nodes and internal points from the strain and stress results. In every step the material removal is done by deleting those internal points and/or boundary nodes with the lowest values of the topological derivative. The material removal is followed by a model remeshing which consists in weighted Delaunay triangularization algorithm and a checking procedure devised to avoid the occurrence of invalid BEM models. The process is repeated until the given stopping criterion (the goal minimum material volume fraction) is achieved. The proposed method proves to be efficient and robust. Its performance is assessed by solving a benchmark problem.

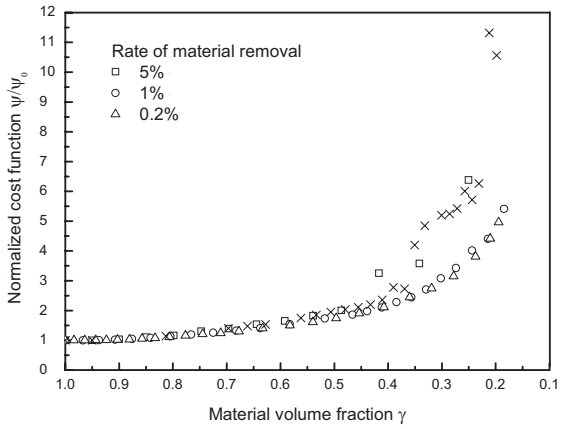

Figure 4: Example 1: evolution of the normalized cost functions in terms of the material volume fraction.

Acknowledgements

This work has been supported by the Agencia de Promoción Científica de la República Argentina under grants PICT 12-12528 and PICT 12-14114 and the ALFA Project ELBENET "Europe-Latin America Boundary Element Network" sponsored by the European Union.

References

[1] Ceá J., Garreau S., Guillaume P. and Masmoudi M. The shape and topological optimization conection. *Comput. Methods Appl. Engrg.*, 188, 713-726 (2000)

[2] Ceá J., Gioan A., and Michel J. Adaptation de la méthode du gradient a a un probleme d'idenfification de domaine. In : *Lectures Notes in Computer Science*, Vol. 11, 371-402, Springer, Berlín (1974)

[3] Novotny A.A, Feijoo R.A., Taroco E. and Padra C. C. Topological sensitivity analysis. Comput. Methods Appl. Mech. Engrg., 192, pp. 803-829 (2003)

[4] Novotny A.A, Feijoo R.A., Padra C. C. and Taroco E. The topological-shape sensitivity analysis and its applications in optimal design. *Mecanica Computacional XXI*. Proceeding of the First South American Congress on Computational Mechanics. S.R. Idelsohn, V.E. Sonzogni and A. Cardona (Eds.), Santa Fe, Argentina, 2002.

[5] Eschenauer H.A. and Olhoff N. Topology optiomization of continuum structures: a review. *Appl. Mech. Rev.,* 54, pp. 331-390 (2001)

[6] Calvo N, Idelsohn S.R. and Oñate E. The extended Delaunay tessellation. *Engineering Computations*, 20/5-6 (2003)

Axisymmetric Acoustic Modeling by the BEM: Analytical Time Integration

A. Warszawski, D. Soares Jr. and W.J. Mansur

Department of Civil Engineering, COPPE – Federal University of Rio de Janeiro,
CP 68506, CEP 21945-970, Rio de Janeiro, RJ, Brasil. E-mail: webe@coc.ufrj.br

Keywords: Boundary Element Method; Acoustics; Scalar Wave Equation; Analytical Time Integration.

Abstract. In the present work, a numerical time-domain approach to model acoustic wave propagation in axisymmetric media is developed. The acoustic medium is modeled by the Boundary Element Method, whose time integrals are evaluated analytically, employing the concept of finite part integrals. Some applications are presented in order to demonstrate the validity of the analytical expressions generated for the BEM, and the results obtained with the present approach are compared with those generated by applying numerical time integration.

Introduction

Initially, boundary element procedures were developed to consider axisymmetric acoustic wave propagation considering only frequency-domain formulations [1,2,3]. In time-domain BEM modeling, numerical integrations of 3D fundamental solutions around an axis of axisymmetry were among the first approaches developed [4,5]. In a recent work, Czygan and von Estorff [6] presented a procedure where integration of the 3D fundamental solution around the axis of axisymmetry is carried out analytically, thus obtaining the axisymmetric fundamental solution. The time integration of the resulting expressions, however, was evaluated numerically. In the present work, these integrals are evaluated analytically, generating expressions that are numerically integrated, latter on, along the discretizated boundary. In some cases, the concept of finite part integrals, introduced by Hadamard [7] and used by Mansur and Carrer [8] to perform analytical integration of bi-dimensional kernels, is required. The superior performance of the expressions derived from analytical time integration is confirmed by a numerical example presented at the end of the paper.

Time-Domain Boundary Element Formulation

The time-domain BEM system of equations that models the acoustic wave propagation through axisymmetric media is given by:

$$\mathbf{C}\mathbf{P}^{n+1} = \sum_{m=1}^{n+1}\left(\mathbf{G}^{(n+1)m}\mathbf{Q}^{m} - \mathbf{H}^{(n+1)m}\mathbf{P}^{m}\right) \tag{1}$$

where **C** is a geometrical matrix, **G** and **H** are influence matrices and **P** and **Q** are the variables of the problem (pressure and flux, for instance). The index *n* stands for the time-step of analysis. The expressions for the influence matrices are given by:

$$G_{ij}^{(n+1)m} = \int_{\Gamma}\eta_G^j(X)x_1(X)\int_0^{t_{n+1}} p^*(X,t_{n+1};\xi_i,\tau)\phi_G^m(\tau)\,d\tau\,d\Gamma_{axi} \tag{2a}$$

$$H_{ij}^{(n+1)m} = \int_{\Gamma}\eta_H^j(X)x_1(X)\int_0^{t_{n+1}} q^*(X,t_{n+1};\xi_i,\tau)\phi_H^m(\tau)\,d\tau\,d\Gamma_{axi} \tag{2b}$$

where η_G^j and η_H^j are spatial interpolation functions (both assumed linear in the present work) and ϕ_G^m and ϕ_H^m are time interpolation functions (assumed piecewise constant and linear, respectively). The source and field points are represented by ξ and *X*, respectively. The coordinates of the field point are described by x_1

(coordinate perpendicular to the axis of axisymmetry) and x_2. p^* and q^* stand for the fundamental solution of the problem (the expressions for p^* and q^* can be found in [6,9]).

Taking into account the properties of functions ϕ_G (piecewise constant) and ϕ_H (linear), as well as the translation property, which indicates that time integrals have to be calculated only along a initial time interval ($t_1 \le \tau \le t_2$), since other terms are already known through calculations performed in previous steps, the time integrals presented in equations (2) can be evaluated analytically as follows :

$$g\ (X,\xi,t_{n+1}) = \int_{t_i}^{t_f} p^*(X,t_{n+1};\xi_i,\tau)\,\phi_G(\tau)\,d\tau = E_0\,/(2d\pi^2) \tag{3a}$$

$$h_i\ (X,\xi,t_{n+1}) = \int_{t_i}^{t_f} q^*(X,t_{n+1};\xi_i,\tau)\,\phi_H^i(\tau)\,d\tau = +\left[2C_1(u_iE_1 - E_2) - C_2(u_iE_3 - E_4)\right]/(c\Delta t\pi^2) \tag{3b}$$

$$h_f(X,\xi,t_{n+1}) = \int_{t_i}^{t_f} q^*(X,t_{n+1};\xi_i,\tau)\,\phi_H^f(\tau)\,d\tau = -\left[2C_1(u_fE_1 - E_2) - C_2(u_fE_3 - E_4)\right]/(c\Delta t\pi^2) \tag{3c}$$

where c is the medium wave propagation velocity, Δt is the selected time-step and d is the greatest distance (the shortest distance is r) between the field point and the source ring generated by the rotation of the source point located on the axisymmetric (X_1, X_2) plane (see Fig.1).

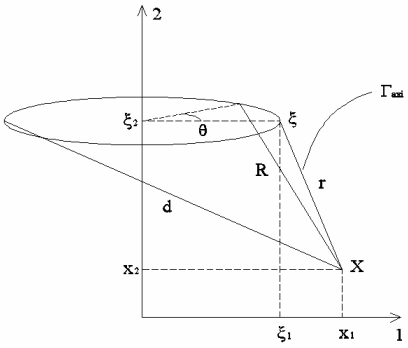

Fig.1 – Geometrical description of the axisymmetric problem

The expressions for $u_{i/f}$, C_1 and C_2 are given by:

$$u_m = c(t_n - t_m) \tag{4}$$

$$C_1 = \left[n_1(x_1 - \xi_1) + n_2(x_2 - \xi_2)\right]x_1\xi_1 \tag{5a}$$

$$C_2 = \left[n_1x_1 + n_2\left(x_2 - \xi_2\right)\right] \tag{5b}$$

where x_m, ξ_m and n_m are the coordinates of the field, source and outward unit vector normal to the boundary, respectively (see Fig.1). The expressions for E_m (see equations (3)) are presented in Table 1, according to the six possible configuration cases. For more details concerning the analytical deduction of equations (3), the reader is referred to [9].

CASE		E_0	E_1	E_2	E_3	E_4
1	$r > u_i$	0	0	0	0	0
2	$r > u_f$ $d > u_i \geq r$	F_A^i	$V_B^i +$ $+ v_B F_A^i - v_A E_A^i$	V_B^i	$V_C^i / u_i +$ $+ v_C (F_A^i - E_A^i)$	V_C^i
3	$r > u_f$ $u_i \geq d$	K_D	$v_B K_D - v_A E_C^i$	0	$v_C (K_D - E_D)$	0
4	$u_f > r$ $d > u_i$	$F_A^i - F_A^f$	$V_B^i - V_B^f +$ $+ v_B (F_A^i - F_A^f) +$ $+ v_A (E_A^f - E_A^i)$	$V_B^i - V_B^f$	$V_C^i / u_i - V_C^f / u_f +$ $+ v_C (F_A^i - F_A^f) +$ $+ v_C (E_A^f - E_A^i)$	$V_C^i - V_C^f$
5	$d > u_f \geq r$ $u_i \geq d$	F_B^i	$- u_f V_A^f +$ $+ v_B F_B^i - v_A E_B^i$	$- V_B^f$	$- u_f V_C^f / d^2 +$ $+ v_C (F_B^f - E_B^f)$	$- V_C^f$
6	$u_f > d$	0	0	0	0	0

Table 1 – Final expressions for E_m

The variables adopted in Table 1 are given by:

$$\Lambda_A^m = \Lambda\left((d/u_m)\sqrt{(u_m^2 - r^2)/(d^2 - r^2)}, \sqrt{(d^2 - r^2)}/d\right) \tag{6a}$$

$$\Lambda_B^m = \Lambda\left((d/u_m)\sqrt{(d^2 - u_m^2)/(d^2 - r^2)}, \sqrt{(d^2 - r^2)}/d\right) \tag{6b}$$

$$\Lambda_C^m = \Lambda\left((d/u_m)\sqrt{(u_m^2 - r^2)/(d^2 - r^2)}\right) \tag{6c}$$

$$\Lambda_D^m = \Lambda\left(\sqrt{(d^2 - r^2)}/d\right) \tag{6d}$$

$$V_A^m = \left[r^2(u_m^2 - r^2) - d^2(d^2 - u_m^2)\right]\left[(d^2 - r^2)d^2 r^2 \sqrt{(d^2 - u_m^2)(u_m^2 - r^2)}\right]^{-1} \tag{7a}$$

$$V_B^m = \left[(u_m^2 - r^2) - (d^2 - u_m^2)\right]\left[(d^2 - r^2)\sqrt{(d^2 - u_m^2)(u_m^2 - r^2)}\right]^{-1} \tag{7b}$$

$$V_C^m = \sqrt{(u_m^2 - r^2)}\left[(d^2 - r^2)\sqrt{(d^2 - u_m^2)}\right]^{-1} \tag{7c}$$

$$v_A = (d^2 + r^2)\left[(d^2 - r^2)^2 d\, r^2\right]^{-1} \tag{8a}$$

$$v_B = 2\left[(d^2 - r^2)^2 d\right]^{-1} \tag{8b}$$

$$v_C = \left[(d^2 - r^2) d\right]^{-1} \tag{8c}$$

where Λ (equations (6)) may represent F (meaning incomplete elliptic integral of the first kind), K (meaning complete elliptic integral of the first kind) or E (meaning complete or incomplete elliptic integral of the second kind) in Table 1.

Numerical Application

In this section, the wave propagation through a prismatic circular rod is analyzed. The rod is subjected to non-null natural boundary condition at one of its extremities and to null essential boundary condition at the opposite end. The rod dimensions are: $a = 6m$, $b = 12m$ and $c = 1m$ (see Fig.2). A unitary Heaviside function describes the prescribed flux along time. Boundary elements measuring $\ell = 1.5m$ are employed to discretize the axisymmetric boundary, composing a 24-element mesh. The acoustic wave propagation velocity of the medium is $1.0m/s$. The time discretization is selected according to an adopted β parameter ($\beta = c\Delta t / \ell$).

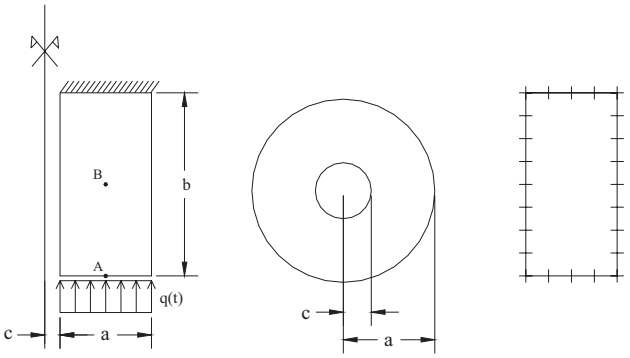

Fig.2 – Sketch of the model: axisymmetric boundary; transversal section; and BEM mesh.

Time history responses at points A and B (see Fig.2) are depicted in Fig.3, considering three different β values. Numerical results are compared with the corresponding analytical solution [10]. As one may observe, instabilities may occur considering the standard BEM time-marching procedure. In order to eliminate the instabilities, the θ-method presented by Yu *et al*. [11], is here adopted as an alternative time-marching scheme.

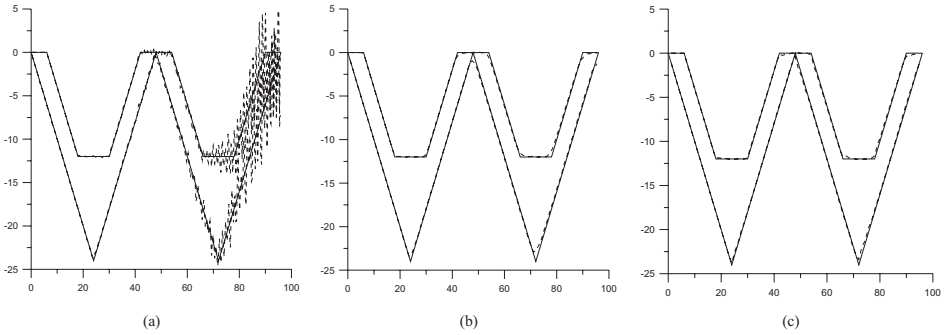

Fig.3 – Comparison between numerical (dot line) and analytical (continuous line) results (pressure *x* time) for points A and B: (a) $\beta = 0.2$; (b) $\beta = 0.6$; (c) $\beta = 0.8$.

In Fig.4, the analytical time integration procedure presently developed is compared with the numerical time integration procedure, implemented by the first author, following the guidelines described by Czygan and von Estorff [6], with $\theta = 1.1$ and $\beta = 0.6$. Thus: (i) for integrals that assemble into the **G** matrices, the Gauss-Chebyshev quadrature is employed [12] and twenty points were used for all numerical integrations (independently of the time and source/field point relative position); (ii) for integrals that assemble into the **H** matrices, the Kutt method is employed [13] and twelve integration points were employed.

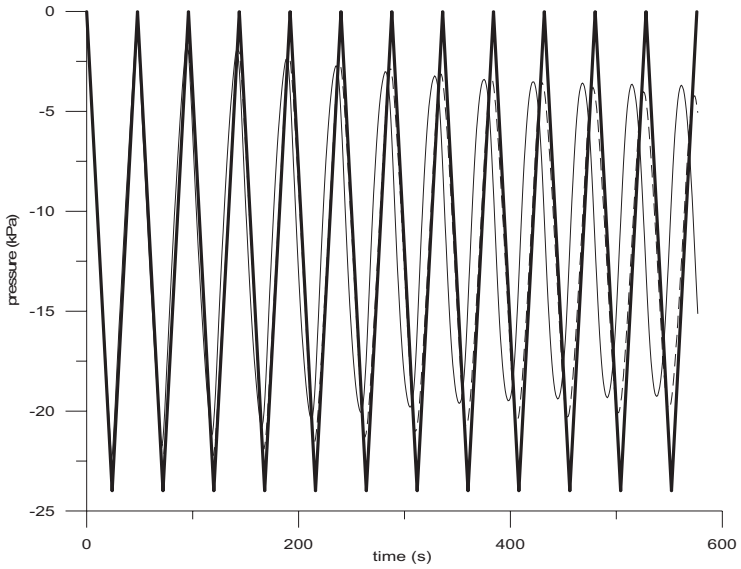

Fig.4 – Results at point A considering analytical (dashed line) and numerical (continuous line) time integration, compared with the analytical solution (thicker line)

As it can be seen, solutions obtained by analytical time integration procedures develop smaller period elongation and amplitude decay, being more accurate. This improvement is more noticeable as the analysis advances in time.

Conclusions

The present work is concerned with the time-domain formulation of the Boundary Element Method applied to model axisymmetric problems governed by the scalar wave equation. The time integrations required by the time-domain BEM approach were carried out analytically, obtaining expressions to be integrated, in the sequence, along the boundary. Singularities of boundary integrals were removed analytically and the remaining kernels were settled quite suitable for numerical integration by usual quadrature rules. The analytical time integrations produced numerical kernels, which led to results more accurate than those obtained when time integrations are carried out numerically.

References

[1] J.J.Grannell, J.J.Shirron and L.S.Couchman. A hierarchic p-version boundary–element method for axisymmetric acoustic scattering. *Journal of the Acoustical Society of America*, **5**, 2320-2329 (1994).

[2] S.V.Tsinopoulos, J.P.Agnantiaris and D.Polyzos An advanced boundary element/fast Fourier transform axisymmetric formulation for acoustic radiation and wave scattering problems. *Journal of the Acoustical Society of America*, **105**, 1517-1526 (1999).
[3] B.Soenarko. A boundary element formulation for radiation of acoustic waves from axisymmetric bodies with arbitrary boundary conditions. *Journal of the Acoustic Society of America*, **93**, 631-639 (1993).
[4] A.S.M.Israil, P.K.Banerjee and H.C.Wang. *Time-domain formulations of BEM for two-dimensional, axisymmetric and three-dimensional scalar wave propagation*. In: Advanced Dynamic Analysis by Boundary Element Method – v. 7, Chapter 3, Elsevier Applied Science: London, 75-113 (1992).
[5] D.E.Beskos. Boundary element methods in dynamic analysis. *Applied Mechanics Reviews*, **50**, 149-197 (1997).
[6] O.Czygan and O.von Estorff. An analytical fundamental solution of the transient scalar wave equation for axisymmetric systems. *Computer Methods in Applied Mechanics and Engineering*, **192**, 3657-3671 (2003).
[7] J.Hadamard. *Lecture on Cauchy's problem in linear partial differential equations*. Dover Publications: New York (1952).
[8] W.J.Mansur and J.A.M.Carrer. Two-dimensional transient BEM analysis for the scalar wave equation: kernels. *Engineering Analysis with Boundary Elements*, **12**, 283-288 (1993).
[9] A.Warszawski. *BEM-FEM coupling for axisymmetric acoustic elastodynamic problems in time domain*, M.Sc. Dissertation (in Portuguese), COPPE/UFRJ, Brazil (2005).
[10] W.Nowacki. *Dynamic of elastic systems*. John Wiley & Sons: New York (1963).
[11] G.Yu, W.J.Mansur, J.A.M.Carrer and L.Gong. A linear θ method applied to 2D time-domain BEM. *Communications in Numerical Methods in Engineering*, **14**, 1171-1179 (1998).
[12] M.Abramowitz and I.A.Stegun. *Handbook of mathematical functions with formulas, graphs and mathematical tables*. Dover Publications: New York (1968).
[13] H.R.Kutt. *Quadrature formulae for finite-part integrals*. In: CSIR Special Report WISK 178, National Research Institute for Mathematical Sciences: Pretoria (1975).

Simulating the blowing of glass containers using the boundary element method

W. Dijkstra, R.M.M. Mattheij

Department of Mathematics and Computing Science, Eindhoven University of Technology,
P.O. Box 513, 5600 MB Eindhoven, The Netherlands. e-mail: w.dijkstra@tue.nl

Keywords: Glass blowing, boundary element method, Stokes equations

Abstract. In the glass industry, an important phase in the production of bottles and jars is the blowing phase. In this phase a preform of hot liquid glass is put into a mould and blown to its final shape. Optimizing this process is costly and time-consuming and therefore a simulation tool that provides insight in the process is desirable. At each time level of the blowing phase the flow of the glass is governed by the Stokes equations. We use the Boundary Element Method to solve these equations and obtain the velocity profile at the boundary of the glass. The shape evolution of the boundary follows an ordinary differential equation. We use an Euler forward or a modified Heun method to perform a time integration step and update the shape of the glass. The main challenge is to perform all calculations in three dimensions and simulate the blowing of bottles and jars that do not have any symmetry property. Another challenge is to model and implement the contact between glass and mould. In this paper we use a partial-slip condition at the contact area. Currently we have results from several simulations on model glass containers.

Introduction

The industrial production of glass bottles and jars consists of several phases. First an amount of hot liquid glass, the *gob*, falls into a mould that is open from above. A plunger is pushed into the mould, shaping the glass to an intermediate form called the *parison*. This phase of the production process is called the *pressing phase* (Figure 1(a)). The parison is put into a second mould in which it is allowed to creep in vertical direction (*sagging*) due to gravity for a short period. Then the parison is blown to its final shape by pressurized air. This phase of the production process is called the *blowing phase* (Figure 1(b)).

For the glass industry it is important to optimize each phase of the production process. One can think of optimizing the shape of the parison, the speed of the plunger, the sagging time, the pressure of the air during the blowing phase, etc [1]. Experiments to tune these parameters are cumbersome, costly and time consuming. Therefore computer simulation of the various production phases can offer useful information to optimize the production.

In this paper we study the flow of the glass during the blowing phase. We are given the shape of the parison and the shape of the mould. The pressure of the pressurized air is prescribed. The Boundary Element Method (BEM) computes the flow at the boundary of the glass at a certain time level. Then we use an Euler forward scheme for time integration yielding the shape of the glass at the next time level.

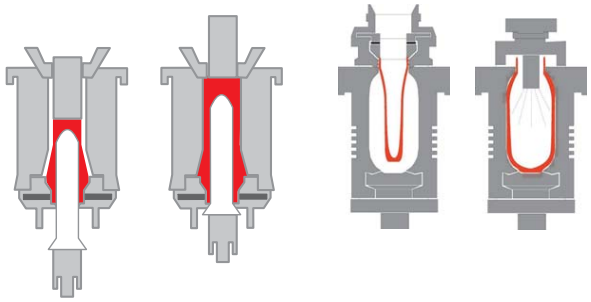

(a) *Pressing phase* (b) *Blowing phase*

Figure 1: *The production of glass containers consists of a pressing phase and a blowing phase.*

Numerical modelling of the production process of glass bottles and jars has been the topic of several papers. Mostly finite elements are used to simulate the glass blowing [2, 3], sometimes using a level set method to track the position of the glass boundary [4]. In many cases rotationally symmetric parisons are modelled and computations are limited to two dimensions. To the authors knowledge our paper is the first to address the blowing problem in three dimensions using the BEM.

During the blowing phase the temperature of the glass changes due to heat exchange with the mould. The viscosity of the glass depends on the temperature in an essentially non-linear way. Hence the heat problem and the flow problem are coupled. In the papers mentioned above this phenomenon is studied intensively. In our paper we assume a homogeneous temperature that remains constant during the whole blowing phase.

Special attention has to be given to the contact problem of the glass and the mould. Most papers assume a no-slip condition at the mould. In practice this is not the case. Sometimes the mould is even covered with a lubricating substance to improve the slip of the glass. Therefore we choose to work with a partial-slip boundary condition instead of a no-slip boundary condition.

Equations

Let Ω be the domain of the glass parison with surface $S = \partial\Omega$. The liquid glass is a viscous fluid and its velocity $\boldsymbol{v}$ and pressure p satisfy the Stokes equations

$$\begin{aligned} \eta\nabla^2\boldsymbol{v} - \nabla p - \rho g \boldsymbol{e}_z &= \boldsymbol{0}, \\ \nabla.\boldsymbol{v} &= 0,\ \boldsymbol{x} \in \Omega. \end{aligned} \tag{1}$$

Here η and ρ are the dynamic viscosity and density of the glass and g is the acceleration of gravity. At the surface of the glass we distinguish four different boundary conditions (see Figure 2 for a cross-sectional view). At the free boundary S_0 we set the pressure equal to the atmospheric pressure p_0 while at the boundary S_1 we set the pressure equal to the prescribed pressure p_1 of the pressurized air,

$$\begin{aligned} p &= p_0,\ \boldsymbol{x} \in S_0, \\ p &= p_1,\ \boldsymbol{x} \in S_1. \end{aligned} \tag{2}$$

At the top of the parison S_2 we assume that the glass is fixed and cannot move. Hence we set the velocity $\boldsymbol{v}$ equal to zero,

$$\boldsymbol{v} = \boldsymbol{0},\ \boldsymbol{x} \in S_2. \tag{3}$$

When a glass particle comes into contact with the wall of the mould we set a partial-slip boundary condition [5] at that point

$$\begin{aligned} (\sigma\boldsymbol{n} + \beta_m \boldsymbol{v}).\boldsymbol{t}^r &= 0, \\ \boldsymbol{v}.\boldsymbol{n} &= 0,\ \boldsymbol{x} \in S_3. \end{aligned} \tag{4}$$

Here $\boldsymbol{n}$ is the outward normal vector at a point at the surface and $\boldsymbol{t}^r$, $r = 1, 2$, are the unit tangential vectors at this point. The coefficient β_m is a friction parameter that has to be determined from experimental data. In the limit case $\beta_m \to \infty$, condition (4) amounts to a no-slip condition, whereas $\beta_m \to 0$ implies a frictionless situation. The tensor σ is the stress tensor, whose elements are given by

$$\sigma_{ij} := -p\delta_{ij} + 2\eta \left(\frac{\partial v_i}{\partial x_j} + \frac{\partial v_j}{\partial x_i} \right). \tag{5}$$

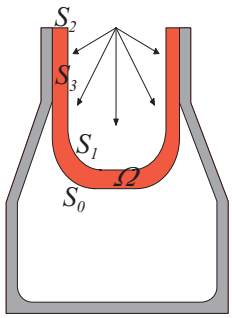

Figure 2: *A cross-section of the parison and mould. The surface of the glass can be divided into four parts.*

We choose a characteristic length scale L, and introduce dimensionless variables,

$$\boldsymbol{x}' := \frac{\boldsymbol{x}}{L}, \quad p' := \frac{p - p_0}{p_1 - p_0}, \quad \boldsymbol{v}' := \frac{\eta \boldsymbol{v}}{(p_1 - p_0)L}, \tag{6}$$

to obtain the dimensionless Stokes equations

$$\begin{aligned} \nabla^2 \boldsymbol{v}' - \nabla p' - \alpha \boldsymbol{e}_z &= 0, \\ \nabla.\boldsymbol{v}' &= 0,\ \boldsymbol{x} \in \Omega, \end{aligned} \tag{7}$$

and the boundary conditions in dimensionless notation

$$\begin{aligned} p' &= 0,\ \boldsymbol{x}' \in S_0, \qquad \left(\sigma'\boldsymbol{n} + \beta_m' \boldsymbol{v}'\right).\boldsymbol{t}^r = 0,\ \boldsymbol{x}' \in S_3, \\ p' &= 1,\ \boldsymbol{x}' \in S_1, \qquad \boldsymbol{v}'.\boldsymbol{n} = 0,\ \boldsymbol{x}' \in S_3, \\ \boldsymbol{v}' &= 0,\ \boldsymbol{x}' \in S_2. \end{aligned} \tag{8}$$

The dimensionless numbers α and β_m' are given by

$$\alpha := \frac{\rho g L}{p_1 - p_0}, \quad \beta_m' := \frac{\beta_m L}{\eta}. \tag{9}$$

Here α quantifies the effect of gravity on the flow, whereas β_m' is again the friction parameter. In the sequel we continue working with dimensionless variables but for ease of writing we omit the $'$.

In order to write the Stokes equations in a boundary integral formulation we introduce the modified pressure $\tilde{p} := p + \alpha z$ (cf. [6, p. 164]). This allows us to write the momentum balance in the Stokes equation as $\nabla^2 \boldsymbol{v} - \nabla \tilde{p} = 0$. Following the analysis of [7], the boundary integral equations for the Stokes problem read

$$\left(\frac{1}{2}\mathcal{I} + \mathcal{H}\right)\boldsymbol{v} = \mathcal{G}\boldsymbol{b}. \tag{10}$$

Here $\mathcal{G}$ and $\mathcal{H}$ are the single and double layer potential operator for the Stokes flow and are given by

$$\begin{aligned}(\mathcal{G}\boldsymbol{v})_i(\boldsymbol{x}) &:= \int_S u_{ij}(\boldsymbol{x}-\boldsymbol{y})v_j(\boldsymbol{y})dS_y,\ i=1,2,3,\\ (\mathcal{H}\boldsymbol{b})_i(\boldsymbol{x}) &:= \int_S q_{ij}(\boldsymbol{x}-\boldsymbol{y})b_j(\boldsymbol{y})dS_y,\ i=1,2,3.\end{aligned} \tag{11}$$

The vector $\boldsymbol{b}$ is the normal stress at the boundary, defined as $\boldsymbol{b} := \sigma\boldsymbol{n}$, and the kernels u_{ij} and q_{ij} are given by

$$\begin{aligned}u_{ij}(\boldsymbol{x}) &:= \frac{1}{8\pi}\left[\frac{\delta_{ij}}{\|\boldsymbol{x}\|}+\frac{x_i\,y_j}{\|\boldsymbol{x}\|^3}\right],\ i,j=1,2,3,\\ q_{ij}(\boldsymbol{x}) &:= \frac{3}{4\pi}\frac{x_i\,y_j(\boldsymbol{x}.\boldsymbol{n})}{\|\boldsymbol{x}\|^5},\ i,j=1,2,3.\end{aligned} \tag{12}$$

The boundary condition at S_2, where the velocity is set equal to zero, remains unaltered. The boundary conditions at S_0 and S_1 can be written in terms of $\boldsymbol{b}$. Taking into account the modified pressure we arrive at

$$\boldsymbol{b} = -\left(p+\alpha z\right)\boldsymbol{n},\ \boldsymbol{x}\in S_{0,1}, \tag{13}$$

where p is either zero or one. It can be seen that the slip condition at S_3 keeps the same form as in (8).

Results

The surface S is discretized with linear triangular elements. At each node of each element either the velocity $\boldsymbol{v}$ is prescribed, the normal stress $\boldsymbol{b}$, or a relation between these two. We use the BEM to find the velocity $\boldsymbol{v}$ at each node. We choose a time step size Δt and update the shape of the model with an Euler forward step,

$$\boldsymbol{x} \rightarrow \boldsymbol{x} + \Delta t\boldsymbol{v}(\boldsymbol{x}). \tag{14}$$

To improve the accuracy of the time integration we could also choose for the modifed Heun method. This method is second order accurate [8], but its drawback is that we have to solve two consecutive BEM-problems at each time level. In this paper we will only use Euler forward for time integration.

Implementing the slip condition. To process the slip condition at S_3 we express the velocity $\boldsymbol{v}$ in terms of $\boldsymbol{b}$. Since $\boldsymbol{v}.\boldsymbol{n}=0$ at a point $\boldsymbol{x}$ at S_3, we may write

$$\boldsymbol{v}(\boldsymbol{x}) = a_1\boldsymbol{t}^1(\boldsymbol{x}) + a_2\boldsymbol{t}^2(\boldsymbol{x}). \tag{15}$$

Substitution into $(\boldsymbol{b}+\beta_m\boldsymbol{v}).\boldsymbol{t}^r = 0$ yields $a_r = -(\boldsymbol{b}.\boldsymbol{t}^r)/\beta_m$. In the boundary integral equation we replace $\boldsymbol{v}(\boldsymbol{x})$ by the above expression. The solution of the BEM yields the normal stress $\boldsymbol{b}(\boldsymbol{x})$ and as a post-processing step we compute the velocity $\boldsymbol{v}(\boldsymbol{x})$ with (15).

Contact problem mould - glass. When a glass particle moves into the direction of the wall of the mould we have to ensure that it does not cross the wall. We assume that the wall is described by an algebraic equation $g(\boldsymbol{x})=0$. A glass particle at time t^n with position $\boldsymbol{x}(t^n)\in S_0$ is inside the mould when $g(\boldsymbol{x}(t^n))<0$ and outside the mould when $g(\boldsymbol{x}(t^n))>0$. In this way we can detect particles that have moved outside the mould. If we find such a particle, we relocate it at a new position at the

wall of the mould, at the imaginary line connecting $\boldsymbol{x}(t^n)$ and $\boldsymbol{x}(t^{n-1})$, the position of the particle at the previous time level. The glass particle now no longer belongs to S_0, but becomes part of S_4. By relocating the particle we inevitably lose a small amount of mass. We compute this mass and relocate the nearest glass particle at S_1 over a small distance to compensate this. To make this procedure more physically realistic we could also divide the mass over several particles at S_1 near $\boldsymbol{x}(t^n)$. At the moment we restrict ourselves to a single particle strategy.

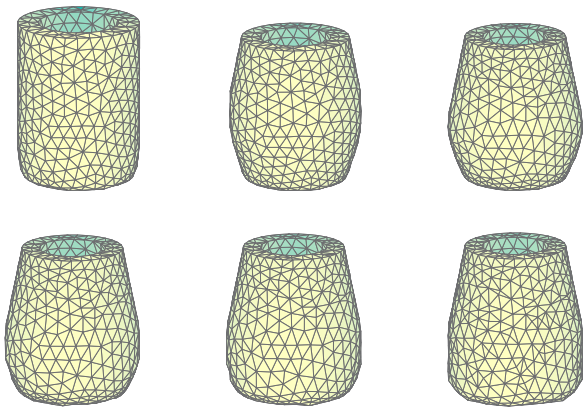

Figure 3: *A cylindrically shaped parison is blown to its final shape.*

Example. As an example we show the results of a test on a parison that consists of a cylinder with bottom. In this case both the parison and mould are rotationally symmetric but we do not exploit this in the computations. Figure 3 shows six timelevels from the blowing phase. Figure 4 gives a cross-sectional view of the test case. Here the shape of the mould is also plotted. For this example the mass change was limited to 0.46%. Since the shape evolution of the parison is rather large, we use a remesh routine that subdivides elements that are larger than a certain tolerance level. Figure 5 shows the example of blowing a drinking glass.

References

[1] C. Marechal, P. Moreau, and D. Lochegnies. Numerical optimization of a new robotized glass blowing process. *Engineering with Computers*, 19:233–240, 2004.

[2] J.M.A. César de Sá. Numerical modelling of glass forming processes. *Eng. Comput.*, 3:266–275, 1986.

[3] J.M.A. César de Sá, R.M. Natal Jorge, C.M.C. Silva, and R.P.R. Cardoso. A computational model for glass container forming processes. In *Europe Conference on Computational Mechanics Solids, Structures and Coupled Problems in Engineering*, 1999.

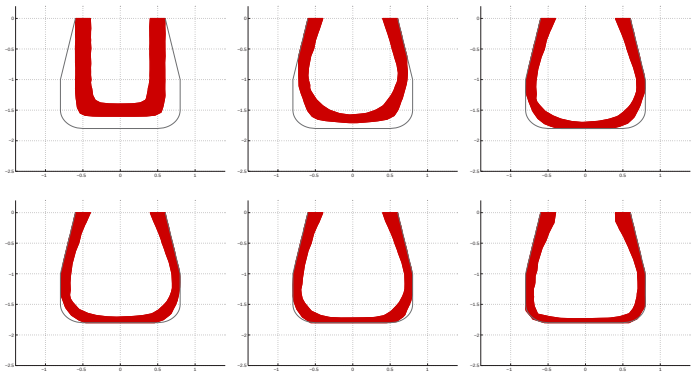

Figure 4: *A cylindrically shaped parison is blown to its final shape: cross-section view.*

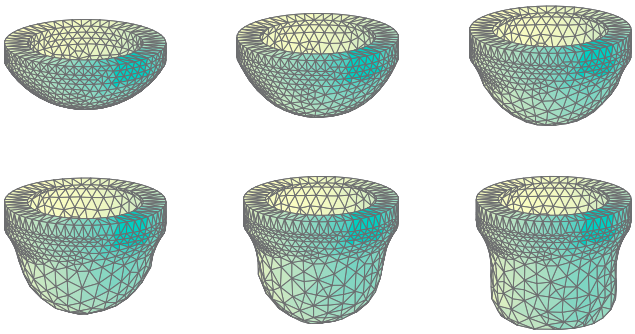

Figure 5: *Blowing of a drinking glass.*

[4] C.G. Giannopapa. Development of a computer simulation model for blowing glass containers. CASA-Report 07, Eindhoven University of Technology, 2006.

[5] V. John and A. Liakos. Time-dependent flow across a step: the slip with friction boundary condition. *Int. J. Numer. Meth. Fluids*, 50:713–731, 2006.

[6] C. Pozrikidis. *A practical guide to boundary element methods*. Chapman and Hall, Boca Raton, 2002.

[7] O.A. Ladyzhenskaya. *The Mathematical Theory of Viscous Incompressible Flow*. Gordon and Beach, New York-London, 1963.

[8] J.C. Butcher. *The numerical analysis of ordinary differential equations*. Wiley, Chichester, 1987.

Variational approaches for elastic domain decomposition problems with non-conforming discretizations of curved interfaces solved by SGBEM

Roman Vodička[1], Vladislav Mantič[2], Federico París[2]

[1] Technical University of Košice, Faculty of Civil Engineering, Department of Applied Mathematics
Vysokoškolská 4, 042 00 Košice, Slovak Republic

[2] University of Seville, School of Engineering, Group of Elasticity and Strength of Materials
Camino de los Descubrimientos s/n, 41092 Sevilla, Spain

Keywords: domain decomposition, symmetric Galerkin boundary element method, non-conforming meshes

Abstract. Two original approaches to the solution of elastic boundary value problems with domain decomposition using the Symmetric Galerkin Boundary Element Method (SGBEM) are presented. These approaches are based on two variational principles, which differ in the treatment of the coupling conditions connecting the solutions through an interface/partition surface. The novel feature of the computer codes developed is that they can deal with curved interfaces in a domain decomposition problem discretized by non-matching meshes of linear boundary elements along the interfaces. The robustness and accuracy of the two algorithms implemented are evaluated and compared by numerical examples.

Introduction

In the solution of a Boundary Value Problem (BVP) it can be useful or necessary to apply a Domain Decomposition (DD) technique to solve BVPs including multi-material or complex structures and/or contact zones, or to solve large-scale BVPs on modern parallel computers. All these applications can be treated effectively by a modern boundary element technique – SGBEM.

In the present work, two approaches to the solution of DDBVPs are developed, implemented in 2D-SGBEM codes [1,2] and compared. The variational principles established in these approaches are based on the one-domain SGBEM variational formulation introduced in [3], generalizing this formulation to DDBVPs. The definition of coupling conditions arises from a weak imposition of contact conditions proposed in [4] and adapted here to DDBVPs. The variational principles produce these conditions as a natural generalization of the classical point-wise coupling conditions, and so the developed approaches also share some ideas with the mortar element approach [5].

Although both approaches apply these coupling conditions in a weak form, the weighting functions used in each approach are different. One of them uses the displacements on one side of the interface as weighting functions for imposing the condition of equilibrium at this interface side. For the imposition of the compatibility condition tractions on the opposite side of the interface sides are used. The other approach introduces a new set of weighting functions, called Lagrange multipliers, in the coupling conditions. Using these new unknowns pushes the approach closely to the mortar element techniques. However, unlike the FEM applications, the Lagrange multipliers have the physical meaning of both displacements and tractions.

The present approaches allow curved interfaces to be discretized by non-conforming meshes, a feature still not very common in the solution of DDBVPs. Various methods for the data transfer between non-conforming meshes via calculation of integrals over the discretized curved surfaces were described in [6], one of these methods having also been used in the implementation of the present approaches.

The robustness and accuracy of the algorithms implemented have been tested on a couple of numerical examples, comparing the results of both approaches with the analytical solutions.

Domain decomposition

Let us consider a 2D elastic body defined by a domain Ω with a bounded Lipschitz boundary Γ, $\boldsymbol{n}$ denoting the outward unit normal vector on Γ. Let us consider a split of Ω into two non-overlapping parts Ω^A and Ω^B, whose respective boundaries are denoted as Γ^A and Γ^B, the common part of both boundaries being denoted by Γ_c. Considering the boundary conditions for displacements $\boldsymbol{u}^\eta$ and tractions $\boldsymbol{t}^\eta$ (η=A,B) and the

corresponding partition of the boundary Γ^η, the DDBVP for the Navier equation can be written in the form:

$$\begin{aligned} c^\eta_{ijkl}u^\eta_{k,lj}(x) = c^\eta_{ijkl}\varepsilon^\eta_{kl,j}\left(\boldsymbol{u}^\eta(x)\right) = 0, \qquad & x\in\Omega^\eta, \\ u^\eta_i(x) = g^\eta_i(x), \quad & x\in\Gamma^\eta_u, \\ t^\eta_i(x) = \left(\mathbf{T}_{\boldsymbol{n}^\eta(x)}\right)_i\left(\boldsymbol{u}^\eta(x)\right) = h^\eta_i(x), \quad & x\in\Gamma^\eta_t, \\ t^A_i(x) = -t^B_i(x), \qquad u^A_i(x) = u^B_i(x), \quad & x\in\Gamma_c, \end{aligned} \tag{1}$$

with the elastic stiffnesses c_{ijkl}, $(i,j,k,l=1,2)$, the strain tensor ε_{ij}, the traction operator $\mathbf{T}_{\boldsymbol{n}}$, and $\boldsymbol{g}^\eta$ and $\boldsymbol{h}^\eta$ the prescribed displacement and traction boundary conditions, respectively. The coupling conditions of compatibility of displacements and equilibrium of tractions through the interface are given in the last row of eq (1).

Formulation of BIEs

Variational formulation of the DDBVP in eq (1). Let us introduce a functional of energy with Lagrange multipliers:

$$E^\lambda\left(\boldsymbol{u}^\mathrm{A},\boldsymbol{u}^\mathrm{B},\boldsymbol{\lambda}_u,\boldsymbol{\lambda}_t\right) = E^A\left(\boldsymbol{u}^\mathrm{A}\right) + E^B\left(\boldsymbol{u}^\mathrm{B}\right) + E^\lambda_c\left(\boldsymbol{u}^\mathrm{A},\boldsymbol{u}^\mathrm{B},\boldsymbol{\lambda}_u,\boldsymbol{\lambda}_t\right), \tag{2}$$

which is a function of displacements $\boldsymbol{u}^A$ and $\boldsymbol{u}^B$ and of the Lagrange multipliers $\boldsymbol{\lambda}_u$ and $\boldsymbol{\lambda}_t$, physically, corresponding to some displacements and tractions at the interface. The functionals $E^\eta(\boldsymbol{u}^\eta)$ give the total energies associated to subdomains Ω^η with the exclusion of the contributions due to the interface boundary parts, writing

$$E^\eta\left(\boldsymbol{u}^\eta\right) = \tfrac{1}{2}\int_{\Omega^\eta}\varepsilon_{ij}\left(\boldsymbol{u}^\eta\right)c^\eta_{ijkl}\varepsilon_{kl}\left(\boldsymbol{u}^\eta\right)\mathrm{d}\Omega - \int_{\Gamma^\eta_t}h^\eta_i u^\eta_i\,\mathrm{d}\Gamma - \int_{\Gamma^\eta_u}t^\eta_i(u^\eta_i - g^\eta_i)\mathrm{d}\Gamma. \tag{3}$$

The functions $\boldsymbol{t}^\eta$ represent the tractions of the displacement solutions $\boldsymbol{u}^\eta$ calculated via the traction operator $\mathbf{T}_{\boldsymbol{n}}$. The last term in eq (2) introduces a form of interface energy modified by Lagrange-multipliers terms:

$$E^\lambda_c\left(\boldsymbol{u}^\mathrm{A},\boldsymbol{u}^\mathrm{B},\boldsymbol{\lambda}_u,\boldsymbol{\lambda}_t\right) = -\int_{\Gamma_c}u^B_i\left(t^A_i + t^B_i\right)\mathrm{d}\Gamma + \int_{\Gamma_c}\left(\lambda_t\right)_i\left(u^B_i - u^A_i\right)\mathrm{d}\Gamma + \int_{\Gamma_c}\left(\lambda_u\right)_i\left(t^A_i + t^B_i\right)\mathrm{d}\Gamma. \tag{4}$$

The interface functional E^λ_c introduces additional unknowns – Lagrange multipliers to explicitly set the interface conditions. As will be shown in what follows, these unknowns can be eliminated. That is, if we put $\boldsymbol{\lambda}_u$ equal to $\boldsymbol{u}^B$ and $\boldsymbol{\lambda}_t$ equal to $\boldsymbol{t}^A$, we obtain the following interface energy:

$$E^R_c\left(\boldsymbol{u}^\mathrm{A},\boldsymbol{u}^\mathrm{B}\right) = \int_{\Gamma_c}t^A_i\left(u^B_i - u^A_i\right)\mathrm{d}\Gamma, \tag{5}$$

which reduces E^λ from eq (2) to a new (reduced) energy functional $E^R(\boldsymbol{u}^A,\boldsymbol{u}^B) = E^A(\boldsymbol{u}^A) + E^B(\boldsymbol{u}^B) + E^R{}_c(\boldsymbol{u}^A,\boldsymbol{u}^B)$.

Both energy functionals introduced can be used to solve the DDBVP in eq (1), as their stationary points provide the problem solution. This can easily be deduced from the vanishing variations of both functionals:

$$\delta E^\lambda\left(\boldsymbol{u}^\mathrm{A},\boldsymbol{u}^\mathrm{B},\boldsymbol{\lambda}_u,\boldsymbol{\lambda}_t;\delta\boldsymbol{u}^\mathrm{A},\delta\boldsymbol{u}^\mathrm{B},\delta\boldsymbol{\lambda}_u,\delta\boldsymbol{\lambda}_t\right) = 0, \quad \delta E^R\left(\boldsymbol{u}^\mathrm{A},\boldsymbol{u}^\mathrm{B};\delta\boldsymbol{u}^\mathrm{A},\delta\boldsymbol{u}^\mathrm{B}\right) = 0, \tag{6}$$

with virtual functions $\delta\boldsymbol{u}^A$, $\delta\boldsymbol{u}^B$, $\delta\boldsymbol{\lambda}_u$, $\delta\boldsymbol{\lambda}_t$.

BIE formulation. We can eliminate the volume integrals in eq (3) restricting the virtual displacements to those which satisfy the Navier equation eq $(1)_1$. To this end, let us apply an integral representation, provided by the difference of the Somigliana displacement identities for interior and exterior BVPs:

$$\delta u^\eta_i(x) = \int_{\Gamma^\eta}U^\eta_{ij}(x,y)\varphi^\eta_j(y)\,\mathrm{d}_y\Gamma - \int_{\Gamma^\eta}T^\eta_{ij}(x,y)\psi^\eta_j(y)\,\mathrm{d}_y\Gamma, \quad x\in\Omega^\eta, \tag{7}$$

for some boundary functions $\boldsymbol{\varphi}^\eta(x)$ and $\boldsymbol{\psi}^\eta(x)$. U^η_{kl} is the fundamental solution of the Navier equation associated to the elastic material of Ω^η, and T^η_{kl} represents the fundamental tractions, obtained from the fundamental solution via the traction operator: $\boldsymbol{T}^\eta(x,y) = (\mathbf{T}^\eta_{\boldsymbol{n}(y)}\boldsymbol{U}^\eta(x,y))^\mathrm{T}$, and 'T' denotes the transpose matrix.

A similar representation can be introduced for the tractions associated to the virtual displacements, i.e.

$$\delta t^\eta_i(x) = \int_{\Gamma^\eta}T^{\eta^*}_{ij}(x,y)\varphi^\eta_j(y)\,\mathrm{d}_y\Gamma - \int_{\Gamma^\eta}D^\eta_{ij}(x,y)\psi^\eta_j(y)\,\mathrm{d}_y\Gamma, \quad x\in\Omega^\eta, \tag{8}$$

with $\boldsymbol{T}^\eta(x,y) = \mathbf{T}^\eta_{\boldsymbol{\nu}(x)}\boldsymbol{U}^\eta(x,y)$, $\boldsymbol{D}^\eta(x,y) = \mathbf{T}^\eta_{\boldsymbol{\nu}(x)}\boldsymbol{T}^\eta(x,y)$ and $\boldsymbol{\nu}(x)$ being the unit normal to an auxiliary curve passing through the point x where the traction is evaluated.

The integral representations in eq (7) and eq (8) can, after a standard limit-to-the-boundary process (which originates jumps in some integrals and possibly changes their meaning to weakly singular, Cauchy principal value or finite-part integrals), be substituted into eq (6), deriving (after reordering the terms, changing the integration order, and introducing an operator notation for simplicity) a matrix form of the resulting boundary integral equation systems [1,2].

Let us define a symbol for the integral operators by

$$\boldsymbol{\omega}_r^{\eta\mathrm{T}} \boldsymbol{Z}_{rs}^{\eta} \boldsymbol{w}_s^{\eta} = \int_{\Gamma_r^{\eta}} \omega_j^{\eta}(y) \left(\int_{\Gamma_s^{\eta}} Z_{ij}^{\eta}(y,x) w_i^{\eta}(x) \mathrm{d}_x\Gamma \right) \mathrm{d}_y\Gamma, \tag{9}$$

where $\boldsymbol{\omega}$ stands for $\boldsymbol{\varphi}$ or $\boldsymbol{\psi}$; $\boldsymbol{w}$ stands for $\boldsymbol{u}$ or $\boldsymbol{t}$; r, s stand for u, t or c; $\boldsymbol{Z}$ stands for $\boldsymbol{U}$, $\boldsymbol{T}$, $\boldsymbol{T}^*$ or $\boldsymbol{D}$. Recall that the inner integral can be regular, weakly singular, principal value or finite-part integral.

The boundary integral equation systems for searching for the stationary point of the functionals E^{λ} and E^{R} can be written in a matrix-operator form as:

$$\boldsymbol{\Phi}^{\mathrm{T}} \boldsymbol{A} \ \boldsymbol{X} = \boldsymbol{\Phi}^{\mathrm{T}} \boldsymbol{B} \tag{10}$$

which should be valid for any virtual vector function $\boldsymbol{\Phi}$. The form of the matrix-operators depends on the energy functional considered. For E^{λ}, the matrices in eq (10) are expressed as follows:

$$\boldsymbol{\Phi}^{\lambda\mathrm{T}} = \begin{pmatrix} \boldsymbol{\varphi}_u^A & \boldsymbol{\psi}_t^A & \boldsymbol{\varphi}_c^A & \boldsymbol{\psi}_c^A & \boldsymbol{\varphi}_u^B & \boldsymbol{\psi}_t^B & \boldsymbol{\varphi}_c^B & \boldsymbol{\psi}_c^B & \boldsymbol{\rho} & \boldsymbol{\xi} \end{pmatrix} \tag{11}$$

is the virtual vector function; the matrix representation of the operator $\boldsymbol{A}$ is

$$\boldsymbol{A}^{\lambda} = \begin{pmatrix}
-\boldsymbol{U}_{uu}^A & \boldsymbol{T}_{ut}^A & -\boldsymbol{U}_{uc}^A & \boldsymbol{T}_{uc}^A & \boldsymbol{0} & \boldsymbol{0} & \boldsymbol{0} & \boldsymbol{0} & \boldsymbol{0} & \boldsymbol{0} \\
\boldsymbol{T}_{tu}^{AT} & -\boldsymbol{D}_{tt}^A & \boldsymbol{T}_{tc}^{AT} & -\boldsymbol{D}_{tc}^A & \boldsymbol{0} & \boldsymbol{0} & \boldsymbol{0} & \boldsymbol{0} & \boldsymbol{0} & \boldsymbol{0} \\
-\boldsymbol{U}_{cu}^A & \boldsymbol{T}_{ct}^A & -\boldsymbol{U}_{cc}^A & \frac{1}{2}\boldsymbol{I}_{cc}^A + \boldsymbol{T}_{cc}^A & \boldsymbol{0} & \boldsymbol{0} & \boldsymbol{0} & -\boldsymbol{I}_{cc}^{AB} & \boldsymbol{0} & \boldsymbol{I}_{cc}^{A\lambda_u} \\
\boldsymbol{T}_{cu}^{AT} & -\boldsymbol{D}_{ct}^A & \frac{1}{2}\boldsymbol{I}_{cc}^A + \boldsymbol{T}_{cc}^{A*} & -\boldsymbol{D}_{cc}^A & \boldsymbol{0} & \boldsymbol{0} & \boldsymbol{0} & \boldsymbol{0} & -\boldsymbol{I}_{cc}^{A\lambda_t} & \boldsymbol{0} \\
\boldsymbol{0} & \boldsymbol{0} & \boldsymbol{0} & \boldsymbol{0} & -\boldsymbol{U}_{uu}^B & \boldsymbol{T}_{ut}^B & -\boldsymbol{U}_{uc}^B & \boldsymbol{T}_{uc}^B & \boldsymbol{0} & \boldsymbol{0} \\
\boldsymbol{0} & \boldsymbol{0} & \boldsymbol{0} & \boldsymbol{0} & \boldsymbol{T}_{tu}^B & -\boldsymbol{D}_{tt}^B & \boldsymbol{T}_{tc}^B & -\boldsymbol{D}_{tc}^B & \boldsymbol{0} & \boldsymbol{0} \\
\boldsymbol{0} & \boldsymbol{0} & \boldsymbol{0} & \boldsymbol{0} & -\boldsymbol{U}_{cu}^B & \boldsymbol{T}_{ct}^B & -\boldsymbol{U}_{cc}^B & -\frac{1}{2}\boldsymbol{I}_{cc}^B + \boldsymbol{T}_{cc}^B & \boldsymbol{0} & \boldsymbol{I}_{cc}^{B\lambda_u} \\
\boldsymbol{0} & \boldsymbol{0} & -\boldsymbol{I}_{cc}^{BA} & \boldsymbol{0} & \boldsymbol{T}_{cu}^B & -\boldsymbol{D}_{ct}^B & -\frac{1}{2}\boldsymbol{I}_{cc}^B + \boldsymbol{T}_{cc}^{B*} & -\boldsymbol{D}_{cc}^B & \boldsymbol{I}_{cc}^{B\lambda_t} & \boldsymbol{0} \\
\boldsymbol{0} & \boldsymbol{0} & \boldsymbol{0} & -\boldsymbol{I}_{cc}^{\lambda_t A} & \boldsymbol{0} & \boldsymbol{0} & \boldsymbol{0} & \boldsymbol{I}_{cc}^{\lambda_t B} & \boldsymbol{0} & \boldsymbol{0} \\
\boldsymbol{0} & \boldsymbol{0} & \boldsymbol{I}_{cc}^{\lambda_u A} & \boldsymbol{0} & \boldsymbol{0} & \boldsymbol{0} & \boldsymbol{I}_{cc}^{\lambda_u B} & \boldsymbol{0} & \boldsymbol{0} & \boldsymbol{0}
\end{pmatrix}; \tag{12}$$

the unknown functions are gathered in the vector function $\boldsymbol{X}$, i. e.

$$\boldsymbol{X}^{\lambda\mathrm{T}} = \begin{pmatrix} \boldsymbol{t}_u^A & \boldsymbol{u}_t^A & \boldsymbol{t}_c^A & \boldsymbol{u}_c^A & \boldsymbol{t}_u^B & \boldsymbol{u}_t^B & \boldsymbol{t}_c^B & \boldsymbol{u}_c^B & \boldsymbol{\lambda}_t & \boldsymbol{\lambda}_u \end{pmatrix} \tag{13}$$

and the given boundary data produce the vector

$$\boldsymbol{B}^{\lambda\mathrm{T}} = \begin{pmatrix} \boldsymbol{B}_A^{\mathrm{T}} & \boldsymbol{B}_B^{\mathrm{T}} & \boldsymbol{0} & \boldsymbol{0} \end{pmatrix}; \tag{14}$$

with

$$\boldsymbol{B}_{\eta}^{\mathrm{T}} = \begin{pmatrix} \boldsymbol{U}_{ut}^{\eta} \boldsymbol{h}^{\eta} - \left(\frac{1}{2}\boldsymbol{I}_{uu}^{\eta} + \boldsymbol{T}_{uu}^{\eta} \right) \boldsymbol{g}^{\eta} & \left(\frac{1}{2}\boldsymbol{I}_{tt}^{\eta} - \boldsymbol{T}_{tt}^{\eta *} \right) \boldsymbol{h}^{\eta} + \boldsymbol{D}_{tu}^{\eta} \boldsymbol{g}^{\eta} & \boldsymbol{U}_{ct}^{\eta} \boldsymbol{h}^{\eta} - \boldsymbol{T}_{cu}^{\eta} \boldsymbol{g}^{\eta} & -\boldsymbol{T}_{ct}^{\eta *} \boldsymbol{h}^{\eta} + \boldsymbol{D}_{cu}^{\eta} \boldsymbol{g}^{\eta} \end{pmatrix}, \quad \eta = A, B. \tag{15}$$

Similarly, we can represent the operators of the (reduced) energy functional E^{R}. The virtual vector function writes as

$$\boldsymbol{\Phi}^{R\mathrm{T}} = \begin{pmatrix} \boldsymbol{\varphi}_u^A & \boldsymbol{\psi}_t^A & \boldsymbol{\varphi}_c^A & \boldsymbol{\psi}_c^A & \boldsymbol{\varphi}_u^B & \boldsymbol{\psi}_t^B & \boldsymbol{\varphi}_c^B & \boldsymbol{\psi}_c^B \end{pmatrix}; \tag{16}$$

the matrix representation of the operator $\boldsymbol{A}^{R}$ is

$$\boldsymbol{A}^{R} = \begin{pmatrix}
-\boldsymbol{U}_{uu}^A & \boldsymbol{T}_{ut}^A & -\boldsymbol{U}_{uc}^A & \boldsymbol{T}_{uc}^A & \boldsymbol{0} & \boldsymbol{0} & \boldsymbol{0} & \boldsymbol{0} \\
\boldsymbol{T}_{tu}^{AT} & -\boldsymbol{D}_{tt}^A & \boldsymbol{T}_{tc}^{AT} & -\boldsymbol{D}_{tc}^A & \boldsymbol{0} & \boldsymbol{0} & \boldsymbol{0} & \boldsymbol{0} \\
-\boldsymbol{U}_{cu}^A & \boldsymbol{T}_{ct}^A & -\boldsymbol{U}_{cc}^A & -\frac{1}{2}\boldsymbol{I}_{cc}^A + \boldsymbol{T}_{cc}^A & \boldsymbol{0} & \boldsymbol{0} & \boldsymbol{0} & \boldsymbol{I}_{cc}^{AB} \\
\boldsymbol{T}_{cu}^{AT} & -\boldsymbol{D}_{ct}^A & -\frac{1}{2}\boldsymbol{I}_{cc}^A + \boldsymbol{T}_{cc}^{A*} & -\boldsymbol{D}_{cc}^A & \boldsymbol{0} & \boldsymbol{0} & \boldsymbol{0} & \boldsymbol{0} \\
\boldsymbol{0} & \boldsymbol{0} & \boldsymbol{0} & \boldsymbol{0} & -\boldsymbol{U}_{uu}^B & \boldsymbol{T}_{ut}^B & -\boldsymbol{U}_{uc}^B & \boldsymbol{T}_{uc}^B \\
\boldsymbol{0} & \boldsymbol{0} & \boldsymbol{0} & \boldsymbol{0} & \boldsymbol{T}_{tu}^B & -\boldsymbol{D}_{tt}^B & \boldsymbol{T}_{tc}^B & -\boldsymbol{D}_{tc}^B \\
\boldsymbol{0} & \boldsymbol{0} & \boldsymbol{0} & \boldsymbol{0} & -\boldsymbol{U}_{cu}^B & \boldsymbol{T}_{ct}^B & -\boldsymbol{U}_{cc}^B & \frac{1}{2}\boldsymbol{I}_{cc}^B + \boldsymbol{T}_{cc}^B \\
\boldsymbol{0} & \boldsymbol{0} & \boldsymbol{I}_{cc}^{BA} & \boldsymbol{0} & \boldsymbol{T}_{cu}^B & -\boldsymbol{D}_{ct}^B & \frac{1}{2}\boldsymbol{I}_{cc}^B + \boldsymbol{T}_{cc}^{B*} & -\boldsymbol{D}_{cc}^B
\end{pmatrix}; \tag{17}$$

the unknown functions are gathered in the vector function

$$\boldsymbol{X}^{RT} = \left(\boldsymbol{t}_u^A \quad \boldsymbol{u}_t^A \quad \boldsymbol{t}_c^A \quad \boldsymbol{u}_c^A \quad \boldsymbol{t}_u^B \quad \boldsymbol{u}_t^B \quad \boldsymbol{t}_c^B \quad \boldsymbol{u}_c^B \right), \tag{18}$$

and the given boundary data produce the vector

$$\boldsymbol{B}^{RT} = \left(\boldsymbol{B}_A^{\mathrm{T}} \quad \boldsymbol{B}_B^{\mathrm{T}} \right). \tag{19}$$

In the previous relations, symbols $\boldsymbol{I}$ denote the identity operators with the subscripts specifying the part of boundary where they are considered and superscripts declaring the domains at which they operate. For the formulation with the Lagrange multipliers, $\boldsymbol{\lambda}_t$ and $\boldsymbol{\lambda}_u$ do not have to be defined with respect to any domain, being defined only with respect to Γ_c, the superscript therefore indicating the pertinent function in this case.

Notes on discretization. The systems represented by eq (10) will be solved numerically by the SGBEM using both formulations introduced. Let us approximate the functions appearing there by straight linear boundary elements, allowing discontinuities of tractions at the junctions of the elements. Thus, the approximation formulae can be written in the form:

$$\boldsymbol{u}^{\eta}(x) \approx \sum_k \boldsymbol{N}_{\psi k}^{\eta}(x) \mathbf{u}_k^{\eta}, \quad \boldsymbol{t}^{\eta}(x) \approx \sum_k \boldsymbol{N}_{\phi k}^{\eta}(x) \mathbf{t}_k^{\eta}, \quad \boldsymbol{\lambda}_u(x) \approx \sum_{\kappa_u} \boldsymbol{N}_{\xi \kappa_u}(x) \boldsymbol{\lambda}_{\kappa_u}, \quad \boldsymbol{\lambda}_t(x) \approx \sum_{\kappa_t} \boldsymbol{N}_{\rho \kappa_t}(x) \boldsymbol{\lambda}_{\kappa_t}, \tag{20}$$

where $\boldsymbol{N}^{\eta}_{\psi k}(x)$ and $\boldsymbol{N}^{\eta}_{\phi k}(x)$, respectively, are matrices containing the shape functions of the displacements and tractions at the node k of the boundary Γ^{η} and $\mathbf{u}^{\eta}_k$ and $\mathbf{t}^{\eta}_k$ are vectors containing the nodal values of the pertinent functions at node k. Moreover, in the Lagrange multipliers formulation, the Lagrange multipliers $\boldsymbol{\lambda}_t$ and $\boldsymbol{\lambda}_u$ could be defined independently, not only with respect to other elastic variables but also with respect to each other, having created a new mesh or meshes at Γ_c with pertinent shape functions $\boldsymbol{N}_{\rho\kappa t}(x)$, $\boldsymbol{N}_{\xi\kappa u}(x)$ and nodal values $\boldsymbol{\lambda}_{\kappa t}$ and $\boldsymbol{\lambda}_{\kappa u}$.

The sets of vectors of virtual functions in eq (11) and (16) can be chosen so that they are equal to shape functions associated to each nodal unknown. Such a choice makes the matrix of the system square. Finally, the following system of linear equations is obtained:

$$\mathbf{A}\,\mathbf{X} = \mathbf{B}, \tag{21}$$

copying the structure of eq (10) and of the corresponding matrices from eq (12) to (15) and from eq (17) to (19). Notice that the identity operators $\boldsymbol{I}$ change to $\mathbf{M}$, which are the matrix representations of the projection operators between the pertinent spaces of shape functions, with the same indices as used with $\boldsymbol{I}$. Therefore, the matrices $\mathbf{M}$ are expressed through the following integrals:

$$\begin{aligned}
&\left(\mathbf{M}_{uu}^{\eta}\right)_{kl} = \int_{\Gamma_u^{\eta}} \boldsymbol{N}_{\phi k}^{\eta}(x)\, \boldsymbol{N}_{\psi l}^{\eta}(x)\, \mathrm{d}_x\Gamma, \quad \left(\mathbf{M}_{tt}^{\eta}\right)_{kl} = \int_{\Gamma_t^{\eta}} \boldsymbol{N}_{\psi k}^{\eta}(x)\, \boldsymbol{N}_{\phi l}^{\eta}(x)\, \mathrm{d}_x\Gamma, \quad \left(\mathbf{M}_{cc}^{\eta}\right)_{kl} = \int_{\Gamma_c} \boldsymbol{N}_{\phi k}^{\eta}(x)\, \boldsymbol{N}_{\psi l}^{\eta}(x)\, \mathrm{d}_x\Gamma, \\
&\left(\mathbf{M}_{cc}^{AB}\right)_{kl} = \int_{\Gamma_c} \boldsymbol{N}_{\phi k}^{A}(x)\, \boldsymbol{N}_{\psi l}^{B}(x)\, \mathrm{d}_x\Gamma, \quad \left(\mathbf{M}_{cc}^{\eta\lambda_u}\right)_{k\kappa_u} = \int_{\Gamma_c} \boldsymbol{N}_{\phi k}^{\eta}(x)\, \boldsymbol{N}_{\xi\kappa_u}(x)\, \mathrm{d}_x\Gamma, \quad \left(\mathbf{M}_{cc}^{\eta\lambda_t}\right)_{k\kappa_t} = \int_{\Gamma_c} \boldsymbol{N}_{\psi k}^{\eta}(x)\, \boldsymbol{N}_{\rho\kappa_t}(x)\, \mathrm{d}_x\Gamma, \\
&\mathbf{M}_{cc}^{BA} = \left(\mathbf{M}_{cc}^{AB}\right)^{\mathrm{T}}, \qquad \mathbf{M}_{cc}^{\lambda_u\eta} = \left(\mathbf{M}_{cc}^{\eta\lambda_u}\right)^{\mathrm{T}}, \qquad \mathbf{M}_{cc}^{\lambda_t\eta} = \left(\mathbf{M}_{cc}^{\eta\lambda_t}\right)^{\mathrm{T}}.
\end{aligned} \tag{22}$$

The last row in eq (22) is the condition of the symmetry of the resulting matrix $\mathbf{A}$. Note that this condition is always valid for the case of Γ_c given by a straight line. If Γ_c is curved, the property can be maintained by calculating the integrals over the common-refinement mesh, see [6].

Examples

Let us consider two problems for a ring body, with the elastic constants G=10^{4}MPa and ν=0.25 shown in Fig. 1(a) and (b). The first, Fig. 1(a), includes the fixed inner circumference and a shear load at the outer one. In the second, Fig. 1(b), the ring is loaded by four point tensile forces F, the inner circumference being free. Due to symmetry, only a quarter of the whole ring is considered for the numerical solution in both problems. Notice the different nature of the symmetry (symmetry and skew-symmetry) in each problem.

Let us distinguish the numerical results obtained by the two variational approaches presented by letters λ and R. The results shown contain the data from three different boundary element meshes along the interface as the role of the subdomains Ω^A and Ω^B in these variational formulations is different, see eqs (4) and (5). The first mesh contains n^A=48 elements along Ω_c on the Ω^A-side and n^B=112 elements on the Ω^B-side, the second mesh has the numbers of elements interchanged, i.e. n^A=112 and n^B=48, and the third mesh has the same number of elements on both sides of the interface Γ_c, n^A= n^B=48. For the R-formulation only the first and the third meshes are considered, as the other case, with $n^A > n^B$, leads to numerically unstable results, see

[1,2] for an analysis and explanations. It should be noted that the non-conforming meshes along a curved Γ_c lead to interpenetrations and gaps between the approximated subdomains, see Fig. 1 (c). Nevertheless, even in such a situation the numerical procedures presented are able to provide excellent approximations of the solution of the original problems.

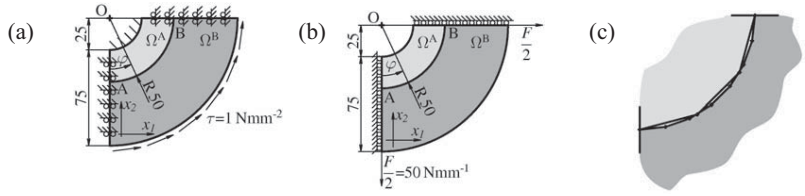

Figure 1: Problem geometry: (a) shear, (b) four point forces, (c) a non-conforming mesh.

The graphs contain the data obtained along the interface curve *AB*, both displacements and tractions fitting the analytical solutions very accurately. Nevertheless, some differences in the distribution of the errors appear. Let us compare the results for both examples shown in Fig. 2 and Fig. 3. While at the coarser meshes (n=48) the distributions of displacement errors are relatively smooth, the finer meshes (n=112) show some small oscillations. It is interesting to observe that in the shear-load example the displacements of the λ–formulation oscillate more significantly than in the other example. Oscillations in tractions are always higher than in displacements, especially close to the end points of the interface, see [2] for an explanation of these facts in the case of the *R*-formulation. Again, the oscillations are especially visible in the shear-load example. It can be seen that a certain pattern of these oscillations appears, as was discussed in detail in [2].

When the magnitude of the errors is compared, the errors of displacements in the shear-load example are an order lower than in the other example, while the highest peaks of traction errors are comparable.

As could be expected, it is also observed that the results of the conforming mesh are not oscillating, except for the corner points, independently of the formulation and the load nature.

Conclusions

Two variational SGBEM approaches for the DDBVP solution have been presented. The main conclusion of the numerical test performed, an excellent accuracy having been obtained by both approaches, is that both approaches can be recommended for engineering applications. An advantage of the reduced *R*-formulation over the λ-formulation with Lagrange multipliers is the lower number of unknowns associated to the interface (about 33% less), which can be relevant in DDBVPs where these variables represent a large portion of all the unknowns in the resulting linear problem. Some differences between the results of these formulations appear when we focus on the error behaviour along the interface. Due to the character of the interface conditions and the form of their imposition, the numerical data at fine meshes always present some oscillations. The magnitude of the oscillation peaks depends on the type of mesh used and on the approach followed. The weak form of the interface conditions in the *R*-formulation forces one body to control the tractions at the interface, while the other body is forced to control the interface displacements. As a result, some choices of the non-conforming mesh are not suitable for calculation as they produce, especially for tractions, large oscillations. Due to this fact, observed and explained in [1,2] in the case $n^A > n^B$, such meshes have not been used for the *R*-formulation. Nevertheless, the λ-formulation works well for any relation between n^A and n^B and does not show large errors of this kind for calculated tractions, inasmuch as it pushes these oscillations to the values of the multipliers, which are usually not of direct interest.

Acknowledgments. The financial support has been given to V.M. and F.P. from the Junta de Andalucia (Project of Excellence No. TEP 1207) and to R.V. from the Scientific Grant Agency of the Slovak Republic (Grant No.1/4160/07).

References

[1] R.Vodička, V.Mantič and F.París *Numerical Methods in Continuum Mechanics & 4th Workshop on Treffitz Methods*, CEACM, (2005).

[2] R. Vodička, V. Mantič and F. París *Computer Methods in Engineering and Sciences*, 17, 173-203 (2007).

[3] M.Bonnet *Engineering Analysis with Boundary Elements*, **15,** 93-102 (1995).

[4] A. Blázquez, F. París and V. Mantič *International Journal of Solids and Structures*, **35**, 3259–3278 (1998).

[5] C. Lacour and Y. Maday *BIT*, **37**, 720 – 738 (1997).

[6] X. Jiao and M.T.Heath *International Journal for Numerical Methods in Engineering,* **61**, 2402–2427 (2004).

[7] A.Quarteroni and A.Valli *Domain Decomposition Methods for Partial Differential Equations*, Oxford University Press (1999).

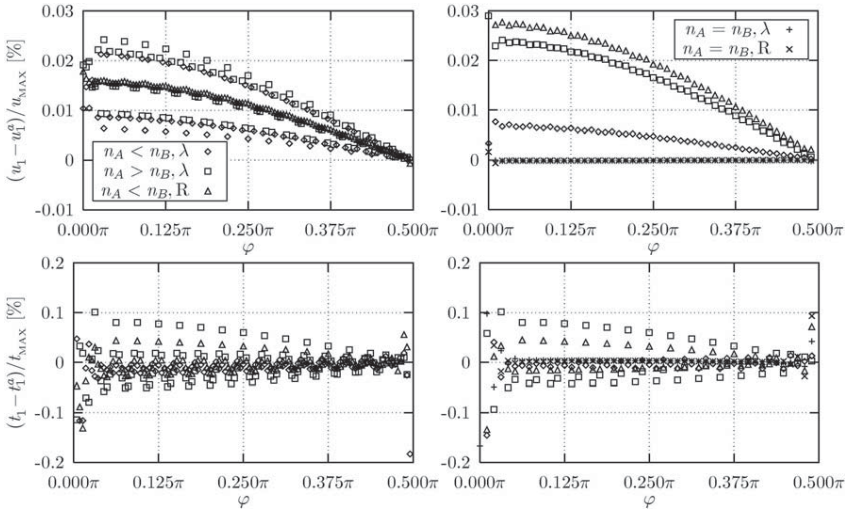

Figure 2: Shear load, errors of displacements (top) and tractions (bottom) for the finer mesh (left) and coarser mesh (right). The legend keys refer to the data of all pictures.

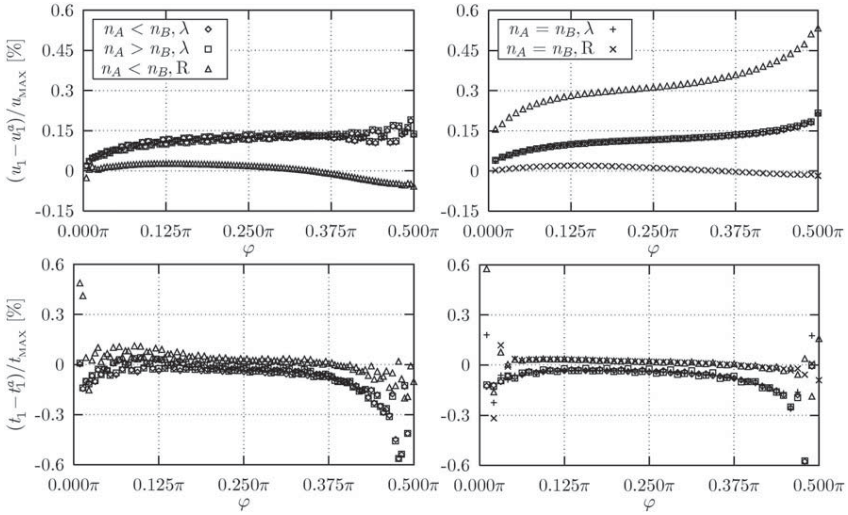

Figure 3: Load by four point forces, errors of displacements (top) and tractions (bottom) for the finer mesh (left) and coarser mesh (right). The legend keys refer to the data of all pictures.

Boundary element analysis of cracked thick plates repaired with adhesive composite patches

J. Useche[1], *P. Sollero*[1], *E.L. Albuquerque*[1], *L. Palermo Jr*[2]

State University of Campinas

[1]Faculty of Mechanical Engineering

[2]Faculty of Civil Engineering

Campinas, S.P. Brazil

sollero@fem.unicamp.br

Keywords: *Fracture mechanics, fracture plates, dual boundary element method, adhesive composite patches, anisotropic repair.*

Abstract. The fracture analysis of cracked thick plates repaired with adhesive composite patches using a boundary element formulation is presented. The shear deformable cracked isotropic plate was modeled using the dual boundary method. In order to model the repair, a three parameter boundary element formulation was established. This formulation is based on Kirchhoff's theory for anisotropic plates and considers the transversal deflection and two in-plane rotations. Interaction forces and moments between the cracked plate and the composite repair were modeled as distributed ones, and discretized using continuous and semi-discontinuous domain cells. Coupling equations, based on cinematic compatibility and equilibrium considerations for the adhesive, were established. In-plane shear-deformable adhesive model without transversal stiffness was considered in order to modeling de mechanical response of the adhesive. Stress intensity factors in the isotropic Reissners plate were calculated using the crack surface displacement extrapolation. A test problem considering circular composite repair is presented.

Introduction

Aeronautic structures are usually constituted of panels and metallic stiffeners. A cracked panel is frequently repaired by bonding, riveting or screwing a metallic patch on the cracked area. The life in fatigue and the residual stresses in the repaired panel are dependent on the efficiency of the load transfer of the cracked panel to the repair. Advanced bonded composite repairs have been used in the aeronautical industry and they are accepted as efficient solutions for the repair of damages. The main advantage, when compared to screwed or riveted repairs is that they supply a load transfer relatively uniform among the structural components that are bonded. The required holes for these fasteners act as stresses concentrators that reduces the useful life of the aeronautical panel.

The Boundary Element Method (BEM) is an attractive numerical alternative to treat fracture problems, mainly to its ability to model continuously high stress gradients without the need of domain discretization. The use of this method in structural analysis has strongly increased since 80s [1]. But, the analysis of cracked isotropic plates structures repaired with the application of adhesively bonded anisotropic patches using BEM hasn't been reported in the literature, yet.

Recently, [2] have presented a BEM for the analysis of metallic sheets repaired by screwed composite materials. The cracked sheet is modeled using the dual boundary element technique. Screws are modeled as linear springs whose forces are treated as point forces. The repair is modeled using a boundary element formulation for anisotropic plates. Later, [3] developed a boundary element formulation for the analysis of flat metallic plates with cracks and adhesive isotropic repairs. The effect of the adhesive layer was modeled considering them as distributed forces. A coupled integral formulation for plate with shear deformation and plane stress was used to determine bending moments and membrane forces in the adhesive repair. Boundary element formulations have been applied to plate bending anisotropic problems considering Kirchhoff as well as shear deformable plate theories.

[4] presented a boundary element analysis of plate bending problems based on Kirchhoff plate bending assumptions. Shear deformable cracked plates have been analyzed using boundary element method by [3] with the fundamental solution proposed by [5]. [6] presented a displacement discontinuity formulation for modeling cracks in orthotropic Reissner plates. Fundamental solutions for displacement discontinuity were derived for the first time using a Fourier transform method. Boundary element method for orthotropic Reissner plates was presented by [7].

Boundary integral formulation for isotropic plates

The two dimensional boundary integral equation for displacements at the boundary point $\mathbf{x}' \in \Gamma$ that describes membrane effects can be written as [1]:

$$c_{ij}^{P}\left(\mathbf{x}'\right) u_{\beta}\left(\mathbf{x}'\right) = \int_{\Gamma} U_{\alpha\beta}^{P}\left(\mathbf{x}', \mathbf{x}\right) t_{\beta} d\Gamma - \int_{\Gamma} T_{\alpha\beta}^{P}\left(\mathbf{x}', \mathbf{x}\right) u_{\beta} d\Gamma + \frac{1}{h_p} \int_{A} U_{\alpha\beta}^{P}\left(\mathbf{x}', \mathbf{x}\right) f_{\beta} dA \tag{1}$$

where α, $\beta = 1$, 2 and $c_{ij}^{P}(\mathbf{x}')$ is a function of the geometry at the collocation points that can be determined by considering rigid body movements. The boundary displacements and tractions for the sheet are denoted by u_{α} and $t_{\alpha}(= n_{\beta}\sigma_{\alpha\beta})$, respectively; displacement and traction fundamental solutions for the plane stress condition are $U_{\alpha\beta}^{P}(\mathbf{x}', \mathbf{x})$ and $T_{\alpha\beta}^{P}(\mathbf{x}', \mathbf{x})$, respectively, $f_{\beta}(\mathbf{x})$ denote two-dimensional body forces per area unit over a region A of the patch, and h_p is the thickness of the plate. In this work no others in-plane body forces will be considered.

In order to model cracked plates, the Dual Boundary Element Method (DBEM) will be used. In this method, the displacement integral formulation is written for source points on one crack surface and the traction integral equation on the other surface. Then, using the stress and strain relationships for plane stress, the traction integral equation for two-dimensional problems in a smooth boundary can be derived as [8]:

$$\begin{aligned} \frac{1}{2} t_{\alpha}\left(\mathbf{x}'\right) &= n_{\beta}\left(\mathbf{x}'\right) \int_{\Gamma} U_{\alpha\beta\gamma}^{P}\left(\mathbf{x}', \mathbf{x}\right) t_{\gamma} d\Gamma - n_{\beta}\left(\mathbf{x}'\right) \int_{\Gamma} T_{\alpha\beta\gamma}^{P}\left(\mathbf{x}', \mathbf{x}\right) u_{\gamma} d\Gamma \\ &\quad + n_{\beta}\left(\mathbf{x}'\right) \frac{1}{h_p} \int_{A} U_{\alpha\beta\gamma}^{P}\left(\mathbf{x}', \mathbf{x}\right) f_{\beta} dA \end{aligned} \tag{2}$$

where $n_{\beta}(\mathbf{x}')$ is the normal to the boundary evaluated at collocation point. $U_{\alpha\beta\gamma}^{P}(\mathbf{x}', \mathbf{x})$ and $T_{\alpha\beta\gamma}^{P}(\mathbf{x}', \mathbf{x})$ are the traction fundamental solution for two-dimensional problems.

Boundary integral formulation for plate bending

If w_{α} are defined as rotations in the x_{α} direction, w_3 is the deflection of the plate along x_3, q_{α}^{P} and q_3^{P} are the distribution of body forces in moment and the out-of-plane body force per area unit, respectively, in the patch area A, and p_o is the pressure force applied in the domain of the plate Ω. The boundary integrals for the plate bending problem can be written as:

$$\begin{aligned} c_{ik}^{P}\left(\mathbf{x}'\right) w_{k}\left(\mathbf{x}'\right) &= \int_{\Gamma} W_{ik}^{P}\left(\mathbf{x}', \mathbf{x}\right) p_{k} d\Gamma - \int_{\Gamma} P_{ik}^{P}\left(\mathbf{x}', \mathbf{x}\right) w_{k} d\Gamma + p_o \int_{\Omega} W_{i3}^{P}\left(\mathbf{x}', \mathbf{x}\right) d\Omega \\ &\quad + \int_{A} W_{ik}^{P}\left(\mathbf{x}', \mathbf{x}\right) q_{k}^{P} dA \end{aligned} \tag{3}$$

where $k = 1 \ldots 3$. $W_{\alpha\beta}^{P}(\mathbf{x}', \mathbf{x})$ and $P_{\alpha\beta}^{P}(\mathbf{x}', \mathbf{x})$ are the fundamental solutions for Reissner's plate model (see Ween [5]) and $p_{\alpha} = M_{\alpha\beta} n_{\beta}$, $p_3 = Q_{\beta} n_{\beta}$. Constant c_{ik}^{P} has a similar significance with those at in-plane displacement problem.

In a similar way, fracture mechanics problems involving plate bending can be modeled using DBEM. In this case, the traction equation can be written as:

$$\frac{1}{2} p_{i}\left(\mathbf{x}'\right) = n_{\beta}\left(\mathbf{x}'\right) \int_{\Gamma} W_{i\beta k}^{P}\left(\mathbf{x}', \mathbf{x}\right) p_{k} d\Gamma - n_{\beta}\left(\mathbf{x}'\right) \int_{\Gamma} P_{i\beta k}^{P}\left(\mathbf{x}', \mathbf{x}\right) w_{k} d\Gamma$$

$$+n_\beta(\mathbf{x}')\,p_o\int_\Omega W^P_{i\beta 3}(\mathbf{x}',\mathbf{x})\,d\Omega + n_\beta(\mathbf{x}')\int_A W^P_{i\beta k}(\mathbf{x}',\mathbf{x})\,q^P_k\,dA \tag{4}$$

where $W^P_{i\beta\gamma}(\mathbf{x}',\mathbf{x})$ and $P^P_{i\beta\gamma}(\mathbf{x}',\mathbf{x})$ are the traction fundamental solution for Reissner's plate [8].

Boundary integral formulation for anisotropic repair

Similarly to the isotropic case, the in-plane displacements of a point $\mathbf{x}'$ in the anisotropic patch are given by:

$$c^R_{\alpha\beta}(\mathbf{x}')\,u^R_\beta + \int_{\Gamma_R} T^R_{\alpha\beta}(\mathbf{x}',\mathbf{x})\,u^R_\beta d\Gamma = \frac{1}{h_R}\int_A U^R_{\alpha\beta}(\mathbf{x}',\mathbf{x})\,f^R_\beta dA \tag{5}$$

where $T^R_{\alpha\beta}(\mathbf{x}',\mathbf{x})$ and $T^R_{\alpha\beta}(\mathbf{x}',\mathbf{x})$ are the traction and displacements fundamental solutions for anisotropic plane elasticity ploblems and h_R represents the repair thickness [9]. Others variables have similar meaning to the isotropic case.

To model the bending response of the repair, a boundary integral formulation for Kichhoff plate's model with three unknowns at every point is used in this work considering the original form of the Betti's theorem for the Kirchhoff plate:

$$\begin{aligned}&\int_\Gamma \left(W_{,n}(\mathbf{x}',\mathbf{x})m_n(\mathbf{x}) + W_{,s}(\mathbf{x}',\mathbf{x})t_s(\mathbf{x}) - W(\mathbf{x}',\mathbf{x})v_n(\mathbf{x})\right)d\Gamma\\ &= \int_\Gamma \left(M_n(\mathbf{x}',\mathbf{x})w_{,n}(\mathbf{x}) + T_s(\mathbf{x}',\mathbf{x})w_{,s}(\mathbf{x}) - V_n(\mathbf{x}',\mathbf{x})w(\mathbf{x})\right)d\Gamma\end{aligned} \tag{6}$$

where $w(\mathbf{x})$ and $w_{,n}(\mathbf{x})$ are the bending deflexion and the normal rotation, respectively, $v_n(\mathbf{x})$ and $m_n(\mathbf{x})$ are the shear force and the normal moment, respectively, and $t_s(\mathbf{x})$ is the tangent moment. $W(\mathbf{x}',\mathbf{x})$, $V_n(\mathbf{x}',\mathbf{x})$, $M_n(\mathbf{x}',\mathbf{x})$, $T_s(\mathbf{x}',\mathbf{x})$ are the fundamental solutions for Kirchhoff plate. Using the stress-strain relationships for anisotropic Kirchhoff plates (see ref. [9]), integrating by parts, taking as weight function $w^* = \delta(\mathbf{x}',\mathbf{x})$ (where $\delta(\mathbf{x}',\mathbf{x})$ is the Dirac's delta function) and considering: $t_s \equiv 0$ we obtain the displacement integral formulation for bending plate with three parameters, two in-plane rotations ($w_{,n}$, $w_{,s}$) and the flexural bending w:

$$\begin{aligned}&w(\mathbf{x}') + \int_\Gamma \left[V_n(\mathbf{x}',\mathbf{x})\,w^R(\mathbf{x}) - M_n(\mathbf{x}',\mathbf{x})\,w^R_{,n}(\mathbf{x}) - T_s w^R_{,s}(\mathbf{x})\right]d\Gamma\\ &= \int_\Gamma \left[W(\mathbf{x}',\mathbf{x})\,v_n - W_{,n}(\mathbf{x}',\mathbf{x})m_n(\mathbf{x})\right]d\Gamma + \int_A W_{,\alpha}(\mathbf{x}',\mathbf{x})\,q^R_\alpha dA + \int_A W(\mathbf{x}',\mathbf{x})\,q^R_3 dA\end{aligned} \tag{7}$$

with $\alpha = 1,2$. ${q_\alpha}^R$ and q^R_3 are distributed body moments and out-of-plane body force by area unit, respectively, generated by interaction with the adhesive layer (super-index R refers to repair).

A second boundary integral equation is obtained by differentiating eq. (7) with respect to point $\mathbf{x}'$ in the tangent direction:

$$\begin{aligned}&w_{,s} + \int_\Gamma \left[V_{n,s}(\mathbf{x}',\mathbf{x})\,w^R(\mathbf{x}) - M_{n,s}(\mathbf{x}',\mathbf{x})\,w^R_{,n}(\mathbf{x}) - T_{s,s}w^R_{,s}(\mathbf{x})\right]d\Gamma\\ &= \int_\Gamma \left[W_{,s}(\mathbf{x}',\mathbf{x})\,v_n - W_{,ns}(\mathbf{x}',\mathbf{x})m_n(\mathbf{x})\right]d\Gamma + \int_A W_{,\alpha s}(\mathbf{x}',\mathbf{x})\,q^R_\alpha dA + \int_A W_{,s}(\mathbf{x}',\mathbf{x})\,q^R_3 dA\end{aligned} \tag{8}$$

Finally, a third integral equation can be obtained differentiating eq. (7) in the normal direction:

$$\begin{aligned}&w_{,n} + \int_\Gamma \left[V_{n,n}(\mathbf{x}',\mathbf{x})\,w^R(\mathbf{x}) - M_{n,n}(\mathbf{x}',\mathbf{x})\,w^R_{,n}(\mathbf{x}) - T_{s,n}(\mathbf{x}',\mathbf{x})\,w^R_{,s}(\mathbf{x})\right]d\Gamma\\ &= \int_\Gamma \left[W_{,n}(\mathbf{x}',\mathbf{x})\,v_n - W_{,nn}(\mathbf{x}',\mathbf{x})\,m_n\right]d\Gamma + \int_A W_{,\alpha n}(\mathbf{x}',\mathbf{x})\,q^R_\alpha dA + \int_A W_{,n}(\mathbf{x}',\mathbf{x})\,q^R_3 dA\end{aligned} \tag{9}$$

Coupling equations

Isotropic plate equations has fifteen unknown variables: five displacements (or tractions) at any boundary points and five unknown displacements and five interaction body forces at any point in the repair region. In addition, ten unknowns appears at repair: five displacements (at boundary and domain) and five interacion body forces (at domain). In this way we have twenty five unknows in the problem. Eq. (1) throught eq. (9) represent only fifteen equations. Ten aditional equations must be provided. Additional equations can be written if cinematic compatibility between the plate and the repair and the equilibrium conditions at adhesive layer, are considered. In this way, a total of twenty five equations could be written.

The equilibrium of forces acting in the adhesive layer can be written as:

$$f_\alpha^P + f_\alpha^R = 0$$

$$q_3^P + q_3^R = 0$$

$$q_\alpha^P + q_\alpha^R + f_\alpha^R \left(h_A + \frac{h_P + h_R}{2} \right) = 0 \tag{10}$$

where h_A represents the thickness of the adhesive.

The shear force $\tau_{3\alpha}^A$, acting at interior of adhesive layer can be written as:

$$\tau_{3\alpha}^A = f_\alpha^R = \frac{\mu_A}{h_A} \left(u_\alpha^R - \frac{h_R}{2} w_\alpha^R \right) - \left(u_\alpha^P + \frac{h_P}{2} w_\alpha^P \right) \tag{11}$$

where μ_A is the shear modulus of the adhesive and h_A its thickness. Finally, we can consider that deflexion and rotation angles at coincident points at plate and repair can be related as:

$$\begin{aligned} w_3^P &= w_3^R \\ q_\alpha^P &= C \left(w_\alpha^R + w_\alpha^P \right) \end{aligned} \tag{12}$$

where, $C = D(1-\nu)\lambda^2/2$. In this way, eq. (10) through eq. (12) represent ten additional equations obtained by considering equilibrium and cinematic compatibility conditions in the adhesive layer.

Stress intensity factor calculation

For plate problems, considering bending and plane tension, the stress intensity factors can be represented by superposition of five stress intensity factors (SIF's), two due to membrane loads and three due to bending and shear loads. In terms of displacements on the crack surfaces they can be written as (see reference [8]):

$$\{K\} = \frac{1}{\sqrt{r}} \mathbf{C} \{\Delta w\} \tag{13}$$

where K is a vector containing the five stress intensity factors. Using the extrapolation technique and discontinuos quadratic boundary elements for modeling crack surfaces, SIF can be calculated as:

$$\{K\}^{tip} = \frac{r_{AA'}}{r_{AA'} - r_{BB'}} \left(\{K\}^{BB} - \frac{r_{BB'}}{r_{AA'}} \{K\}^{AA'} \right) \tag{14}$$

Numerical Results

In order to test the formulation developed here, the boundary element analysis of a rectangular isotropic cracked plate repaired with adhesively bonded anisotropic circular patch is presented. The plate is $248mm \times 118mm$, thickness $h_P = 2.0mm$ and it is subject to in-plane load $\sigma_0 = 79.4MPa$. The material constants are chosen as $E = 72.39GPa$, $\nu = 0.33$. A circular anisotropic patch of radius $R = 25mm$ and thickness $h_R = 3.2mm$ is bonded to the plate (see Fig. 1). The mechanical properties

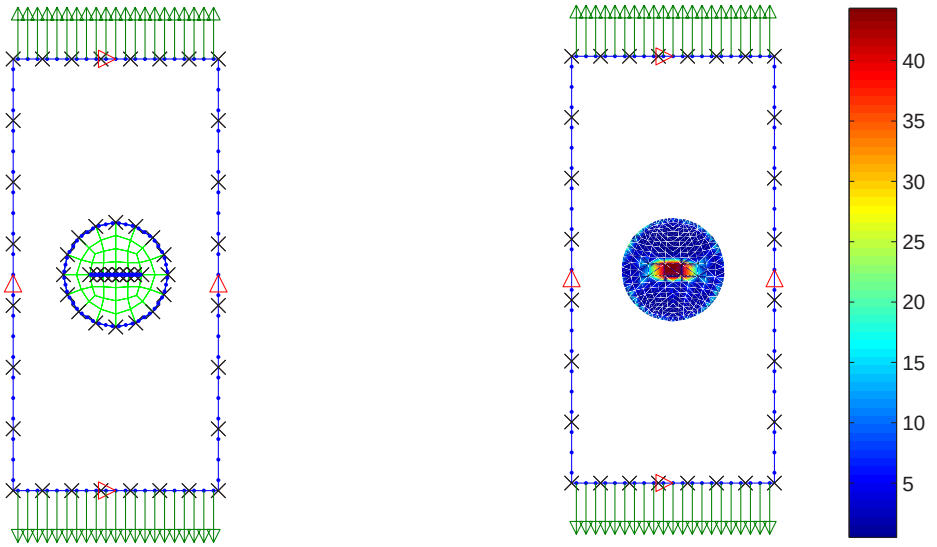

Figure 1: Boundary element model for cracked isotropic plate repaires with composite circular patch and shear stress distribution in the adhesive

are of patch are: $E_1 = 37.35GPa$, $E_2 = 11.38GPa$, $G_{12} = 5.97GPa$ and $\nu = 0.38$. The adhesive layer has thickness $h_a = 0.1mm$ and shear modulus $G_a = 0.44GPa$. This analysis was performed using a combined boundary element method and finite element method formulation as presented in ref. [10], where the cracked plate is modeled using a 3D BEM model and the repair a plate model.

A total of 28 quadratic discontinuous boundary elements were used to discretize the boundary of the isotropic cracked plate. Meshes from 4 to 16 quadratic discontinuous boundary elements were used to discretize the crack faces. The patch was discretized using 128 cells and 24 quadratic discontinuous elements. Simply supported conditions were applied to all sides. The resultant shear stress distribution in the adhesive layer obtained is showed in Fig. 1.

Table 1 compares values for the maximum stress intensity factor calculated along plate thickness with those K_I reported in [10].

Table 1: Stress intensity factors for cracked plate repaired with composite patch

z(mm)	$K_{Imax}(MPam^{1/2})$ **BEM**	$K_I(MPam^{1/2})$**-Ref.[10]**	error
0.40	13.82	12.60	4.32%
0.80	11.56	11.09	4.24%
1.20	9.89	9.52	3.89%
1.60	8.15	7.84	3.95%

Conclusions

The analysis of cracked isotropic thick plates repaired with symmetrical laminate composite plates using the boundary element method, was presented. The equations for the repair is based on boundary integral formulation considering three parameters, based on the theory of plates of Kirchhoff as a generalization of the integral formulation of thin plates traditionally used. The isotropic model linear proposed for the adhesive considers shear forces and bending moments acting on it. This way, equations for kinematic coupling for displacements and rotations, as well as a system of equations that describes

the equilibrium of forces and moments that act on the adhesive, were established. Domain integrals containing forces and moments in the repair's area were treated with using the cell method. It can be concluded that the new formulation can be used with reasonable accuracy to study the mechanical behavior of cracked plates repaired with adhesively bonded composite repairs under in-plane load actions. More research work must be done to obtain more accurate values for stress intensity factors.

References

[1] Brebbia, C. A. and Dominguez, J. *Boundary Element - An Introductory Course.* Computational Mechanics Publications, 2 ed., Southamptom, (1989).

[2] Widagdo, D., Aliabadi, M. H. *Boundary element analysis of cracked panels repaired by mechanically fastened composite patches.* Engineering analysis with boundary elements, **25**(4-5): 339-345 apr-may (2001).

[3] Wen, P. H, Aliabadi, M. H, Young, A. *Boundary element analysis of flat cracked panels with adhesively bonded patches.* Engineering Fracture Mechanics, **69**: 2129-2146, (2002).

[4] Shi, G. and Bezine, G. *A general boundary integral formulation for the anisotropic plate bending problems.* Journal of Composite Materials, **22**: 694-716, (1988).

[5] Vander Weeën, F. *Application of the boundary integral equation method to Reissner's plate model.* International Journal for Numerical Methods In Engineering, **18**: 1-10, (1982).

[6] Wen, P. H. and Aliabadi, M. H. *Displacement discontinuity formulation for modeling cracks in ortotropic shear deformable plates.* International Journal of Fracture Mechanics, **12**: 69-79, (2006).

[7] Wang, J. and Huang, M. *Boundary element method for ortotropic thick plates.* Acta Mechanica Sinica, **7**: 258-266, (1991).

[8] Dirgantara, T. *Boundary Element Analysis of Cracks in Shear Deformable Plates and Shells.* Topics in Engineering, V. 43, Southampton, WIT Press, (2002).

[9] Albuquerque E. L, *Numerical analysis of composite plates using the boundary element method.* Scientific Report No. 03/11537-3. Universidade Stadual de Campinas, School of Mechanical Engineering, Department of Mechanical Design, (2006)

[10] Sekine, H., Yan, B., Yasuho, T. *Numerical simulation study of fatigue crack growth behaviour of cracked aluminium panels repaired with a FRP composite patch using combined BEM/FEM* Engineering Fracture Mechanics, **72**: 2549-2563 (2005)

A BEM to Time-Harmonic Vibration Analyses of 3D Piezoelectric Solids

Michiaki Takagi[1], Toshiro Matsumoto[2], Hironori Ito[3],
Keisuke Kamiya[4], Masataka Tanaka[5]

[1]Seiko Epson Corporation
Suwa, Nagano 392-8502, Japan
E-mail: Takagi.Michiaki@exc.epson.co.jp

[2]Department of Mechanical Science and Engineering, Nagoya University
Furo-cho, Chikusa-ku, Nagoya City, 464-8603, Japan
E-mail: t.matsumoto@nuem.nagoya-u.ac.jp

[3]Department of Mechanical Science and Engineering, Nagoya University
Furo-cho, Chikusa-ku, Nagoya 464-8603, Japan
E-mail: h_ito@nuem.nagoya-u.ac.jp

[4]Department of Mechanical Science and Engineering, Nagoya University
Furo-cho, Chikusa-ku, Nagoya 464-8603, Japan
E-mail: kamiya@nuem.nagoya-u.ac.jp

[5]Graduate School of Shinshu University
4-17-1, Wakasato, Nagano City, 380-8553, Japan

Keywords: Piezoelectric material, Time-harmonic vibration, Fundamental solution, Boundary Element Method

Abstract A boundary element method using the fundamental solution for time-harmonic vibration of a piezoelectric material is presented. The fundamental solution is separated into the static singular part and the dynamical regular part as outlined in the conventional works. The boundary integral equation is regularized by using the static singular part of the fundamental solution. A boundary element code is developed based on the present formulation and the validity of the formulation is demonstrated through a numerical example by comparing the results with those obtained by a different numerical method.

Introduction

Time-harmonic vibration analyses are important for the efficient designs of high-performance piezoelectric devices, such as surface acoustic wave (SAW) devices. Although the boundary element method has been applied to 2D time-harmonic vibration analyses for solids of fully anisotropic and piezoelectric media [1], that for 3D solids with fully anisotropic material constants, based on the exact fundamental solution, has not been applied so far due to the complicated expression of the fundamental solution and the heavy computation costs in evaluating the dynamic fundamental solution. Only the results based on the static fundamental solution can be observed [2, 3] in the reference.

In this paper, we derive a fundamental solution of 3D time-harmonic vibration for piezoelectric solid with fully anisotropic material constants following Wang and Achenbach [4], and the outline by Norris [5]. As in the corresponding fundamental solution for fully anisotropic solids, the fundamental solution for the present problem comprises its singular part [4] and the regular part. By using the singular part of the fundamental solution, the corresponding Somigliana type integral identity is regularized. The regularized integral representation can be used as the boundary integral equation to be discretized.

A boundary element code for three-dimension piezoelectric materials is developed based on the present formulation. Numerical results obtained by the boundary element code are given for a rectangular solid model. The results obtained by the present boundary element method is compared with those obtained by a different numerical method to verify the formulation.

Boundary Integral Formulation

Governing Equations and Integral Representation. The governing equations for time-harmonic vibration of a piezo-electric solid is given as

$$C_{ijkl}u_{k,li} + \rho\omega^2 u_j + e_{lij}\bar{\varphi}_{,li} = 0 \tag{1}$$

$$e_{ikl}u_{k,li} - \varepsilon_{il}\varphi_{,li} = 0 \tag{2}$$

where σ_{ij} denotes the stress tensor, C_{ijkl} the elastic moduli, ϵ_{kl} the strain tensor, e_{ikl} the piezoelectric stress constants, D_i the electric displacement vector, ε_{il} the permittivity constants, q the electric charge density, u_k the displacement vector, φ the electric potential, ρ the density of the piezoelectric solid. A subscript denotes the cartesian component of the vector or the tensor, and the summation convention applies to repeated indices. By grouping together u_j and φ as $U_J = u_j$ for $j = 1,\ 2,\ 3$ and $U_J = \varphi$ for $J = 4$, the governing equations (1) and (2) can be written in a simplified form

$$\Gamma_{JK}(\partial)U_K = 0 \tag{3}$$

where

$$\Gamma_{JK}(\partial) = \begin{bmatrix} C_{ijkl}\partial_l\partial_i + \rho\omega^2\delta_{jk} & e_{lij}\partial_l\partial_i \\ e_{ikl}\partial_l\partial_i & -\varepsilon_{il}\partial_l\partial_i \end{bmatrix} \tag{4}$$

The integral representation corresponding to eq (3) is obtained, starting from the weighted-residual form of eq (3), in the form

$$U_M(y) + \int_\Gamma T^*_{JM}U_J\, d\Gamma = \int_\Gamma U^*_{JM}T_J\, d\Gamma \tag{5}$$

where U^*_{JM} is the fundamental solution of the adjoint form of eq (3).
T_J and T^*_{JM} are related to U_J and U^*_{JM}, respectively, by

$$T_j = \left(C_{ijkl}U_{k,l} + e_{lij}U_{4,l}\right)n_i \tag{6}$$

$$T_4 = \left(e_{ikl}U_{k,l} - \varepsilon_{il}U_{4,l}\right)n_i \tag{7}$$

$$T^*_{jM} = \left(C_{ijkl}U^*_{kM,l} + e_{lij}U^*_{4M,l}\right)n_i \tag{8}$$

$$T^*_{4M} = \left(e_{ikl}U^*_{kM,l} - \varepsilon_{il}U^*_{4M,l}\right)n_i \tag{9}$$

Fundamental Solution. The fundamental solution U^*_{JM} can be obtained by using the Radon Transform [6], following Wang and Achenbach [4] and Norris [5], as follows:

$$U^*_{kM} = \frac{1}{8\pi^2}\int_{|\mathbf{n}|=1}\sum_{m=1}^{3}\frac{1}{2\lambda_m}E_{km}E_{jm}P_{jM}(\mathbf{n})\left[2\delta(\mathbf{n}\cdot\mathbf{x}) + \mathrm{i}k_m\mathrm{e}^{\mathrm{i}k_m|\mathbf{n}\cdot\mathbf{x}|}\right]dS(\mathbf{n}) \tag{10}$$

$$U^*_{4M} = \frac{1}{8\pi^2}\int_{|\mathbf{n}|=1}\left\{\frac{\beta_k(\mathbf{n})}{\alpha(\mathbf{n})}\sum_{m=1}^{3}\frac{1}{2\lambda_m}E_{km}E_{jm}P_{jM}(\mathbf{n})\left[2\delta(\mathbf{n}\cdot\mathbf{x}) + \mathrm{i}k_m\mathrm{e}^{\mathrm{i}k_m|\mathbf{n}\cdot\mathbf{x}|}\right] - \frac{\delta_{4M}\delta(\mathbf{n}\cdot\mathbf{x})}{\alpha(\mathbf{n})}\right\}dS(\mathbf{n}) \tag{11}$$

The terms appearing in eqs (10) and (11) are defined below.

$$\alpha(\mathbf{n}) = \varepsilon_{il}n_l n_i \tag{12}$$

$$\beta_k(\mathbf{n}) = e_{ikl}n_l n_i \tag{13}$$

where $\mathbf{n} = n_i$ $(i = 1,\ 2,\ 3)$ is the real number parameters of the Radon transform.

$$Q_{jk}(\mathbf{n}) = C_{ijkl} n_l n_i + \frac{\beta_j(\mathbf{n})\beta_k(\mathbf{n})}{\alpha(\mathbf{n})} \tag{14}$$

$$P_{jM}(\mathbf{n}) = \delta_{jM} + \frac{\beta_j(\mathbf{n})}{\alpha(\mathbf{n})}\delta_{4M} \tag{15}$$

Also, λ_m and E_{jm} $(m = 1,\ 2,\ 3)$ are the eigen values and the eigenvectors, respectively, of $Q_{jk}(\mathbf{n})$.
The integrals in eqs (10) and (11) are evaluated over a unit spherical surface for $\mathbf{n}$. Also, they can be splitted into two parts: the singular parts corresponding to static loading and the regular dynamical parts. Let us denote these parts by U^{*S}_{JM} and U^{*R}_{JM}. Then, U^{*S}_{JM} results in the line integral form for a unit circle with $O(1/r)$ singularity. Although U^{*R}_{JM} has no singularity, it have to be evaluated over a unit sphere.

Boundary Integral Equation. The boundary integral equation is easily derived by using the singular part of the fundamental solution. The integral representation (5) can be regularized in the form

$$\left(\int_\Gamma T^{*R}_{JM}\, d\Gamma\right) U_M(y) + \int_\Gamma T^*_{JM}\,(U_J - U_J(y))\; d\Gamma = \int_\Gamma U^*_{JM} T_J\, d\Gamma \tag{16}$$

Numerical Results
We consider a rectangular solid model as shown Fig.1. The model is discretized with 56 quadratic elements each of which has eight nodes. The total number of nodes is 170. The surface at $x_1 = 0$, perpendicular to x_1 axis, is assumed to be a roller-support boundary. The electric displacement is assumed to be 0 on the surface. On the surface at $x_1 = 0.12$, also perpendicular to x_1 axis, the electric displacement is also assumed to be 0 but the harmonic excitation traction of 1 [MPa] in x_1-direction is assumed to be applied. On all the surfaces perpendicular to x_2 axis, the electric displacement is assumed to be 0, but the surface at $x_2 = 0$ is assumed to be a roller-support one and the surface at $x_2 = 0.4$ is assumed to be traction free. Also, on both surfaces perpendicular to x_3 axis, the electric potential is assumed to be 0. The surface at $x_3 = 0$ is assumed to be a roller-support one and the surface at $x_3 = 0.4$ is assumed to be traction free.

The material properties are assumed to be $c_{11} = 139$ [GPa], $c_{12} = 77.8$ [GPa], $c_{13} = 74.3$ [GPa], $c_{33} = 115$ [GPa], $c_{44} = 25.6$ [GPa], $c_{66} = 30.6$ [GPa], $E_{15} = 12.7$ [C/m^2], $E_{24} = 12.7$ [C/m^2], $E_{31} = -5.2$ [C/m^2], $E_{32} = -5.2$ [C/m^2], $E_{33} = 15.1$ [C/m^2], $\varepsilon_{11} = 6.461 \times 10^{-9}$ [C/Vm], $\varepsilon_{22} = 6.461 \times 10^{-9}$ [C/Vm], $\varepsilon_{33} = 5.620 \times 10^{-9}$ [C/Vm], where $c_{\alpha\beta}$ $(\alpha = 1,\ ...,\ 6;\ \beta = 1,\ ...,\ 6)$ and E_{kp} $(k = 1,\ 2,\ 3;\ p = 1,\ ...,\ 6)$ are the matrices of the elastic moduli and the piezoelectric constants, respectively. The subscripts α and β of $c_{\alpha\beta}$ is related to the indices $i,\ j,\ k,\ l$ of the elastic moduli C_{ijkl} by $\alpha = i$ $(i = j)$, $9 - i - j$ $(i \neq j)$ and $\beta = k$ $(k = l)$, $9 - k - l$ $(k \neq l)$. In the similar manner, the components of the matrix of the piezoelectric constants are related those of the piezoelectric tensor as $E_{k1} = e_{k11},\ E_{k2} = e_{k22},\ E_{k3} = e_{k33},\ E_{k4} = e_{k23} = e_{k32},\ E_{k5} = e_{k13} = e_{k31},\ E_{k6} = e_{k12} = e_{k21}$ with $k = 1,\ 2,\ 3$. Also the density and the frequency are assumed to be 7600 [kg/m^3] and 1500 [Hz], respectively.

The Gaussian quadrature with sixteen points is used for the numerical integrations to evaluate the fundamental solutions and to evaluate the boundary integral of each element. We show in Fig.2 and 3 the results for the displacement u_2, x_2 component of the displacement and the electric displacement $D = D_i n_i$, both along the line AB of the rectangular solid, respectively. The BEM results are compared with those obtained by a collocation method based on the approximation in terms of radial basis functions [7]. Both the results obtained by two different numerical methods show good agreement.

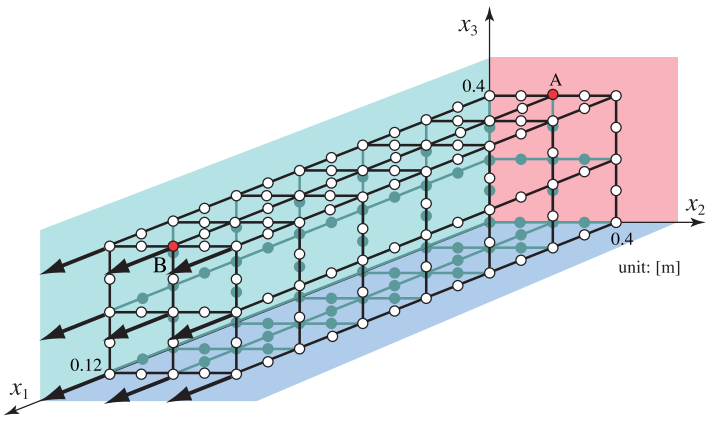

Fig. 1 A rectangular solid model subjected to harmonic excitation loads.

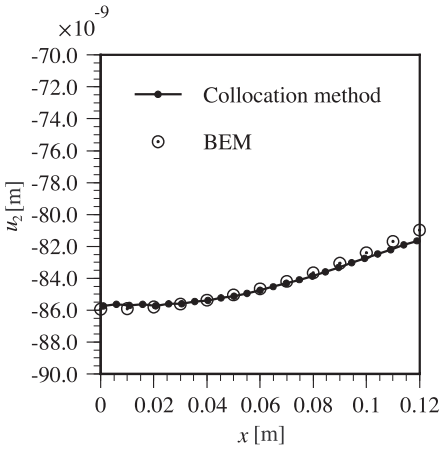

Fig. 2 Results for the displacement u_2 along the line AB of the rectangular solid model.

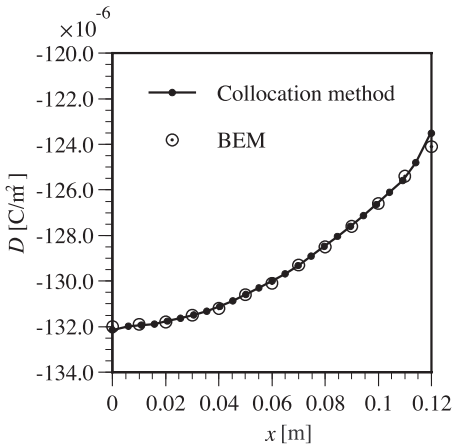

Fig. 3 Results for the charge flux densities D along the line AB of the rectangular solid model.

Concluding Remarks

A fundamental solution of 3D time-harmonic vibration for piezoelectric solid with fully anisotropic material constants has been derived and a boundary element code for three-dimension piezoelectric material has been developed using the formulation. The present formulation has been demonstrated through a numerical example by comparing the results with those obtained by a different numerical method.

References

[1] M.Denda and Y.Araki *The 15th ASCE Engineering Mechanics Division Conference (EM2002)*, New York, USA, June 2002, 77-84 (2002).

[2] M.Kögel and L.Gaul *Boundary Elements XXI*, C.A.Brebbia and H.Power (eds.) , Oxford, UK, WIT Press, Southampton, 537-548 (1999).

[3] L.R.Hill and T.N.Farris *AIAA Journal*, **36**, 102-108 (1998).

[4] C.Y.Wang and J.D.Achenbach *Proc. R. Soc. Lond.*, A, **449**, 441-458 (1995).

[5] A.N.Norris *Proc. R. Soc. Lond.*, A, **447**, 175-188 (1994).

[6] L.Debnath and D.Bhatta *Integral Transforms and Their Applications*, Chapman & Hall/CRC (2007).

[7] E.J.Kansa *Comput. Math. Appl.*, **19**, 147-161 (1990).

Modeling of Composites Reinforced by Short Fibers by the Method of Continuous Source Functions

Mário Štiavnický[1] , Vladimír Kompiš[1]

[1]Department of Mechanical Engineering, Academy of Armed Forces of gen. M. R. Štefánik,

Demänovská 393, 03119 Lipt. Mikuláš, Slovakia

e-mail: kompis@aoslm.sk

Keywords: composite structure, short fibers, fundamental solution, analytic integration, Method of continuous source functions (MCSF), force, dipole

Abstract. In this paper a new Method of Continuous Source Functions (MCSF) to modeling of such problems like composites reinforced with short fibers will be shown. The source functions (forces and dipoles) are continuously distributed along the fiber axis and their intensity (i. e. outside of the domain, which is the matrix) is modeled by 1D quadratic elements along the axis in order to satisfy boundary conditions. The continuity conditions simulating quasi-stiff fibers are given in the form of strains along the fiber axis (which is identical to difference of displacements in this direction) and by the difference of displacements in cross sectional directions. The method is not fully meshless for these particular models, as it requires 1D elements outside the 3D domain and 2D integration on fiber ends where continuous force is applied, however, the model presents significant reduction (even by several orders) of resulting system of equations comparing to FEM, BEM, or other known meshless methods and can be defined as a Mesh Reducing Method (MRM).
Comparing to the MFS, which does not require any integration, the MCFS requires integration along the 1D elements. The integrals are quasi-singular and quasi-hyper-singular and even though the numerical integration is computationally cumbersome it is necessary to use it partly in the computation together with analytic integration. The analytic integration using symbolic manipulation is very efficient tool used in the models.

Introduction. Composite structures where a soft matrix is reinforced by hard particles improve many properties of the matrix material. They have better stiffness, better wearing resistance and improved thermal and electrical properties. In order to improve existing materials there have to be an efficient method for assessment of optimal particles distribution, its size and shape inside of the matrix that would be necessary to achieve given goals. There are many computational methods which could be used, ranging from atomic structures in Molecular Dynamics (MD) to micro and macro structures which can be handled by conventional finite element method (FEM) or boundary element method (BEM). The limiting factors are of course the hardware insufficiency be it the CPU power or the amount of memory in the computer. If we go into smaller volumes where tiny particles are placed tightly one on another, then the number of these particles rapidly increases with increasing volume. Using conventional computational methods it would be very cumbersome to model and evaluate even few thousand particles in relatively small volume where in reality the number of particles could be few billions. In this case it is of course necessary to use multi-scale methods which are assessing properties of each fiber, interaction forces between the matrix and the fiber an interaction effects between the particles. Afterwards the information obtained from this high scale simulation will be used in lower scale levels where more material volume could be processed. In this paper a boundary method called Method of Continuous Source Functions (MCSF) is used to simulate very efficiently the behavior of the composite material including all interactions which occur in the material using continuous distribution of forces, dipoles or any other kind of source functions which satisfy the governing equation of the problem. It is a modification of the Method of Fundamental Solutions (MFS) [1,2] where the boundary conditions are satisfied in a collocation sense by using a set of point source functions and applying a theorem of linear combination on them so that the boundary conditions in chosen field points laying on the domain boundary would be a linear combination of all source functions acting outside of the domain. The resulting system of equations can be either square or rectangular depending on the number of source points and on the number of field points. If the number of source and field points is equal then we can solve the system

exactly. If there are more source points than field points that means we have more unknown quantities than equations then the only way to solve the system is by Singular Value Decomposition (SVD). If there is on the other hand more field points compared to source points which would mean there is more equations than unknown quantities, the system is satisfied in the least square sense by applying the Method of Least Squares (MLS) on the system. By the MCSF the source functions are distributed continuously along the axis of the fiber and therefore it is necessary to integrate only in one direction along the fiber to assemble the matrix of the system containing the unknown intensities of the functions. 2D numerical integration is used for continuous force with linear distribution which is applied on fiber ends. The integration in the radial direction is performed using Gaussian quadratures and the integration along the angle is done using equidistantly spaced elements with linear integration. The number of elements on which an integration is performed is much lesser compared to what MFS would require in terms of degrees of freedom for given accuracy threshold. The resulting system of equations is then solved in the least squares sense. The corresponding integral equations are quasi-singular and quasi-hyper-singular with large gradients and cannot be evaluated efficiently by numerical procedures however numerical integration was partly used together with analytical integration. An analytic integration is preferred for better performance and improved accuracy.

Source Functions. The field of displacements in an elastic continuum by a unit force acting in direction of the axis x_p is given by Kelvin solution

$$U_{pi}^{(F)} = \frac{1}{16\pi G\left(1-\nu\right)}\frac{1}{r}\left[\left(3-4\nu\right)\delta_{ip} + r_{,i}r_{,p}\right], \tag{1}$$

where i denotes the x_i coordinate of the displacement, G and ν are shear modulus and Poisson's ratio of the material of the matrix (isotropic material is considered here), r is the distance between the source point s, where the force is acting with a field point t, where the displacement is introduced

$$r = \sqrt{r_i r_i},\ \ r_i = x_i\left(t\right) - x_i\left(s\right) \tag{2}$$

with summation convection over repeated indices and

$$r_{,i} = \partial r \big/ \partial x_i\left(t\right) = r_i / r \tag{3}$$

is its directional derivative.

The gradients of displacement fields are corresponding derivatives of the field (1) in the point t

$$U_{pi,j}^{(F)} = -\frac{1}{16\pi G\left(1-\nu\right)}\frac{1}{r^2}\left[\left(3-4\nu\right)\delta_{pi}r_{,j} - \delta_{pj}r_{,i} - \delta_{ij}r_{,p} + 3r_{,i}r_{,j}r_{,p}\right] \tag{4}$$

Note that the second derivative of the radius vector of n-th power is

$$\left(r_{,k}^{n}\right)_{,j} = \frac{n}{r}\left(r_{,k}^{n-1}\delta_{jk} - r_{,j}r_{,k}^{n}\right) \tag{5}$$

The strains are

$$E_{pij}^{(F)} = \frac{1}{2}\left(U_{pi,j}^{(F)} + U_{pj,i}^{(F)}\right) = -\frac{1}{16\pi G\left(1-\nu\right)}\frac{1}{r^2}\left[\left(1-2\nu\right)\left(\delta_{pi}r_{,j} + \delta_{pj}r_{,i}\right) - \delta_{ij}r_{,p} + 3r_{,i}r_{,j}r_{,p}\right] \tag{6}$$

and the stress components ij of this field are

$$S_{pij}^{(F)} = 2GE_{pij}^{(F)} + \frac{2G\nu}{1-2\nu}\delta_{ij}E_{pkk}^{(F)} = \frac{1}{8\pi\left(1-\nu\right)}\frac{1}{r^2}\left[\left(1-2\nu\right)\left(\delta_{ij}r_{,p} - \delta_{jp}r_{,i} - \delta_{ip}r_{,j}\right) - 3r_{,i}r_{,j}r_{,p}\right] \tag{7}$$

where δ_{ij} is the Kronecker delta.

The displacement field of a dipole (two collinear point forces with opposite orientation) can be obtained from the displacement field of a force by differentiating it in the direction of the acting force, i.e.

$$U_{pi}^{(D)} = U_{pi,p}^{(F)} = -\frac{1}{16\pi G(1-\nu)}\frac{1}{r^2}\left[3r_{,i}r_{,p}^2 - r_{,i} + 2(1-\nu)r_{,p}\delta_{ip}\right] \tag{8}$$

The summation convection does not act over the repeated indices *p* here and in the following relations, too.

Gradients of displacement field are

$$\begin{aligned} U_{pi,j}^{(D)} = -\frac{1}{16\pi G(1-\nu)}\frac{1}{r^3}\Big[&-15r_{,i}r_{,j}r_{,p}^2 + 3r_{,i}r_{,j} + \\ &+2(1-2\nu)\delta_{ip}\left(\delta_{jp} - 3r_{,j}r_{,p}\right) + 6r_{,i}r_{,p}\delta_{jp} + \delta_{ij}\left(3r_{,p}^2 - 1\right)\Big] \end{aligned} \tag{9}$$

and corresponding strain and stress fields are

$$\begin{aligned} E_{pij}^{(D)} = \frac{1}{2}\left(U_{pi,j}^{(D)} + U_{pj,i}^{(D)}\right) = -\frac{1}{16\pi G(1-\nu)}\frac{1}{r^3}\Big[&-15r_{,i}r_{,j}r_{,p}^2 + 3r_{,i}r_{,j} + \\ &+2(1-2\nu)\delta_{ip}\delta_{jp} + 6\nu\left(\delta_{ip}r_{,j}r_{,p} + \delta_{jp}r_{,i}r_{,p}\right) + \delta_{ij}\left(3r_{,p}^2 - 1\right)\Big] \end{aligned} \tag{10}$$

$$\begin{aligned} S_{pij}^{(D)} = 2GE_{pij}^{(D)} + \frac{2G\nu}{1-2\nu}\delta_{ij}E_{pkk}^{(D)} = -\frac{1}{8\pi(1-\nu)}\frac{1}{r^3}\Big[&(1-2\nu)\left(2\delta_{ip}\delta_{jp} + 3r_{,p}^2\delta_{ij} - \delta_{ij}\right) + \\ &+6\nu r_{,p}\left(r_{,i}\delta_{jp} + r_{,j}\delta_{ip}\right) + 3\left(1-5r_{,p}^2\right)r_{,i}r_{,j}\Big] \end{aligned} \tag{11}$$

The displacements (1) by a force are weak singular, the displacement gradients, strains and stresses are strong singular. The fields defined by a dipole have one order higher singularity (strong in displacement and hyper-singular in strain and stress fields).

The Method of Continuous Source Functions. The fibers are considered with ratio of radius to length of 1:100 and 1:1000 in examples belov. The boundary of the fiber is also the inner boundary of the matrix. Continuity conditions have to be satisfied here according to which the unknown intensities of the source functions acting on the axis of the fiber are computed. If the fiber is very thin as in this case, a large number of discrete source functions would be necessary to satisfy the boundary conditions. Instead it is better to use continuous distribution of source functions along the axis of the fiber as it is in the MCSF. Both force and dipole source functions are used to satisfy the continuity conditions (Fig 1.).

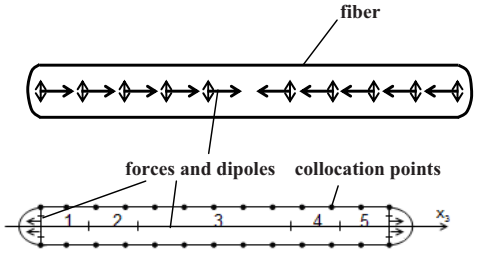

Figure 1: Continuous dipole model for fiber reinforcement

The source functions are approximated by polynomial functions and following integral has to be evaluated

$$\int_a^b \frac{x_s^n \left(x_s - x_f\right)^p}{\left(y^2 + x_s - x_f^2\right)^{\frac{m}{2}+r}} dx_s = f\left(x_f\right) \tag{12}$$

where x is the coordinate along the fiber axis, the subscripts s and f denote the source and field point and exponents are integers. For the computation the integral (12) is transformed for better manipulation to

$$\int_{a+x_f}^{b+x_f} \frac{\left(x + x_f\right)^n x^p}{\left(y^2 + x^2\right)^{\frac{m}{2}+r}} dx = f\left(x_f\right) \tag{13}$$

The numerical integration of the integrals is computationally very intensive, however, analytic evaluation of the integrals containing the kernel function and polynomial approximation of the unknown functions is an efficient way of handling complex functions.

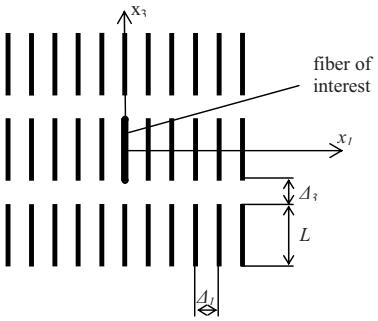

Figure 2: Patch of reinforcing fibers

Numerical results. In the numerical example are shown results for a patch of fibers reinforcing soft matrix with elastic modulus E=1000 and Poison number ν=0.3 (Fig. 2). The fiber of interest is placed in the middle to show reinforcing effect of the along its boundary. The length of the fiber is L=1000 and L=100. The radius R=1 and the spacing between the fibers in longitudinal direction is Δ_3=16R and in the perpendicular direction it is Δ_1=16R. A load in longitudinal direction with stress acting in infinite boundaries σ_{33}=10 was applied on the domain boundary. In Fig. 3 intensities of continuous source functions distributed along the axis of the fiber for the force and dipole distribution are shown.

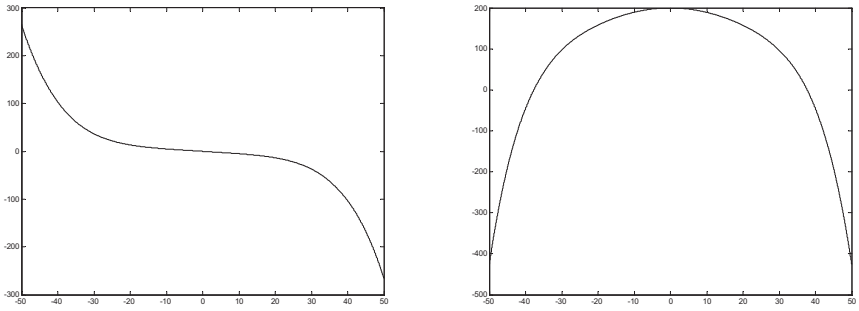

Figure 3: Intensity of the force source function (left) and dipole source function (right)

In Fig. 4 errors in displacement in radial and longitudinal direction for short and long fiber are shown.

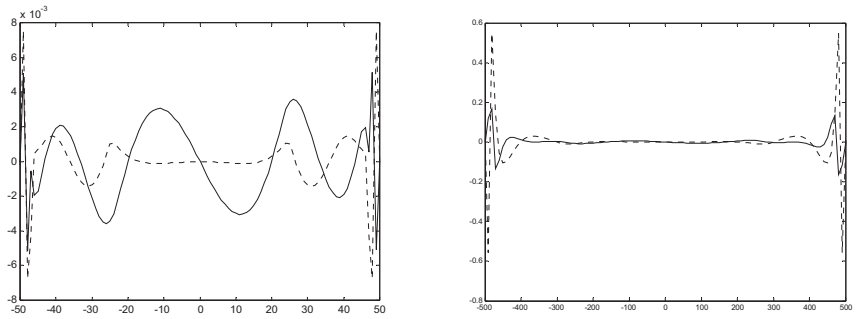

Figure 4: Errors in displacements u_3 (dashed line) and u_1 (solid line) for short fiber (left) and long fiber (right)

In Fig. 5 displacements in longitudinal direction for short and long fiber along the boundary of the fibers and in between fibers are shown.

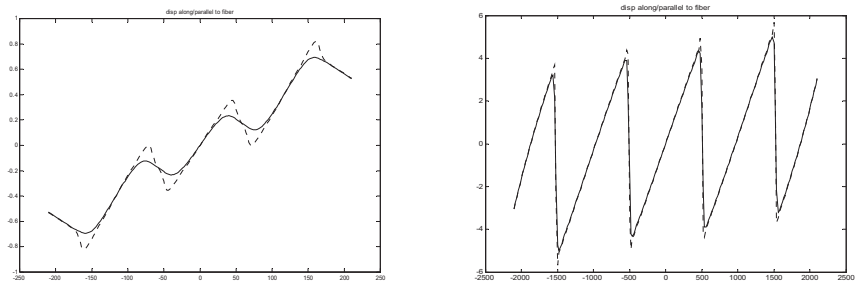

Figure 5: Displacements u_3 along the fibers boundaries (dashed line) and in between the fiber (solid line) for short fiber (left) and long fiber (right)

Conclusion. The paper presents the Method of Continuous Source Functions suitable for modeling of composite structures reinforced by short fibers in effective manner. For this purpose the force and dipole source functions were used but any type of source functions which satisfy the governing equation of the problem can be used [3-6]. 1D analytical integration of the continuous source functions distributed along the axis of the fiber was used in order to assemble the linear system of equations with unknown intensities of the source functions. 2D numerical integration was used for linearly distributed forces on the end parts of the fiber to catch the large gradients in the primary and secondary fields and thus improving accuracy of the model. All kind of interactions between fibers, fiber-matrix and the fiber-matrix boundary can be modeled efficiently this way. The source functions are quasi-singular along the fiber boundary. Very large gradients in the fields make the numerical integration inefficient and analytic integration is preferred. The analytic evaluation of integrals is simple also for higher order polynomial approximation of the intensities of the source functions.

References.

[1] Golberg M. A. and Chen C. S. The Method of Fundamental Solutions for Potential, Helmholtz and Diffusion Problems. *Boundary Integral Methods – Numerical and Mathematical Aspect,* Golberg M. A. Ed., Computational Mechanics Publications, Southampton, pp. 103-176, 1998.

[2] Karageorghis, A. and Fairweather, G. The method of fundamental solutions for the solution of nonlinear plane potential problems, *IMA Journal Numerical Analysis,* 9, pp. 231-242, 1989.
[3] V. I. Blokh. *Theory of Elasticity,* (in Russian), University Press, Kharkov, 1964
[4] M. Kachanov, B. Shafiro, I. Tsukrov. *Handbook of Elasticity Solutions*, Dordrecht: Kluwer Academic Publishers, 2003.
[5] C. Somigliana. Sulla Teoria delle Distorsioni Elastiche. *Note I e II Atti Accad Naz Lincei Classe Sci Fis e Nat* **23:** 463-472,1914 and **24**: 655-666, 1915.
[6] A. H.-D. Cheng, D. T. Cheng. Heritage and early History of the Boundary Element Method. *Eng. Anal. with Boundary Elements,* **29:** 268-302, 2005.

Dual Boundary Elements for Crack Propagation by Means of Linear Fracture Mechanics

Sonia Parvanova and Gospodin Gospodinov

Department of Civil Engineering, University of Architecture Civil Engineering and Geodesy
1 Hristo Smirnenski blv, 1046 Sofia, Bulgaria, slp_fce@uacg.bg, gospgosp_frf@uacg.bg

Keywords: Dual boundary elements, linear fracture mechanics, crack propagation, quasibrittle materials

Abstract This paper presents the numerical implementation of the dual boundary element method (DBEM) in the linear elastic fracture mechanics (LEFM) context for crack propagation in plain concrete. The main advantage of the DBEM is that multiple discrete crack problems can be solved successfully with a single region formulation. The method is combined with a previously developed two-step singularity subtraction technique (TSSST) for evaluation of stress intensity factors (SIFs). The crack growth condition requires a fracture criterion, which forms a simple numerical procedure along with the DBEM and TSSST, capable of treating the general problem of mixed-mode fracture. The accuracy and efficiency of the implementation, described herein, make this formulation very suitable to study the crack growth problems in plain concrete under a general mode I/II conditions.

Introduction It is well known that the nonlinear response of concrete is mainly dominated by progressive cracking which frequently results in local failure [1, 2, 3]. In general two principal approaches are used for the numerical modelling of cracks: discrete and smeared crack models. In the present study we employ the discrete crack modelling and some positive arguments for this choice are to be found in reference [6]. When the concrete shear beam is initially loaded flexural cracks are expected to develop under pure opening mode. It is relatively easy to analyse this type of cracking and calculate the stress intensity factor when the discrete crack model and LEFM are employed. The situation becomes more complex when a mixed-mode fracture develops, associated with a diagonal, usually known as shear or "critical" crack. The crack opening is combined with huge sliding and frictional forces, due to aggregate interlock over the both faces of the crack, in this respect a reliable numerical method is needed to study the problem.

The direct application of the classical BEM for 2D domain with edge or internal cracks is not possible, because the coincidence of the crack surfaces gives rise to a singular system of algebraic equations. Few techniques have been devised to overcome this difficulty, but it seems that the DBEM is most promising one, demonstrating many advantages. On the other hand, the method is very complex and requires unconditional application of discontinuous boundary elements and analytical treatment of the singular finite part integrals [1, 4]. In this study we use the dual boundary element method for linear, double node discontinuous boundary elements, already developed in paper [7]. In fact, the original idea of implementation of DBEM is dating back to 70-th for solving potential theory problems, but the method was refined by Aliabadi and others for the theory of elasticity and fracture mechanics applications – see references [1, 3, 4].

The successful implementation of the methods of LEFM for the direction of crack growth involves a definition and application of certain criterion and we use the maximum circumferential stress criterion [2], which proves to be suitable for mixed-mode case of deformations. However, it requires very accurate calculation of K_I and K_{II} SIFs for both fracture modes. We employ the TSSST, following the principal idea from paper [5], where the approach was employed for a single crack in mode I, by means of the sub-region decomposition. The crack path usually consists of number of linear segments with a chosen length and it is shown in [7] that it leads to very accurate results for SIFs required. Two examples of concrete beams are solved and analyzed and some comparisons are made.

1. The dual boundary element method using linear, double-node discontinuous boundary elements

The term *dual* for this variant of the boundary element method steams from the fact that the displacement boundary integral equations are used on the one crack surface, whereas the traction equations are applied on the other. In this way, avoiding the singular set of algebraic equations, we can simply treat a domain containing several edge as well as internal cracks, as a single one. Omitting details, the complete system of boundary integral equations are worked out to constitute the basis of the dual boundary element method at the crack point x_0' (see Fig. 1) of a smooth boundary, as follows [3, 4, 7]:

$$\frac{1}{2}u_j(x_0') + \frac{1}{2}u_j(x_0'') = \int_\Gamma u_{ij}^*(x_0', x)t_i(x)d\Gamma(x) - \int_\Gamma t_{ij}^*(x_0', x)u_i(x)d\Gamma(x),$$
$$\frac{1}{2}t_j(x_0') - \frac{1}{2}t_j(x_0'') = n_i(x_0')\int_\Gamma d_{kij}^*(x_0', x)t_k(x)d\Gamma(x) - n_i(x_0')\int_\Gamma s_{kij}^*(x_0', x)u_k(x)d\Gamma(x). \quad (1)$$

The indices i and j range from 1 to 2 and refer to the Cartesian coordinate directions; $u_j(x)$ and $t_j(x)$ are displacement and traction functions on the boundary Γ respectively; u_{ij}^* и t_{ij}^* represent the Kelvin displacement and traction fundamental solutions at a boundary point x; d_{kij}^* and s_{kij}^* are third-order fundamental tensors, derived as linear combinations of derivatives of Kelvin's tensors; $n_i(x_0')$ denotes the i-th coordinate of the unit normal to the boundary at point x_0'; the second integral of the first equation and the first integral of the second equation must be considered as Cauchy principal value integrals, whereas the last integral of the second integral equation is considered in a sense of Hadamard principal value integral.

It is important to note that when the collocation point x_0' is on the crack surface (say $u_j(x_0')$ in displacement equation or $t_j(x_0')$ in traction equation), an additional jump term $u_j(x_0'')$ or $t_j(x_0'')$ will appear, due to the coincident node x_0'' on the other crack surface, detailed explanations for which are given in [7].

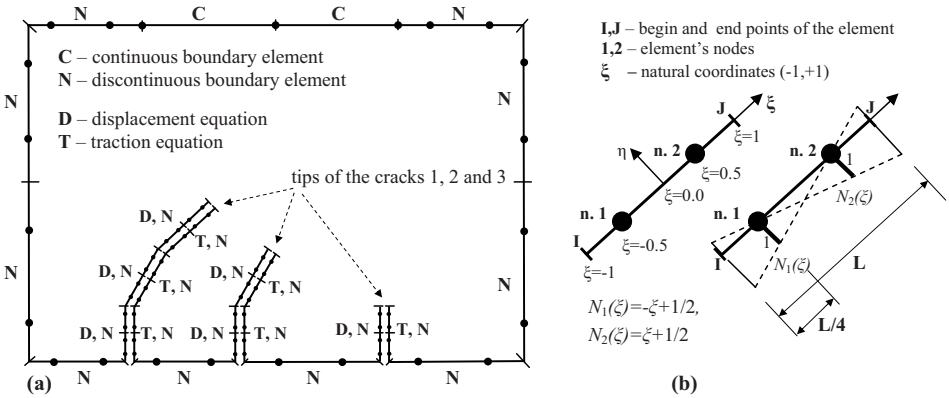

Fig. 1 ***(a)*** *Contour discretization using continuous and discontinuous boundary elements. Utilization of the dual integral equations for both surfaces of the crack.* ***(b)*** *Discontinuous double-node linear boundary element and its shape functions $N_1(\xi)$ and $N_2(\xi)$*

In Fig. 1 (a) a rectangular plane domain is shown with three multi-linear edge cracks. The boundary discretization of the crack faces modeled by double node discontinuous elements is also shown together with the element itself and its shape functions (Fig. 1 (b)). On the boundary Γ either continuous (C) and/or discontinuous (N) boundary elements could be employed. Also, there are no restrictions on the type of integral equations, displacement or traction, used. Operating on one of the crack surfaces two principal restrictions are to be met: (1) the dual system of integral equations must be used, namely displacement equations (denoted by D) on one side, and traction equations (denoted by T) on the other; (2) only discontinuous boundary elements must be employed for both crack faces. The above conditions are necessary for the existence of principal value integrals, assumed for the derivation of dual integral equations.

With the system of algebraic equations worked out and boundary functions available, one can find displacements and stresses for any point in the domain including the stresses at the crack tip or at any point near by.

2. Application of two-step singularity subtraction technique for the calculation of SIFs

The main feature of the classical singularity subtraction (SS) technique is the combination of the singular solution due to first term of the Williams series expansion, and the solution of the real problem, applying superposition principle. For simplicity, we refer to first and second step solutions with details given in [7]. The elastic stress field near the crack tip vicinity is singular (Fig. 2). Because of the convergence difficulties

arising in numerical modeling of the singular fields by the SS method these singularities are completely eliminated. As a result, the "regularization" process introduces the stress intensity factors (K_I and K_{II} for the mixed mode fracture) as additional unknowns for the original problem, therefore two extra conditions are needed to obtain a correct solution.

Suppose the stress tensor σ_{mn} at point *a* in the unprimed x_1x_2 coordinate system (Fig. 2 (a)) is known. If a virtual crack direction is defined at nonzero angle α, one can calculate the stress tensor σ'_{ij} in the primed coordinate system $x'_1x'_2$ (Fig. 3 (b)), by means of well known transformation formulas.

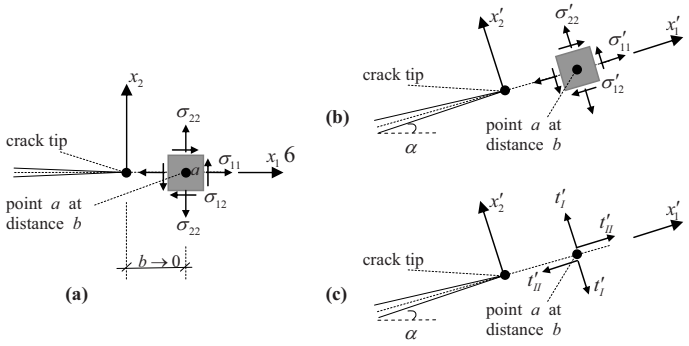

Fig. 2 ***(a)*** *Stresses at point a located at distance b→0 in front of the crack tip in* x_1x_2 *coordinate system;* ***(b)*** *Stresses at point a in coordinate system* $x'_1x'_2$ *;* ***(c)*** *Case (b) represented by means of tractions* t'_I *and* t'_{II} *at point a governing the opening and sliding fracture modes*

We assume that the crack propagates along the line of the last linear section pointing at *a* (Fig. 3 (c)). Furthermore, it is convenient to calculate the two tractions t'_i at point *a*, bearing in mind the obvious relationship $t'_I = \sigma'_{22}$ related to the definition of SIF for the opening mode I and $t'_{II} = \sigma'_{12}$ related to the definition of SIF for the sliding mode II.

In a linear elastic domain containing a discrete crack, the complete elastic solution is assumed to be a sum of two components: a regular part (denoted by *r* superscript) and a singular part (denoted by *s* superscript) due to the presence of the crack tip. Therefore, the solution can be rearranged for the displacement and stress tensors, as follows

$$\begin{aligned} u_i^r &= u_i - u_i^s \,, \\ \sigma_{ij}^r &= \sigma_{ij} - \sigma_{ij}^s \,. \end{aligned} \qquad (2)$$

Since the complete solution (u_i, σ_{ij}) and the singular part of it (u_i^s, σ_{ij}^s) include the mentioned singularity, it follows from equations (2) that the singularity is cancelled out, and the remaining component of the solution (u_i^r, σ_{ij}^r) is therefore regular.

It is important to point out that for the TSSST in the first step we perform a solution by DBEM for the actual geometry, load and boundary conditions to get u_i and σ_{ij} fields. In the second step, using *the same boundary element discretization*, the singular fields u_i^s and σ_{ij}^s are obtained for a reference value of SIF. The both solutions are "loaded" with error due to approximation of the boundary functions plus the presence of the crack tip, being a highly singular point. It follows therefore from equations (2), that as a result of subtraction the computational error is minimized [1, 5, 7].

With both solutions available, the traction t_i at a chosen point in the domain or at the boundary can be presented as follows:

$$t_i = \mathbf{K} t_i^s + t_i^r \quad , \quad or \quad t_i^r = t_i - \mathbf{K} t_i^s \quad , \qquad (3)$$

where $\mathbf{K}$ is the unknown SIF for mode I or II, t_i is the relevant traction from the real first step solution, t_i^s is the respective traction from the singular second step solution, and t_i^r denotes the traction assumed a regular function free from crack tip singularity, which actually is not needed to calculate.

In order to get the values of SIFs $\mathbf{K}$ additional equations are needed – one for each different fracture mode. These are known as the "singularity" conditions for the regularization procedure. It is very natural to define them for the crack tip point, where the regular traction t_i^r is zero and from eq. (3) follows that

$$t_i^r(r=0,\theta=0)=t_i-\mathbf{K}t_i^s=0 \quad , \quad (4) \quad \text{yielding the final result} \quad \mathbf{K}=\frac{t_i}{t_i^s} \quad . \quad (5)$$

The relationship (5) could be rewritten in expanded form, giving the formulas for the two stress intensity factors required:

$$K_I=\frac{t_I'}{t_I'^s} \quad , \quad (6) \quad \text{and} \quad K_{II}=\frac{t_{II}'}{t_{II}'^s} \quad . \quad (7)$$

It is shown in [7] how the above procedure can be generalized in order to use the method in the case of several traction free cracks.

3. Linear elastic fracture mechanics criterion and procedures for crack initiation and propagation in the case of mixed-mode fracture

The maximum circumferential stress criterion constitutes that the fracture initiation starts in direction in which the circumferential stress, near the crack tip, is maximum. According to this criterion [2], the direction of crack propagation angle θ_{cr} is the solution of the following equation

$$K_I/K_{II}\sin\theta_{cr}+(3\cos\theta_{cr}-1)=0 \quad , \quad (8)$$

where K_I and K_{II} are the stress intensity factors, calculated at the corresponding instant.

The crack initiation begins if the stress intensity factors and propagation angle θ_{cr} satisfy the following inequality [2]

$$K_I\cos^3\frac{\theta_{cr}}{2}-3K_{II}\cos^2\frac{\theta_{cr}}{2}\sin\frac{\theta_{cr}}{2}\geq K_{Ic} \quad , \quad (9)$$

where K_{Ic} is the fracture toughness for fracture mode I, which in case of plane stress can be derived from the fracture energy parameter G_f using the following relationship $K_{Ic}^2=EG_f$.

A simple algorithm and software code are developed for a quasi-static crack propagation involving a number of successive analyses. Each analysis consists of the following steps:

- Linear elastic numerical analysis is performed by the DBEM in order to find the strain and stress fields.
- Stress intensity factors K_I and K_{II} are calculated by means of the TSSST, given in section 2;
- The direction of crack propagation angle is then calculated from eq. (8). Since this formula needs a ratio of SIFs, there is no need to obtain the crack propagation load, so a reference load value is usually used;
- Once the propagation angle is calculated, the parametric equation (9) is satisfied in order to find the current crack propagation load, which helps to find the values of SIFs K_I , K_{II}; The respective displacements, stresses and tractions are updated accordingly;
- For a user defined crack-length increment, the location of the new crack tip is determined and the crack geometry and mesh are updated;
- A discretization is made along the new linear crack length performing consecutive static solution by the DBEM for a reference load;
- The above procedure is repeated until the user decides to stop the crack propagation, or if a certain desired location and crack length are arrived at.

4. Numerical results and conclusions

Two numerical simulations were conducted to demonstrate the ability of the presented method and they include a symmetric mode I fracture as well as mixed-mode crack propagation. Fig. 3 shows the classical example of a notched beam, subjected to three-point bending [3, 6]. Since the crack path is known we developed a LEFM solution taking the crack path increment of 5 mm. In Fig. 3 the load-deflection response curve is given for the present DBEM + TSSST solution as well as for the cohesive crack approach developed by the same authors for the case of one, two and three-linear stress-displacement softening models.

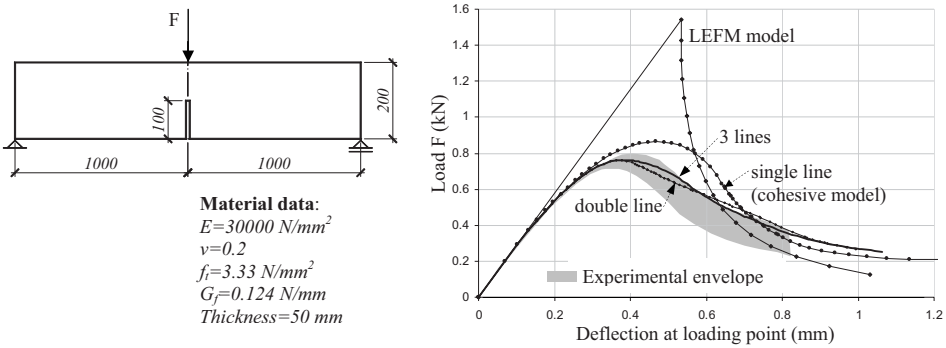

Fig. 3 *The notched unreinforced beam in mode I fracture – data and load-deflection response*

The experimental envelope, taken from reference [6], is also presented in order to estimate the numerical solutions. Omitting details for the LEFM solution (they can be found in [7]) and the cohesive models (the latter results are due to be accomplished and published), a conclusion can be made that the present LEFM model is a good first step for estimation of the real response. No doubt the cohesive models are better suited for the present material data. Some parametric studies have shown however that in case the material is more brittle the peak load may be very well simulated.

As a second example a case of mixed-mode fracture in a single notched concrete beam, tested by Arrea and Ingraffea [3, 6], is numerically solved and discussed. Fig. 4 (a) shows the geometrical configuration and material parameters of the shear beam. In the experiment a displacement control was used in order to obtain the descending branch of the load-displacement relationship. The initial vertical crack is of 82 mm length and plane stress condition was assumed. For this numerical test the complete DBEM plus TSSST were performed and the crack length increment was chosen 20 mm. Starting with the calculation of SIFs for the initial crack, the procedure for finding the direction of the new crack segment is performed by using eq. (8). The next step requires correction of the reference load to be used in the static DBEM solution, by means of eq. (9), followed by stress and displacement fields update.

Adding the new crack segment and updating the geometry and boundary element mesh, the next static solution is performed with the reference (usually unit) load. The above procedure is repeated until the final stage is reached. The calculation process is made interactive, so the user is able to run, stop, correct data and continue the program execution. For this example 13 crack length increments have been realized. In Fig. 4 (b) a picture of the experimental scatter for crack growth path is given along with the present numerical prediction. A good fitting between experimental and numerical data is observe although the methodology developed here is simple, based on the principles of the linear elastic fracture mechanics.

The diagrams given in Fig. 4 (c) show the vertical load-crack mouth sliding displacement relationship. The experimental envelope for the extreme values of fracture energy parameter (G_f=0.55-0.100 N/mm), taken from [6], and the present numerical predictions (for G_f=0.100 N/mm), are compared. Fair prediction for the descending curve is attained for the case of maximum value of fracture energy. Apparently the peak load is better simulated if the cohesive model is employed.

Some interesting results are plotted in Fig. 4 (d), where the load-vertical deflection responses are given. The snap-back phenomena, reported in the experiment, could be successfully captured by the present LEFM numerical approach since the crack length increments are used as a controlling parameter. There is significant deviation for the peak load, whereas good fitting is observed in the descending branch of the diagram. Again a comparison is made with the cohesive models.

Based on the above numerical experiments, comparisons and analyses of the results, the following conclusions may be written:

- The dual boundary element method combined with the two-step subtraction singularity technique, constitute a good, accurate and reliable numerical procedure for finding the real crack path trajectories for beams, made of plain concrete;
- We perform the regularization process with respect to crack tip point. That is exactly the point for which the calculations are correct;

- This technique is based on the principles of the LEFM and the formulated fracture criterion. It turns out being capable of predicting the phenomena of the crack growth in plain concrete, including the case of mixed-mode conditions;
- Although the main features of the deformation process and failure are portrayed, it is obvious that the problem is highly nonlinear and the real energy dissipation is not well reproduced. As a result there are some deviations for the critical peak load.

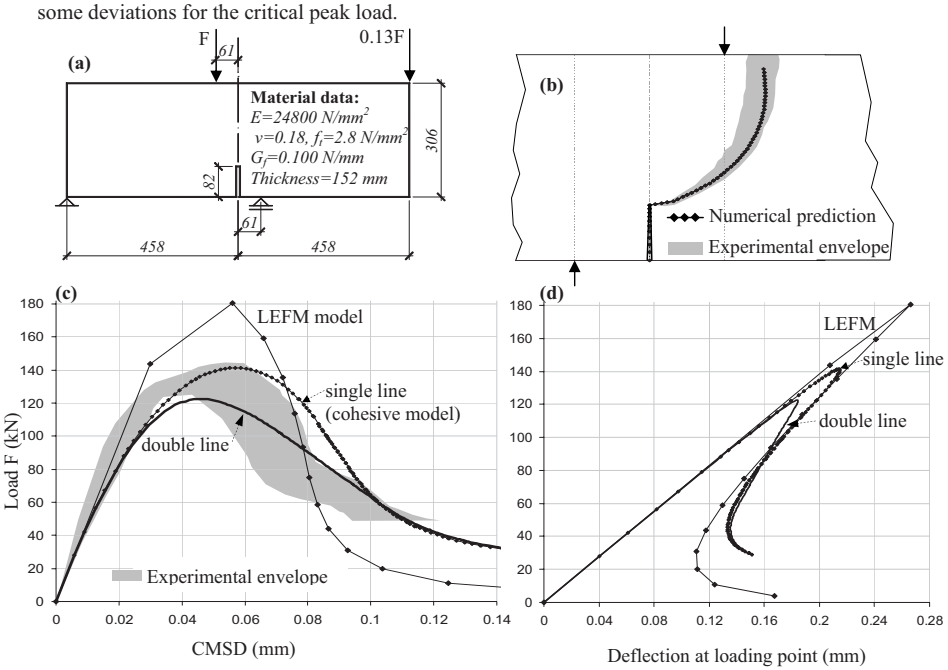

Fig. 4 ***(a)*** *Single notched shear beam;* ***(b)*** *The crack path prediction;* ***(c)*** *Load - crack mouth sliding displacement response;* ***(d)*** *Load - vertical deflection response with a sharp snap-back behaviour*

That paper is a part of doctoral work in progress and it is author's belief that the presented methodology is an important and necessary step for further development of the method. The results obtained for the crack path simulation of plain concrete beams under mixed-mode fracture are promising. They could serve as a good tool and basis for development of nonlinear fracture mechanics models, such as cohesive cracks approach as well as an extension to reinforced concrete simulation.

References

[1] M. Aliabadi and D. Rooke. *Numerical fracture mechanics*. Kluwer Academic Publishers, (1991).
[2] Z. Bazant, J. Planas. *Fracture and size effect in concrete and other quasibrittle materials*. CRC Press, LLC, (1998).
[3] A. L. Saleh. *Crack growth in concrete using boundary elements*. Computational mechanics publications, Volume 30, Southampton, (1997).
[4] A. Portela, M. Aliabadi and D. Rooke. *The dual boundary element method: effective implementation of crack problems.* Int. J. Num. Meth. Engng., 33(6), p. 1269-87, (1992).
[5] D. Della-Ventura, R.N.L. Smith. *Some application of singular fields in the solution of crack problems*. Int. J. Num. Meth. Engng., 42, p. 927-942, (1998).
[6] J. Rots, P. Nauta, G. Kusters, J. Blaauwendraad. *Smeared crack approach and fracture localization in concrete.* HERON, Vol. 30, No 1, (1985).
[7] S. Parvanova. *Application of the subtraction singularity approach to dual boundary element method* (in Bulgarian). Annual of UACEG, Sofia, Vol. XLIII, 2006-2007.

Acknowledgement Funding for the research described in this paper was supplied by the National Science Fund under the contract № TH – 1406/04. This support is gratefully acknowledged.

A Local Integral Equation Method for Dynamic Analysis in Functionally Graded Piezoelectric Materials

Jan Sladek[1], Vladimir Sladek[1] and Chuanzeng Zhang[2]

[1] Institute of Construction and Architecture, Slovak Academy of Sciences, 84503 Bratislava, Slovakia, email: sladek@savba.sk
[2] Department of Civil Engineering, University of Siegen, D-57068 Siegen, Germany, email: c.zhang@uni-siegen.de

Keywords: Imact loading, Laplace-transform, Stehfest's inversion, crack, functionally graded materials, piezoelectricity, meshless approximation.

Abstract. A meshless method based on the local Petrov-Galerkin approach is proposed for dynamic crack analysis in two-dimensional (2-D) piezoelectric solids with continuously varying material properties under dynamic loading. To eliminate the time-dependence, the Laplace-transform technique is applied to the governing partial differential equations which are satisfied in the Laplace-transformed domain in a weak-form on small fictitious subdomains. The nodal points are introduced and spread on the analyzed domain and each node is surrounded by a small circle for simplicity, but without loss of generality. The local integral equations (LIEs) have a very simple nonsingular form. The spatial variations of the Laplace-transforms of the displacements and the electric potential are approximated by the Moving Least-Squares (MLS) scheme. As electrical boundary conditions on the crack-surfaces, two extreme cases, namely impermeable and completely permeable electrical boundary conditions, are investigated. Numerical examples arte presented and discussed to show the accuracy of the present local integral equation method.

Introduction

The concept of functionally graded materials (FGMs) is becoming utilized in piezoelectricity to obtain desirable piezoelectric materials with high strength, high toughness, low thermal expansion coefficient and low dielectric constant. Devices such as actuators based on functionally graded piezoelectric materials (FGPMs) have been investigated by Zhu et al. [1,2]. The fracture of FGPMs under a thermal load has been studied by Wang and Noda [3]. Recently, the in-plane crack problem in FGPMs has been analyzed by Chen et al. [4] and Ueda [5]. To the best of the authors' knowledge, however, only very few papers like [6] are devoted to three-dimensional (3-D) analysis of electromechanical fields in FGPMs.

The solution of the boundary value problems for continuously nonhomogeneous piezoelectric solids requires advanced numerical methods due to the high mathematical complexity. The governing partial differential equations for FGPMs are much more complicated than that for their homogeneous counterpart, since the electric and the mechanical fields are coupled each other. Modern computational methods like the finite element method (FEM) [7-9] and the boundary element method (BEM) [10-13] have to be applied for general crack problems in homogeneous or nonhomogeneous piezoelectric solids. In spite of the great success of these effective numerical tools for the solution of boundary value problems in piezoelectric solids, there is still a growing interest in the development of new advanced numerical methods. In recent years, meshless formulations are becoming popular due to their high adaptivity and low cost in preparation of input and output data for numerical analyses. A variety of meshless methods has been proposed so far and some of them also applied to piezoelectric problems [14-15]. They can be derived either from a weak-form formulation on the global domain or a set of local subdomains. In the global formulation, background cells are required for the integration of the weak-form. In the methods based on the local weak-form formulation no background cells are required and therefore they are often referred to as truly meshless methods. The meshless local Petrov-Galerkin (MLPG) method is a fundamental base for the derivation of many meshless formulations, since trial and test functions can be chosen from different functional spaces. Recently, the MLPG method with a Heaviside step function as the test functions [16] has been applied to solve two-dimensional (2-D) homogeneous piezoelectric problems by the authors [17]. In the present paper, the MLPG is extended to continuously nonhomogeneous piezoelectric solids with cracks under transient dynamic

loading conditions. The coupled governing partial differential equations are satisfied in a weak-form on small fictitious subdomains. Nodal points are introduced and spread on the analyzed domain and each node is surrounded by a small circle for simplicity, but without loss of generality. If the shape of subdomains has a simple form, the numerical integrations over them can be easily carried out. The integral equations have a very simple nonsingular form. The spatial variations of the displacements and the electric potential are approximated by the Moving Least-Squares (MLS) scheme [16,18]. After performing the spatial integrations, a system of linear algebraic equations for unknown nodal values is obtained. The boundary conditions on the global boundary are satisfied by the collocation of the MLS-approximation expressions for the displacements and the electric potential at the boundary nodal points.

If cracks in piezoelectric solids are investigated, an important question is how the medium inside the crack is modeled. Depending on the ratio between the dielectric permittivity of the medium inside the crack and that of the piezoelectric solid, two extreme cases can be considered. In this first extreme case, the crack is not visible for the electric field if the permittivity of the medium inside the crack is significantly larger than that of the piezoelectric solid. In such a case the potentials on both crack-surfaces are the same, and thus one has the so-called electrically permeable boundary conditions on the crack-surfaces. In the second extreme case, the permittivity of the medium inside the crack is vanishing. Then, the electrical displacements on both crack-surfaces are vanishing and a potential jump occurs. This case corresponds to the so-called electrically impermeable boundary conditions. In a real situation, the electrical displacements on both crack-surfaces are proportional to the ratio of the potential jump and the distance of the crack-surfaces (crack-opening-displacement). Since the crack-opening-displacement is dependent on the value of the electrical displacement, the problem has to be solved iteratively.

Local boundary integral equations in Laplace-transformed domain

The governing equations for continuously nonhomogeneous and linear piezoelectric solids are given by the equations of motion for displacements and by the first Maxwell's equation for the electric displacements [19]

$$\sigma_{ij,j} + X_i = \rho \ddot{u}_i \,, \tag{1}$$

$$D_{j,j} - R = 0 \quad , \tag{2}$$

where $\ddot{u}_i$, σ_{ij} , D_i , X_i , R and ρ denote the acceleration, stress tensor, electric displacement, body force vector, volume density of free charges and mass density, respectively.

The constitutive relations expressing the coupling between the mechanical and the electrical fields are

$$\sigma_{ij}(\mathbf{x}) = c_{ijkl}(\mathbf{x})\varepsilon_{kl}(\mathbf{x}) - e_{kij}(\mathbf{x})E_k(\mathbf{x}) \,, \tag{3}$$

$$D_j(\mathbf{x}) = e_{jkl}(\mathbf{x})\varepsilon_{kl}(\mathbf{x}) + h_{jk}(\mathbf{x})E_k(\mathbf{x}) \,, \tag{4}$$

where $c_{ijkl}(\mathbf{x})$, $e_{jkl}(\mathbf{x})$ and $h_{jk}(\mathbf{x})$ are the elastic, the piezoelectric and the dielectric material tensors in a continuously nonhomogeneous piezoelectric medium, respectively.

The strain tensor ε_{ij} and the electric field vector E_j are related to the displacements u_i and the electric potential ψ by

$$\varepsilon_{ij} = \frac{1}{2}\left(u_{i,j} + u_{j,i}\right) \,, \tag{5}$$

$$E_j = -\psi_{,j} \,. \tag{6}$$

Applying the Laplace-transform to the governing equations, eq. (1), we obtain

$$\bar{\sigma}_{ij,j}(\mathbf{x}, p) - \rho(\mathbf{x}) p^2 \bar{u}_i(\mathbf{x}, p) = -\bar{F}_i(\mathbf{x}, p) \quad , \tag{7}$$

where p is the Laplace-transform parameter, and

$$\bar{F}_i(\mathbf{x}, p) = \bar{X}_i(\mathbf{x}, p) + p u_i(\mathbf{x}, 0) + \dot{u}_i(\mathbf{x}, 0) \,.$$

Instead of writing the global weak-form for the above governing equations, we apply the MLPG method to construct a weak-form over the local fictitious subdomains such as Ω_s, which is a small region taken for each node inside the global domain [16]. The local subdomains could be of any geometrical shape and size.

In the present paper, the local subdomains are taken to be of a circular shape. The local weak-form of the governing equations (7) can be written as

$$\int_{\Omega_s}\left[\overline{\sigma}_{ij,j}(\mathbf{x},p)-\rho(\mathbf{x})p^2\overline{u}_i(\mathbf{x},p)+\overline{F}_i(\mathbf{x},p)\right]u^*_{ik}(\mathbf{x})\,d\Omega\;=0\,, \tag{8}$$

where $u^*_{ik}(\mathbf{x})$ is a test function.

By choosing a Heaviside step function as the test function $u^*_{ik}(\mathbf{x})$ in each subdomain

$$u^*_{ik}(\mathbf{x})=\begin{cases}\delta_{ik} & \text{at } \mathbf{x}\in\Omega_s\\ 0 & \text{at } \mathbf{x}\notin\Omega_s\end{cases}$$

the local weak-form (8) is then converted into the following local boundary-domain integral equations

$$\int_{L_s+\Gamma_{su}}\overline{t}_i(\mathbf{x},p)d\Gamma-\int_{\Omega_s}\rho(\mathbf{x})p^2\overline{u}_i(\mathbf{x},p)d\Omega=-\int_{\Gamma_{st}}\tilde{\overline{t}}_i(\mathbf{x},p)d\Gamma-\int_{\Omega_s}\overline{F}_i(\mathbf{x},p)d\Omega\,, \tag{9}$$

where $\partial\Omega_s$ is the boundary of the local subdomains which consists of three parts $\partial\Omega_s=L_s\cup\Gamma_{st}\cup\Gamma_{su}$ [16]. It is noted that L_s is the local boundary that is totally inside the global domain, Γ_{st} is the part of the local boundary which coincides with the global traction boundary, i.e., $\Gamma_{st}=\partial\Omega_s\cap\Gamma_t$, and similarly Γ_{su} is the part of the local boundary that coincides with the global displacement boundary, i.e., $\Gamma_{su}=\partial\Omega_s\cap\Gamma_u$.

Note that the local integral equations (9) are valid for both homogeneous and nonhomogeneous linear piezoelelectric solids. Nonhomogeneous material properties are included in eq. (9) through the elastic and the piezoelectric tensors of the material in the traction components.

Similarly, the local weak form of the governing equation (2) in the Laplace transformed domain is given by

$$\int_{\Omega_s}\left[\overline{D}_{j,j}(\mathbf{x},p)-\overline{R}(\mathbf{x},p)\right]v^*(\mathbf{x})\,d\Omega\;=0\,, \tag{10}$$

where $v^*(\mathbf{x})$ is a test function.

Applying the Gauss divergence theorem to the local weak-form and considering the Heaviside step function for the test function $v^*(\mathbf{x})$, one obtains

$$\int_{L_s+\Gamma_{sp}}\overline{Q}(\mathbf{x},p)d\Gamma=-\int_{\Gamma_{sq}}\tilde{\overline{Q}}(\mathbf{x},p)d\Gamma+\int_{\Omega_s}\overline{R}(\mathbf{x},p)d\Omega\quad, \tag{11}$$

where

$$\overline{Q}(\mathbf{x},p)=\overline{D}_j(\mathbf{x},p)n_j=\left[e_{jkl}\overline{u}_{k,l}(\mathbf{x},p)-h_{jk}\overline{\psi}_{,k}(\mathbf{x},p)\right]n_j\,.$$

The trial functions are approximated by the Moving Least-Squares (MLS) method over a number of nodes spread within the domain of influence. The approximated functions for the Laplace-transforms of the mechanical displacements and the electric potential can be written as [16]

$$\overline{\mathbf{u}}^h(\mathbf{x},p)=\mathbf{\Phi}^T(\mathbf{x})\cdot\hat{\mathbf{u}}(p)=\sum_{a=1}^{n}\phi^a(\mathbf{x})\hat{\mathbf{u}}^a(p)\,,$$

$$\overline{\psi}^h(\mathbf{x},p)=\sum_{a=1}^{n}\phi^a(\mathbf{x})\hat{\psi}^a(p)\,, \tag{12}$$

where the nodal values $\hat{\mathbf{u}}^a(p)$ and $\hat{\psi}^a(p)$ are fictitious parameters for the displacements and the electric potential respectively, and $\phi^a(\mathbf{x})$ is the shape function associated with the node *a*. The number of nodes *n* used for the approximation is determined by the weight function $w^a(\mathbf{x})$. A 4th order spline-type weight function is applied in the present work.

Furthermore, in view of the MLS-approximations for the unknown quantities in the local boundary-domain integral equations (9) and (11), we obtain their discretized forms as

$$\sum_{a=1}^{n}\left(\int_{L_s+\Gamma_{su}}\mathbf{N}(\mathbf{x})\mathbf{C}(\mathbf{x})\mathbf{B}^a(\mathbf{x})d\Gamma-\rho(\mathbf{x})p^2\int_{\Omega_s}\phi^a(\mathbf{x})d\Omega\right)\hat{\mathbf{u}}^a(p)\;+\sum_{a=1}^{n}\left(\int_{L_s+\Gamma_{su}}\mathbf{N}(\mathbf{x})\mathbf{L}(\mathbf{x})\mathbf{P}^a(\mathbf{x})d\Gamma\right)\hat{\psi}^a(p)=$$

$$= -\int_{\Gamma_{st}} \tilde{\tilde{\mathbf{t}}}(\mathbf{x},p)d\Gamma - \int_{\Omega_s} \bar{\mathbf{F}}(\mathbf{x},p)d\Omega \ , \tag{13}$$

$$\sum_{a=1}^{n}\left(\int_{L_s+\Gamma_{sp}} \mathbf{N}_1(\mathbf{x})\mathbf{G}(\mathbf{x})\mathbf{B}^a(\mathbf{x})d\Gamma\right)\hat{\mathbf{u}}^a(p) \ - \sum_{a=1}^{n}\left(\int_{L_s+\Gamma_{sp}} \mathbf{N}_1(\mathbf{x})\mathbf{H}(\mathbf{x})\mathbf{P}^a(\mathbf{x})d\Gamma\right)\hat{\psi}^a(p) =$$

$$= -\int_{\Gamma_{sq}} \tilde{\tilde{Q}}(\mathbf{x},p)d\Gamma + \int_{\Omega_s} \bar{R}(\mathbf{x},p)d\Omega \ , \tag{14}$$

which are considered on the sub-domains adjacent to interior nodes as well as to the boundary nodes on Γ_{st} and Γ_{sq}. The matrices arising in both equations (13) and (14) follow from the constitutive equations (3), (4) and the MLS approximations (12).

Obeying the boundary conditions at those nodal points on the global boundary, where the displacements and the electrical potential are prescribed, and making use of the approximation formulae (12), one obtains the discretized forms of the boundary conditions as

$$\sum_{a=1}^{n}\phi^a(\boldsymbol{\zeta})\hat{\mathbf{u}}^a(p) = \tilde{\tilde{\mathbf{u}}}(\boldsymbol{\zeta},p) \ \text{ for } \ \boldsymbol{\zeta}\in\Gamma_u \, , \tag{15}$$

$$\sum_{a=1}^{n}\phi^a(\boldsymbol{\zeta})\hat{\psi}^a(p) = \tilde{\tilde{\psi}}(\boldsymbol{\zeta},p) \ \text{ for } \ \boldsymbol{\zeta}\in\Gamma_p \, . \tag{16}$$

The time-dependent values of the transformed physical quantities can be obtained by an inverse Laplace-transform. There are many inversion methods available for the Laplace-transform. In the present analysis the Stehfest's algorithm is used.

Numerical examples

In the first example a straight central crack in a homogeneous finite strip under a uniform pure mechanical loading is analyzed (Fig. 1). Homogeneous material properties are selected to test the present computational method. The strip is subjected to an impact loading with Heaviside time variation and the loading amplitude is $\sigma_0 = 1Pa$. The material coefficients of the strip correspond to the PZT-4 material

$c_{11} = 13.9\cdot 10^{10}\, Nm^{-2}$, $c_{12} = 7.43\cdot 10^{10}\, Nm^{-2}$, $c_{22} = 11.5\cdot 10^{10}\, Nm^{-2}$, $c_{44} = 2.56\cdot 10^{10}\, Nm^{-2}$,

$e_{15} = 12.7\, Cm^{-2}$, $e_{21} = -5.2\, Cm^{-2}$, $e_{22} = 15.1\, Cm^{-2}$,

$h_{11} = 6.46\cdot 10^{-9}\, C(Vm)^{-1}$, $h_{22} = 5.62\cdot 10^{-9}\, C(Vm)^{-1}$, $\rho = 7500\,\mathrm{kg/m^3}$.

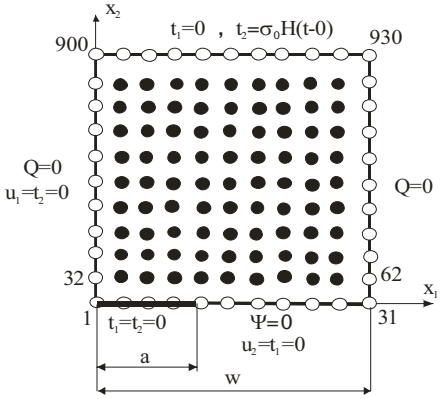

Fig. 1: Central crack in a finite piezoelectric strip

The cracked strip has the following geometrical parameters: width $w = 1.25a$, crack length $2a = 1.0m$ and height $h = 1.2w$. Due to the symmetry of the problem with respect to the crack line, only a quarter of the strip is numerically analyzed. The mechanical displacement and the electrical potential fields in the quarter of the strip are approximated by using 930 (31x30) nodes equidistantly distributed.
When cracks in piezoelectric solids are investigated, an important question is how to prescribe electric boundary conditions on the crack-surfaces. For completely permeable conditions

$\psi^+ = \psi^-$, $D_n^+ = D_n^-$,

the crack is not visible for the electric field. Contrary, completely impermeable boundary conditions lead to vanishing electrical displacements

$D_n^+ = D_n^- = 0$.

Realistic electrical boundary conditions are between the above mentioned two extreme cases. The dielectric property of the medium inside the crack is described by constants $h = \mathbf{h}_r \cdot \mathbf{h}_0$, where $\mathbf{h}_0$ is the permittivity of the vacuum inside the crack and $\mathbf{h}_r$ is a relative permittivity. The dielectric law gives

$$D_n^+ = D_n^- = -h\frac{\psi^+ - \psi^-}{u_n^+ - u_n^-}.$$

Since the mechanical displacements and the electric potential are dependent on the electric displacement, an iterative solution procedure is needed to handle this kind of electrical boundary conditions.
Kuna [9] analyzed the Griffith crack problem under various electric boundary conditions on crack-surfaces. He observed that the two extreme electric boundary conditions have a vanishing influence on the stress intensity factors (SIFs) at a pure mechanical load. However, the electrical displacement intensity factor is significantly influenced by the electric boundary conditions. Similar phenomena are observed in our results as presented in Fig. 2 for the normalized dynamic stress intensity factor K_I / K_I^{stat} and the normalized electrical displacement intensity factor $\Lambda K_{IV} / K_I^{stat}$, where $K_I^{stat} = 1.4\text{Pa} \cdot \text{m}^{1/2}$ for the considered geometry and loading, and $\Lambda = e_{22} / h_{22}$. The electrical displacement intensity factor (EDIF) is higher for permeable electric boundary conditions than for the impermeable ones.

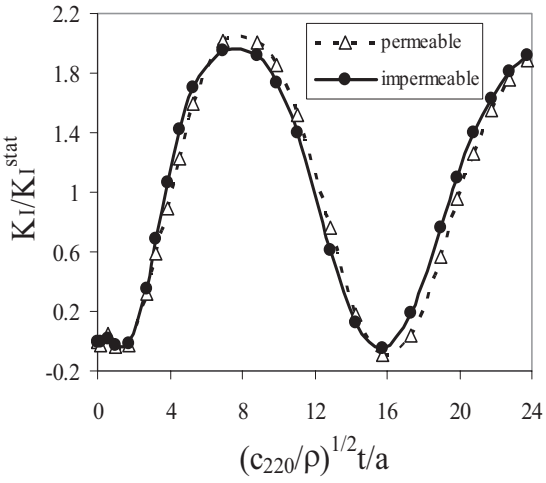

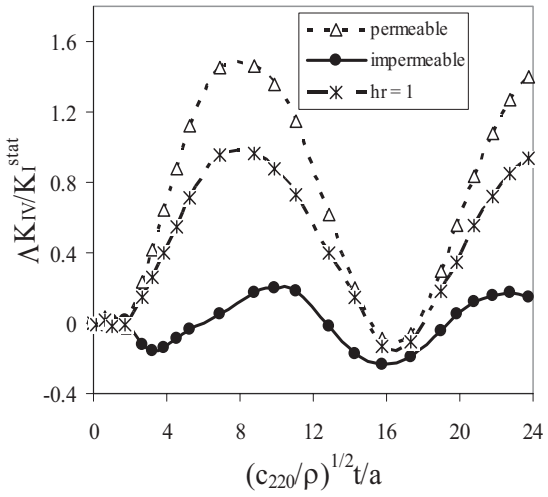

Fig. 2: Normalized dynamic intensity factors for a central crack in a piezoelectric strip under a pure mechanical impact loading

In the next example an edge crack in a finite piezoelectric strip is analyzed. The strip geometry is the same as in the previous example. Due to the symmetry with respect to x_1-axis only a half of the strip is modeled. We have used 930 nodes equidistantly distributed for the MLS-approximation of the physical fields. On the top of the strip a uniform impact tension $\sigma = \sigma_0 \cdot H(t)$ with a Heaviside time variation is applied.

Functionally graded material properties in the x_1-direction are considered. Exponential variations for the elastic, the piezoelectric and the dielectric tensors are assumed as

$$c_{ijkl}(\mathbf{x}) = c_{ijkl0}\exp(\gamma x_1), \qquad e_{ijk}(\mathbf{x}) = e_{ijk0}\exp(\gamma x_1), \qquad h_{ij}(\mathbf{x}) = h_{ij0}\exp(\gamma x_1),$$

where c_{ijkl0}, e_{ijk0} and h_{ij0} correspond to the material parameters used in the previous example.

Here again, we use the two extreme electrical boundary conditions on the crack-surfaces. Numerical results for the normalized dynamic SIF and the normalized dynamic EDIF are given in Figs. 3 and 4, respectively. The normalized dynamic SIF remains almost the same for both the permeable and the impermeable boundary conditions in homogeneous and continuously nonhomogeneous piezoelectric solids. The variation of the normalized dynamic EDIF for permeable electrical boundary conditions is similar to the variation of the normalized dynamic SIF.

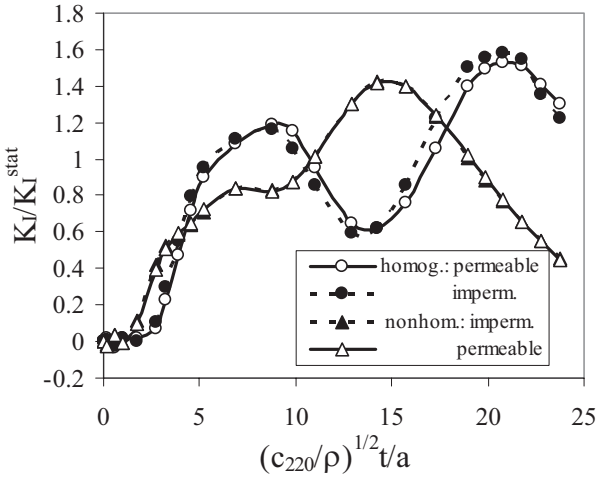

Fig. 3 Time variation of the normalized dynamic stress intensity factor

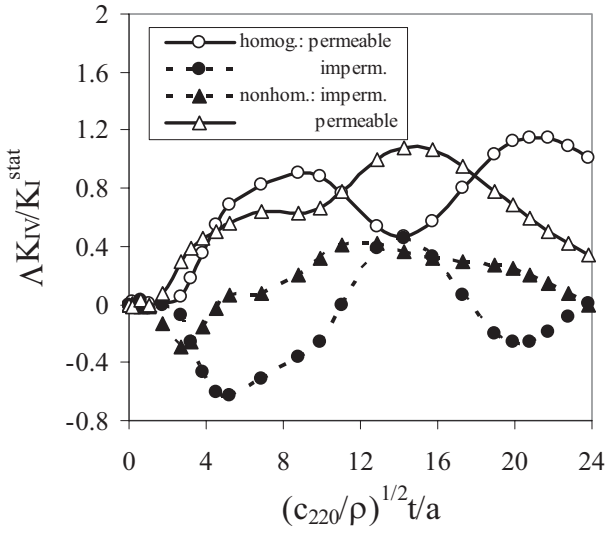

Fig. 4 Time variation of the normalized dynamic electrical displacement intensity factor

For a positive value of the gradation parameter γ of the mechanical material properties in the x_1-direction and a uniform mass density, the wave propagation velocity is growing with x_1-coordinate. Therefore, the first peak value of the dynamic SIF is reached at a shorter time instant in FGPM strip than in a homogeneous one. The maximum value of the dynamic SIF is only slightly reduced for the cracked FGPM strip compared to that of the cracked homogeneous strip.

Acknowledgements

This work is supported by the German Research Foundation (DFG) under the project number ZH 15/6-1, Slovak Science and Technology Assistance Agency registered under number APVV-51-021205, APVV-20-035404 and the Slovak Grant Agency VEGA-2/6109/6, which is gratefully acknowledged.

References

[1] X. Zhu, Z. Wang, A. Meng *Journal of Material Science Letter* **14**, 516-518 (1995).

[2] X. Zhu, J. Zhu, S. Zhou, Q. Li, Z. Liu *Sensor and Actuators A* **74**, 198-202 **(**1999).

[3] B.L. Wang, N. Noda *Theoretical Applied Fracture Mechanics* **35**, 93-109 (2001).

[4] J. Chen, Z.X. Liu, Z.Z. Zou *Theoretical Applied Fracture Mechanics* **39**, 47-60 (2003).

[5] S. Ueda *Theoretical Applied Fracture Mechanics* **40**, 225-236 (2003).

[6] W.Q. Chen, Y. Lu, G.R. Ye, J.B. Cai *Archive of Applied Mechanics* **72**, 39-51 (2002).

[7] O. Gruebner, M. Kamlah, D. Munz *Engneering Fracture Mechanics* **70**, 1399-1413 (2003)

[8] M. Enderlein, A. Ricoeur, M. Kuna *International Journal of Fracture* **134**, 191-208 (2005)

[9] M. Kuna *Archives of Applied Mechanics* **76**, 725-745 (2006).

[10] E. Pan Engineering *Analysis with Boundary Elements* **23**, 67-76 (1999).

[11] D. Gross, T. Rangelov, P. Dineva *SID: Structural Integrity & Durabil*ity **1**, 35-47 (2005).

[12] F. Garcia-Sanchez, Ch. Zhang, J. Sladek, V. Sladek *Computational Materials Science* **39**, 179-186 (2007).

[13] N. Sheng, K.Y. Sze *Computational Mech*anics **37**, 381-393 (2006).

[14] R.R. Ohs, N.R. Aluru *Computational Mechanics* **27**, 23-36 (2001).

[15] G.R. Liu, K.Y. Dai, K.M. Lim, Y.T. Gu *Computational Mechanics* **29**, 510-519 (2002).

[16] S.N. Atluri *The Meshless Method, (MLPG) For Domain & BIE Discretizations*, Tech Science Press (2004).

[17] J. Sladek, V. Sladek, Ch. Zhang, F. Garcia-Sanchez, M. Wunsche *CMC: Computer, Materials & Continua* **4**, 109-118 (2006).

[18] T. Belytschko, Y. Krongauz, D. Organ, M. Fleming and P. Krysl *Computer Methods in Applied Mechanics and Engineering* **139**, 3-47 (1996).

[19] V.Z. Parton, B.A. Kudryavtsev *Electromagnetoelasticity, Piezoelectrics and Electrically Conductive Solids*, Gordon and Breach Science Publishers, New York (1988).

BEM Thermoelastic Fracture Mechanics Analysis of Thin, Multi-Layered Anisotropic Structures

Y.C. Shiah[1], C.L Tan[2]

[1]Dept. of Aerospace and Systems Eng., Feng Chia University,
100 Wenhwa Rd., Seatwen 407, Taichung, Taiwan, R.O.C.

Email: ycshiah@fcu.edu,tw

[2] Dept. of Mechanical & Aerospace Engineering, Carleton University,
1125 Colonel By Drive, Ottawa, Canada K1S 5B6

Email: ctan@mae.carleton.ca

Keywords: Anisotropic thermoelasticity, fracture mechanics, thin multi-layered structures.

Abstract. The fracture mechanics analysis of de-bond interface cracks between thin, multi-layered anisotropic materials using the BEM is presented in this paper. In the formulation, the nearly-singular integrals in the boundary integral equation when treating very thin bodies are fully regularized using integration by parts. For straight elements, these integrals can be analytically integrated. Quarter-point elements with the appropriate oscillatory stress singularity at the interface crack-tip are also employed. Two numerical examples are presented to demonstrate the applicability of the algorithm developed.

Introduction

Material systems involving several thin layers of anisotropic solids bonded together occur in many modern engineering applications. They include laminated structural composites, thin film-substrate systems in electronic devices, thermal barrier coatings in turbine blades and adhesive joints. Under thermal loading, the mismatch of the coefficients of thermal expansion between the layers gives rise to inter-laminar stresses along their interfaces. A common failure mode of these components under such loads is de-bonding at these interfaces.

The finite element method (FEM) and the boundary element method (BEM) are two computational techniques commonly employed in engineering stress analysis. When computing the stress intensity factors (SIF's) of interface cracks between thin layers of anisotropic materials, difficulties associated with the oscillatory stress singularity at the bi-material interface crack-tip may be encountered [1]. Also, when analysing these problems involving very thin layers, appropriate aspect ratios of the discrete elements in the mesh are required to ensure reliable results; a consequence of this is the need for very refined mesh designs. To the authors' knowledge, the facility to directly compute the SIF's for interface cracks between dissimilar anisotropic materials remain absent in most, if not all, commercial FEM codes in spite of their long history of use in general engineering analysis. In the BEM formulation for thermoelastic stress analysis, a true boundary integral equation (BIE) can be obtained by transforming the domain integral associated with the thermal loads into a series of boundary ones [2]. For treating problems of thin, slender bodies using the BEM, however, the boundary integrals are nearly-singular and it is well-known that conventional numerical integration schemes will not yield accurate solutions. Several schemes have been proposed over the years to overcome this difficulty by regularizing the BIE (see, e.g. [3]-[6]), with the aim of accuracy, numerical efficiency, generality and simplicity. They have been met with varying degrees of success. Recently, the present authors [7] proposed a semi-analytical approach applying integration by parts to regularize the boundary integrals for anisotropic thermoelasticity. In this paper, the BEM with this regularization scheme is employed for the fracture mechanics analysis of de-bond cracks between dissimilar thin anisotropic layers subjected to thermal loads. Two example problems are considered for illustration below. Before presenting the results, however, a review of the BEM scheme is in order.

Regularized BIE formulation

The present authors has shown in ref. [2] that the domain integral associated with thermal effects in classical BIE formulations for 2D anisotropic elasticity can also be fully transformed into a series of boundary ones. Following the usual discretisation process of the boundary S into M elements and the assumed variations of

the field solutions and geometry over each of them with n^{th}-order shape functions, $N^{(c)}$, the discretised BIE relating the nodal displacements u_j and tractions t_j at the boundary S of the homogeneous elastic domain, can be expressed in terms of the local coordinate $\xi \in [-1,1]$ of the elements as

$$
\begin{aligned}
& C_{ij}(P^a)\, u_i(P^a) \\
&= \sum_{b=1}^{M}\sum_{c=1}^{n+1} {}^{b}t_i^c \int_{-1}^{1} U_{ij}(P^a, {}^{b}Q) N^{(c)}(\xi)\, J(\xi)\, d\xi \; - \sum_{b=1}^{M}\sum_{c=1}^{n+1} {}^{b}u_i^c \int_{-1}^{1} T_{ij}(P^a, {}^{b}Q) N^{(c)}(\xi)\, J(\xi)\, d\xi \\
&+ \sum_{b=1}^{M}\sum_{c=1}^{n+1} {}^{b}\Theta^c \int_{-1}^{1} \gamma_{ik}\, n_k U_{ij}(P^a, {}^{b}Q)\, N^{(c)}(\xi) J(\xi)\, d\xi - \sum_{b=1}^{M}\sum_{c=1}^{n+1} {}^{b}\Theta^c \int_{-1}^{1} \gamma_{\underline{ik}}\, n_{\underline{k}} U_{\underline{ij}}(P^a, {}^{b}Q)\, N^{(c)}(\xi) \hat{J}(\xi)\, d\xi \\
&+ \sum_{b=1}^{M}\sum_{c=1}^{n+1} {}^{b}\Theta^c \int_{-1}^{1} \gamma_{\underline{ik}} n_{\underline{l}} Q_{\underline{ijk},\underline{l}}(P^a, {}^{b}Q)\, N^{(c)}(\xi) \hat{J}(\xi)\, d\xi - \sum_{b=1}^{M}\sum_{c=1}^{n+1} {}^{b}\Theta^c_{,\underline{l}} \int_{-1}^{1} \gamma_{\underline{ik}}\, n_{\underline{l}} Q_{\underline{ijk}}(P^a, {}^{b}Q)\, N^{(c)}(\xi) \hat{J}(\xi)\, d\xi
\end{aligned} \tag{1}
$$

where the underline denotes properties defined in a mapped domain [2] in which the thermal field is treated as an equivalent isotropic one; $J(\xi)$ and $\hat{J}(\xi)$ represent the Jacobian transformation of the original and the mapped domain, respectively; γ_{ik} are the thermal moduli; n_i is the unit outward normal at Q; Θ is the temperature change; and $N^{(c)}$ is the shape function of nth degree for the c-th node expressed as

$$N^{(c)}(\xi) = \sum_{m=0}^{n} \alpha_m^{(c)} \xi^m \tag{2}$$

where $\alpha_m^{(c)}$ is the interpolation coefficient. Also in Eq.(1), the value of $C_{ij}(P)$ depends upon the local geometry of S at the source point P; $U_{ij}(P,Q)$ and $T_{ij}(P,Q)$ are the fundamental solutions of displacements and tractions, respectively, given by

$$U_{ij}(P,q) = 2\,\mathrm{Re}\left\{ r_{i1}\, A_{j1} \log z_1 + r_{i2}\, A_{j2} \log z_2 \right\} \tag{3a}$$

$$T_{1j} = 2n_1\,\mathrm{Re}\left\{ \mu_1^2\, A_{j1}/z_1 + \mu_2^2\, A_{j2}/z_2 \right\} - 2n_2\,\mathrm{Re}\left\{ \mu_1\, A_{j1}/z_1 + \mu_2\, A_{j2}/z_2 \right\} \tag{3b}$$

$$T_{2j} = -2n_1\,\mathrm{Re}\left\{ \mu_1\, A_{j1}/z_1 + \mu_2\, A_{j2}/z_2 \right\} + 2n_2\,\mathrm{Re}\left\{ A_{j1}/z_1 + A_{j2}/z_2 \right\} \tag{3c}$$

In addition, r_{ij} and A_{jk} are constants associated with the material properties; and

$$Q_{\underline{ijk}} = 2\,\mathrm{Re}\{ r_{i1}\, A_{j1}\, \mu_{\underline{k}1}\, z_1 \log(z_1) / (\mu_{\underline{1}1}{}^2 + \mu_{\underline{2}1}{}^2) + r_{i2}\, A_{j2}\, \mu_{\underline{k}2}\, z_2 \log(z_2) / (\mu_{\underline{1}2}{}^2 + \mu_{\underline{2}2}{}^2) \} \tag{4a}$$

$$Q_{\underline{ijk},\underline{l}} = 2\,\mathrm{Re}\{ r_{i1}\, A_{j1}\, \mu_{\underline{k}1}\, \mu_{\underline{l}1} (\log z_1 + 1) / (\mu_{\underline{1}1}{}^2 + \mu_{\underline{2}1}{}^2) + r_{i2}\, A_{j2}\, \mu_{\underline{k}2}\, \mu_{\underline{l}2} (\log z_2 + 1) / (\mu_{\underline{1}2}{}^2 + \mu_{\underline{2}2}{}^2) \} \tag{4b}$$

The operator $\mathrm{Re}\{\ \}$ in the equations shown gives the real part of complex variables; z_i are generalized complex variables defined in terms of the characteristic roots, $\mu_{k.}$, and the local coordinates of the field point, (ζ_1, ζ_2), with the origin set at the source point $P(x_{p1}, x_{p2})$ as follows

$$z_k = (x_1 - x_{p1}) + \mu_k (x_2 - x_{p2}) = \zeta_1 + \mu_k \zeta_2 \tag{5}$$

The kernels U_{ij} and T_{ij} are weakly singular and strongly singular, respectively; $Q_{\underline{ijk},\underline{l}}$ is weakly singular and $Q_{\underline{ijk}}$ is nonsingular. As described in [7], the weakly singular integral associated with U_{ij} can be regularized using integration by parts to have a form,

$$\sum_{c=1}^{n} {}^{b}t_i^c \int_{-1}^{1} 2\,\mathrm{Re}\left[r_{ik} A_{jk} \log {}^{b}z_k \right] N^c(\xi)\, J(\xi) d\xi = \sum_{c=1}^{n} {}^{b}t_i^c\, 2\,\mathrm{Re}\left[r_{ik} A_{jk} \left\{ \left[w(\xi) v_k(\xi) \right]_{-1}^{1} - \int_{-1}^{1} v_k(\xi) \cdot \Omega^{(c)}(\xi) d\xi \right\} \right] \tag{6}$$

where

$$w(\xi) = \sum_{m=0}^{n} \alpha_m^{(c)} \xi^m J(\xi), \tag{7a}$$

$$v_k(\xi) = \xi \log(B_{nk}) + \sum_{l=1}^{n} (\xi - R_{lk}) \left[\log(\xi - R_{lk}) - 1 \right], \tag{7b}$$

$$\Omega^{(c)}(\xi)=\sum_{t=1}^{n} t\alpha_t^{(c)}\xi^{t-1}J(\xi)+\frac{\sum_{t=0}^{n}\sum_{k=0}^{2n}\sum_{m=0}^{k}\sum_{i,j=1}^{n+1}(n-m)(n+m-k)(2n-k-2)\alpha_{n-m}^{(i)}\alpha_{n+m-k}^{(j)}\alpha_t^{(c)}x_l^{(i)}x_l^{(j)}\xi^{2n+t-k-3}}{2J(\xi)}\quad , \tag{7c}$$

$$B_{mk}=\sum_{c=1}^{n+1}\alpha_m^{(c)}\left({}^{b}x_1^{(c)}+\mu_k\,{}^{b}x_2^{(c)}\right), \tag{8}$$

and R_{ik} are roots of the polynomial equation,

$$\left[B_{0k}-\left({}^{b}x_{p_1}+\mu_k\,{}^{b}x_{p_2}\right)\right]/B_{nk}+\sum_{m=1}^{n}B_{mk}\xi^m/B_{nk}=0 \tag{9}$$

The second integral term in Eq. (1) containing T_{ij} can be analytically integrated [7] to give

$$\begin{aligned}&\sum_{c=1}^{n+1}\sum_{i=1}^{2}{}^{b}u_i^c\int_{-1}^{1}(-1)^{(i-1)}2\mathrm{Re}\left[\mu_k^{\delta_{1i}}A_{jk}\left(\frac{n_1\mu_k-n_2}{{}^{b}z_k}\right)\right]N^{(c)}(\xi)J(\xi)\,d\xi\\&=\sum_{c=1}^{n+1}\sum_{i=1}^{2}{}^{b}u_i^c(-1)^{(i-1)}2\mathrm{Re}\left[\mu_k^{\delta_{1i}}A_{jk}\sum_{j=1}^{n}\sum_{m=0}^{n}\alpha_m^{(c)}G_{jk}^{(c)}\left(\sum_{l=0}^{m-1}\frac{R_{jk}^{l}\xi^{m-l}}{m-l}+R_{jk}^{m}\log(\xi-R_{jk})\right)\right]_{-1}^{1}\end{aligned} \tag{10}$$

where

$$G_{jk}=\sum_{c=1}^{n+1}\sum_{m=1}^{n}m\alpha_m^{(c)}R_{jk}^{m-n-1}\left(x_2^{(c)}\mu_k+x_1^{(c)}\right)/B_{nk}\prod_{m=1}^{n}\left(1-R_{mk}/R_{jk}+R_{mk}\delta_{mj}/R_{jk}\right) \tag{11}$$

Similar analytical integration process may be followed for the remaining integrals in Eq.(1); this results in

$$\begin{aligned}&\sum_{c=1}^{n+1}{}^{b}\Theta^c\int_{-1}^{1}\gamma_{ik}\,n_k U_{ij}(P^a,{}^{b}Q)N^{(c)}(\xi)J(\xi)\,d\xi\\&=\sum_{c=1}^{n+1}{}^{b}\Theta^c\,\mathrm{Re}\left[\left[2\gamma_{ik}(-1)^{k+1}\sum_{c=1}^{n+1}\sum_{m=1,l=0}^{n}m\alpha_m^{(c)}\alpha_l^{(c)}\hat{x}_{1+\delta_{k1}}^{(c)}\left[\frac{\xi^{m+l}}{m+l}\,{}^{(c)}\log B_{nl}+\sum_{f=0}^{m+l-1}\frac{(-1)^f(m+l-1)!}{(m+l-1-f)!}\xi^{m+l-1-f}\right.\right.\right.\\&\left.\left.\left.(\xi-R_{fl})\left(E_{f+1}\log(\xi-R_{fl})-F_{f+1}\right)\right]_{-1}^{1}\right]\end{aligned} \tag{12a}$$

$$\begin{aligned}&\sum_{c=1}^{n+1}{}^{b}\Theta^c\int_{-1}^{1}\gamma_{\underline{ik}}n_{\underline{t}}Q_{\underline{ijk}\cdot\underline{t}}(P^a,{}^{b}Q)N^{(c)}(\xi)\hat{J}(\xi)\,d\xi\\&=\sum_{c=1}^{n+1}{}^{b}\Theta^c\,\mathrm{Re}\left[\left[\frac{2\gamma_{\underline{ik}}(-1)^{k+1}r_{ig}A_{jg}\mu_{\underline{kg}}\mu_{\underline{tg}}\hat{x}_{1+\delta_{t1}}}{\left(\mu_{\underline{1g}}{}^{2}+\mu_{\underline{2g}}{}^{2}\right)}\sum_{c=1}^{n+1}\sum_{m=1,l=0}^{n}m\alpha_m^{(c)}\alpha_l^{(c)}\right.\right.\\&\left.\left.\left[\frac{\left(1+\log B_{ng}\right)}{m+l}\xi^{m+l}+\sum_{f=0}^{m+l-1}\frac{(-1)^f(m+l-1)!}{(m+l-1-f)!}\xi^{m+l-1-f}\left(\xi-R_{fg}\right)^{f+1}\left[E_{f+1}\log(\xi-R_{fg})-F_{f+1}\right]\right]_{-1}^{1}\right]\end{aligned} \tag{12b}$$

where the coefficients E_{f+1}, F_{f+1} are defined by the following recursive formulae,

$$E_{f+1}=\frac{1}{(f+1)!}\quad,\quad F_{f+1}=\frac{F_f}{(f+1)}+\frac{E_f}{(f+1)^2}\quad,\quad (E_0=F_0=1) \tag{13}$$

With these, all nearly singular integrals in the BIE for anisotropic thermoelasticity can be accurately computed.

It is well established in BEM linear elastic analysis of fracture problems that the use of the traction-singular quarter-point crack-tip elements will yield accurate SIF's in the quadratic isoparametric element formulation. For an interface crack between dissimilar anisotropic materials, a modified shape function for the tractions on the

quarter-point crack-tip element was developed by Tan, *el al.* [1] to incorporate the oscillatory stress singularity at the crack-tip. The mode I and mode II stress intensity factors, K_I and K_{II}, respectively, can then be calculated directly from the following equation:

$$\mathbf{K} = \begin{bmatrix} K_{II}(L) \\ K_I(L) \end{bmatrix} = \sqrt{2\pi l} \cdot \mathbf{R}' \left[\left(\frac{L}{l} \right)^{i\gamma} \right] \cdot \begin{bmatrix} \hat{t}_1^{(1)} \\ \hat{t}_2^{(1)} \end{bmatrix}, \tag{14}$$

where l is the length of the crack-tip element, and L represents a characteristic dimension of the physical problem; and $\hat{t}_i^{(1)}$ are the computed traction coefficients at the crack-tip node. In Eq. (14), the coefficient γ and matrix $\mathbf{R}'$ are related to the elastic constants of the bi-material; their explicit forms are given in [1]. Also, the strain energy release rate, G, can be expressed as

$$G = \frac{1}{4} \mathbf{K}^{\mathrm{T}} \tilde{\mathbf{D}}^{-1} \mathbf{K}. \tag{15}$$

where, again, the matrix $\tilde{\mathbf{D}}$ is a matrix associated with the elastic constants of the bi-material [1]. In the numerical examples that follow, the characteristic length L is taken to be the crack length modeled.

Numerical examples

Two numerical examples are treated here. Due to the lack of availability of commercial FEM software to compute the SIF's of interface cracks between dissimilar anisotropic materials, the conventional BEM approach [1] with very refined meshes is employed for comparison of the results in the current study. The first example is shown in Fig. 1(a); it is a double-layered strip with a small de-bond edge crack subjected to a temperature change, ΔT. The upper layer is taken to be isotropic silicon (but analysed as quasi-isotropic using the anisotropic algorithm); the bottom layer is single crystal alumina (Al_2O_3). Following the usual notation with asterisk denoting properties in the direction of principal axes, their material properties are listed below.

$$\text{Alumina}: E_{11}^* = E_{33}^* = 345\ \text{GPa}, E_{22}^* = 516\,\text{GPa}, G_{12}^* = G_{23}^* = 173\,\text{GPa}, G_{31}^* = 173\ \text{GPa},$$
$$\nu_{12}^* = 0.131, \nu_{13}^* = 0.362, \nu_{23}^* = 0.196$$
$$\alpha_{11}^* = \alpha_{33}^* = 8.1\times10^{-6}/^0C, \alpha_{22}^* = 6.2\times10^{-6}/^0C, \eta_{12,1}^* = 0.59, \eta_{12,2}^* = 0.0, \eta_{12,3}^* = -0.59$$
$$\text{Silicon}: E = 130.3\ \text{GPa}, \nu = 0.278, \alpha = 2.59\times10^{-6}/^0C$$

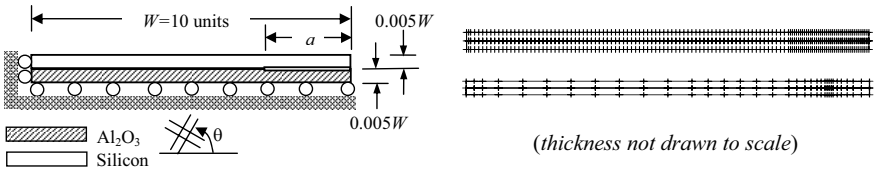

Figure 1: Example 1 (a) An edge crack in a double-layered strip; (b) BEM refined and coarse meshes

To demonstrate capability of treating general anisotropy, the principal axes are rotated by an angle θ = 30° counterclockwise with respect to the x-axis as shown in the figure. The fracture analysis is carried out for three different relative crack sizes, namely, a/W = 0.025, 0.05 and 0.1. Two mesh designs are considered in each case, a refined mesh and a coarser one. Figure 1(b) shows the two mesh designs in the BEM modeling for the particular case of a/W = 0.1. In the refined mesh, all element lengths away from the crack-tip are in the same order of magnitude as the thickness and there are 488 quadratic isoparametric elements for this case. This is to ensure good solution accuracy when using the conventional boundary integral equation (CBIE) formulation [1]. The coarser mesh has 136 elements for this case, with more refinement near the interface crack-tip. The analysis is carried out with the CBIE and the regularized boundary integral equation (RBIE) algorithms. Table 1 shows that comparison of the computed SIF's, normalized by $K_0 = E_{11}^* \alpha_{11}^* \Delta T \sqrt{\pi a}$, and the strain energy release rate G, as normalized by G_0 defined in [1]. For the alumina considered, $G_0 = 0.0069596\ K_0^2$. As can be seen in the table,

Table 1: Example 1- Comparison of normalized SIF's and energy release rates

$\theta=30^0$		Refined Mesh			Coarse Mesh			
		CBIE	RBIE		CBIE		RBIE	
	a/W	Normalized Value	Normalized Value	% Diff.	Normalized Value	% Diff.	Normalized Value	% Diff.
K_I/K_0	0.025	0.04260	0.04284	0.57	0.02878	32.5	0.04280	0.47
	0.050	0.03118	0.03081	1.19	0.01118	64.1	0.03126	0.27
	0.100	0.02013	0.02065	2.59	-0.00438	122.	0.01981	1.58
K_{II}/K_0	0.025	-0.06041	-0.06053	0.20	-0.06473	7.15	-0.06061	0.33
	0.050	-0.04326	-0.04337	0.26	-0.04962	14.7	-0.04348	0.53
	0.100	-0.03141	-0.03085	1.42	-0.03939	25.4	-0.03153	0.77
G/G_0	0.025	0.00330	0.00332	0.64	0.00303	8.17	0.00332	0.71
	0.050	0.00172	0.00171	0.55	0.00157	8.53	0.00173	0.82
	0.100	0.00084	0.00083	0.49	0.00097	16.0	0.00084	0.21

Table 2: Example 2 - Comparison of normalized SIF's and energy release rate for Tip 1

$\theta=30^0$		Refined Mesh			Coarse Mesh			
		CBIE	RBIE		CBIE		RBIE	
Tip 1	a/W	Normalized Value	Normalized Value	% Diff.	Normalized Value	% Diff.	Normalized Value	% Diff.
K_I/K_0	0.025	0.05185	0.05177	0.16	0.06622	27.7	0.05209	0.47
	0.050	0.04140	0.04140	0.00	0.04939	19.3	0.04169	0.70
	0.100	0.02948	0.02949	0.07	0.02776	5.82	0.02956	0.27
K_{II}/K_0	0.025	0.03420	0.03416	0.11	-0.00545	116.	0.03364	1.64
	0.050	0.02493	0.02501	0.33	0.00939	62.3	0.02435	2.33
	0.100	0.01780	0.01779	0.03	0.00312	75.1	0.01756	1.33
G/G_0	0.025	0.00115	0.00115	0.00	0.00122	6.08	0.00114	0.87
	0.050	0.00070	0.00069	0.10	0.00071	1.43	0.00069	1.43
	0.100	0.00035	0.00035	0.00	0.00022	39.1	0.00035	0.45

Table 3: Example 2-Comparison of normalized SIF's and energy release rate for Tip 2

$\theta=30^0$		Refined Meshes			Coarse Meshes			
		CBIE	RBIE		CBIE		RBIE	
Tip 2	a/W	Normalized Value	Normalized Value	% Diff.	Normalized Value	% Diff.	Normalized Value	% Diff.
K_I/K_0	0.025	0.05867	0.05867	0.00	0.03424	41.6	0.05815	0.89
	0.050	0.04739	0.0474	0.01	0.03454	27.1	0.04682	1.20
	0.100	0.03360	0.03357	0.06	0.01805	46.3	0.03340	1.20
K_{II}/K_0	0.025	-0.02944	-0.02943	0.01	-0.07712	162.	-0.03012	2.31
	0.050	-0.02042	-0.02050	0.41	-0.03312	62.2	-0.02107	3.18
	0.100	-0.01498	-0.01497	0.04	-0.01250	16.5	-0.01535	2.48
G/G_0	0.025	0.00116	0.00116	0.09	0.00202	74.1	0.00116	0.00
	0.050	0.00072	0.00072	0.00	0.00062	13.9	0.00071	1.39
	0.100	0.00037	0.00037	0.08	0.00013	64.3	0.00038	2.80

the RBIE algorithm with coarse meshes yields consistent results throughout while the same is not true with the CBIE when using the coarse meshes.

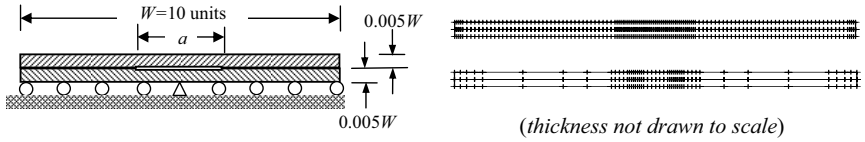

Figure 2: Example 2- (a) A central crack in a double-layered structure, (b) BEM refined and coarse meshes

Figure 2(a) shows the second example treated. It is an alumina bi-crystal wafer with a central crack, subjected to a uniform temperature change ΔT; the principal axes are rotated by $+\theta$ and $-\theta$ for the upper and the lower layers, respectively, with $\theta = 30^{o}$. A similar analysis as in the previous example is carried for the same relative crack sizes of a/W = 0.025, 0.05 and 0.1, using refined and correspondingly coarser meshes. Figure 2(b) shows mesh designs for the particular case of a/W =0.1; there are 500 quadratic elements employed for the refined mesh and 188 elements for the coarser mesh. The computed values of K_{I}, K_{II}, G for the left crack tip (Tip 1), and the right one (Tip 2), are listed in Table 2 and Table 3, respectively. Again, excellent consistency of the numerical results is observed for the RBIE results, in contrast with significant deviations between those obtained with the refined and coarse meshes when using the CBIE algorithm.

Conclusions

By applying the BIE regularized by the scheme of integration by parts and analytical integration, BEM fracture mechanics analysis of cracked thin layered anisotropic bodies subjected to thermal loading has been carried out in this investigation. Two numerical examples have been presented to demonstrate the usefulness of the regularized BIE algorithm where it was shown that excellent results for the stress intensity factors could still be obtained with relatively coarser mesh designs, in contrast to the conventional BEM algorithms.

Acknowledgement

The first author gratefully acknowledges the financial support of the National Science Council of Taiwan, Republic of China. (Grant Number: NSC-95-2221-E-035-025)

References

[1] Tan, C. L., Y. L. Gao, and F. F. Afagh, "Boundary element analysis of interface cracks between dissimilar anisotropic materials," *Int. J. Solids Structures,* Vol. 29, No. 24, pp. 3201-3220 (1992).

[2] Shiah, Y. C. and Tan, C. L., "Exact boundary integral transformation of the thermoelastic domain integral in BEM for general 2D anisotropic elasticity," *Computational Mech.,* Vol. 23, pp. 87-96 (1999).

[3] Tanaka, M, V. Sladek, V., and J. Sladek, J., "Regularization techniques applied to boundary element methods, *Appl. Meh. Rev*., Vol. 47, pp. 457-499 (1994).

[4] Krishnasamy, G., Rizzo, F.J. and Liu, Y.J., "Boundary integral equation for thin bodies", *Int. J. Num. Methods Engng.*, Vol. 37, 107-121 (1991).

[5] Richardson, J.D. and Cruse, T.A., "Weakly singular stress-BEM for 2D elastostatics" , *Int. J. Num. Methods Engng.*, Vol. 45, 13-35 (1999).

[6] Granados, J.J. and Gallego, R., "Regularization of nearly singular integrals in the boundary element method", *Engng. Anal. Boundary Elements,* 25 165-184 (2001).

[7] Shiah, Y. C., Lin, Y. C., and C. L. Tan, " Boundary element stress analysis of thin layered anisotropic bodies," *CMES- Computer Modeling in Engineering & Sciences*, Vol. 16, no. 1, pp.15-26 (2006).

Analysis of Plates Stiffened by Parallel Beams with Deformable Connection

[1]E.J.Sapountzakis and [2]V.G. Mokos

[1]School of Civil Engineering, National Technical University, Zografou Campus, GR-157 80 Athens, Greece, email:cvsapoun@central.ntua.gr

[2]email:vgmokos@central.ntua.gr

Keywords: Elastic stiffened plate, reinforced plate with beams, bending, nonuniform torsion, warping, ribbed plate, boundary element method, slab-and-beam structure

Abstract. In this paper a general solution for the analysis of plates stiffened by arbitrarily placed parallel beams of arbitrary cross section with deformable connection subjected to an arbitrary loading is presented. The adopted model describes better the actual response of the plate beams system and permits the evaluation of the shear forces at the interfaces in both directions, the knowledge of which is very important in the design of prefabricated ribbed plates. Numerical examples of great practical interest demonstrate the influence of the interface slip to the behavior of the stiffened plate while the accuracy of the obtained results compared with those obtained from FEM solutions is verified.

1. Introduction

Structural plate systems stiffened by beams are widely used in buildings, bridges, ships, aircrafts and machines. According to the proposed model, the stiffening beams are isolated from the plate by sections in the lower outer surface of the plate, making the hypothesis that the plate and the beams can slip in all directions of the connection without separation (i.e. uplift neglected) and taking into account the arising tractions at the fictitious interfaces. The aforementioned integrated tractions result in the loading of the beams as well as the additional loading of the plate. Their distribution is established by applying continuity conditions in all directions at the interfaces taking into account their relation with the interface slip through the shear connector stiffness. Any distribution of connectors in each direction of the interfaces can be handled. The analysis of both the plate and the beams is accomplished on their deformed shape taking into account second-order effects. Six boundary value problems are formulated and solved using the Analog Equation Method (AEM), a BEM based method. The solution of the aforementioned plate and beam problems, which are nonlinearly coupled, is achieved using iterative numerical methods.

The essential features and novel aspects of the present formulation compared with previous ones are summarized as follows.

i. The stiffened plate is subjected to an arbitrary loading, while both the number and the placement of the parallel stiffening beams are also arbitrary (eccentric beams are also included).
ii. The influence of the transverse traction component at plate-beams interfaces is taken into account. A nonuniform variation of its distribution is taken into account by applying compatibility equations on points in the transverse direction.
iii. Displacement continuity conditions, taking into account the deformable connection of the plate and the beams, are applied along all three axes of the coordinate system.
iv. The eccentricities of both the centroid and the shear center axes with respect to the midline of the plate – beam interface are also included.
v. The nonuniform torsion in which the stiffening beams are subjected is taken into account by solving the corresponding problem and by comprehending the arising twisting and warping in the corresponding displacement continuity conditions.
vi. Terms arising from the internal variable axial loading of both the plate and the beams coming from the longitudinal and transverse inplane shear forces at the interfaces are taken into account.

2. Statement of the problem

Consider a thin plate of homogeneous, isotropic and linearly elastic material with modulus of elasticity E and Poisson ratio ν, having constant thickness h_p and occupying the two dimensional multiply connected region Ω of the x,y plane bounded by the piecewise smooth $K+1$ curves $\Gamma_0,\Gamma_1,...,\Gamma_{K-1},\Gamma_K$,

as shown in Fig.1. The plate is stiffened by a set of $i=1,2,...,I$ arbitrarily placed nonintersecting beams of homogeneous, isotropic and linearly elastic material with modulus of elasticity E_b^i and Poisson ratio ν_b^i, which may have either internal or boundary point supports. For the sake of convenience the x axis is taken parallel to the beams. The stiffened plate is subjected to the lateral load $g=g(x,y)$. For the analysis of the aforementioned problem a global coordinate system Oxy for the analysis of the plate and local coordinate ones $O_i x_i y_i$ and $O_i \tilde{x}_i \tilde{y}_i$ corresponding to the centroid and shear center axes of each beam are employed as shown in Fig.1.

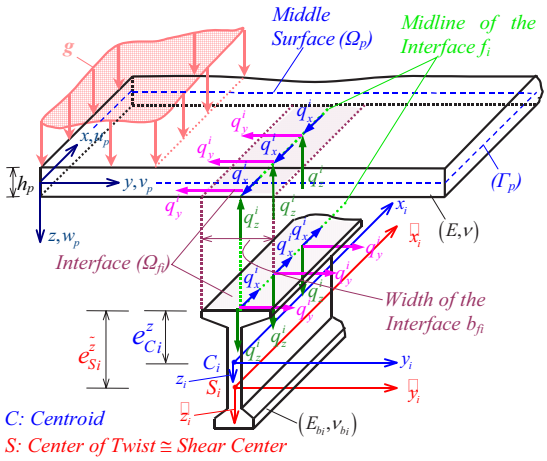

Fig.1. Isolation of the beams from the plate.

The solution of the problem at hand is approached by a refined model of that proposed by Sapountzakis and Katsikadelis in [1]. According to this model, the stiffening beams are isolated from the plate by sections in the lower outer surface of the plate, taking into account the arising tractions at the fictitious interfaces (Fig.1). Integration of these tractions along the width of the i-th beam results in line forces per unit length, which are denoted by q_x^i, q_y^i and q_z^i encountering in this way the influence of the transverse component q_y, which in the aforementioned model [1] was ignored. The aforementioned integrated tractions result in the loading of the i-th beam as well as the additional loading of the plate. Their distribution is unknown and can be established by imposing displacement continuity conditions at the interfaces along x_i, y_i and z_i local axes following the procedure developed in this investigation.

On the base of the above considerations the response of the plate and of the beams may be described by the following boundary value problems.

a. For the plate.

The plate undergoes transverse deflection and inplane deformation. Thus, for the transverse deflection the equation of equilibrium employing the linearized second order theory can be written as

$$D\nabla^4 w_p - \left(N_x \frac{\partial^2 w_p}{\partial x^2} + 2N_{xy} \frac{\partial^2 w_p}{\partial x \partial y} + N_y \frac{\partial^2 w_p}{\partial y^2} \right) = g - \sum_{i=1}^{I} \left(q_z^i + \frac{\partial m_{py}^i}{\partial x} - q_x^i \frac{\partial w_p}{\partial x} - q_y^i \frac{\partial w_p}{\partial y} \right) \delta(y - y_i) \quad \text{in } \Omega \qquad (1)$$

and the corresponding boundary conditions as

$$\alpha_{p1} w_p + \alpha_{p2} R_{pn} = \alpha_{p3} \qquad \beta_{p1} \frac{\partial w_p}{\partial n} + \beta_{p2} M_{pn} = \beta_{p3} \qquad \text{on } \Gamma \qquad (2a,b)$$

where $w_p = w_p(x,y)$ is the transverse deflection of the plate; $D = Eh_p^3 / 12(1-\nu^2)$ is its flexural rigidity; $N_x = N_x(x,y)$, $N_y = N_y(x,y)$, $N_{xy} = N_{xy}(x,y)$ are the membrane forces per unit length of the plate cross section; $\delta(y-y_i)$ is the Dirac's delta function in the y direction; M_{pn} and R_{pn} are the bending moment

normal to the boundary and the effective reaction along it, respectively, and a_{pi}, β_{pi} $(i=1,2,3)$ are functions specified on the boundary Γ, formulating the most general boundary conditions for the plate problem including also the elastic support.

Since linearized plate bending theory is considered, the components of the membrane forces N_x, N_y, N_{xy} are given as

$$N_x = C\left(\frac{\partial u_p}{\partial x} + \nu\frac{\partial v_p}{\partial y}\right) \qquad N_y = C\left(\nu\frac{\partial u_p}{\partial x} + \frac{\partial v_p}{\partial y}\right) \qquad N_{xy} = C\frac{1-\nu}{2}\left(\frac{\partial u_p}{\partial y} + \frac{\partial v_p}{\partial x}\right) \tag{3a,b,c}$$

where $C = Eh_p/\left(1-\nu^2\right)$; $u_p = u_p(x,y)$, $v_p = v_p(x,y)$ are the displacement components of the middle surface of the plate arising from the line body forces q_x^i, q_y^i ($i=1,2,...I$). These displacement components are established by solving independently the plane stress problem, which is described by the following boundary value problem (Navier's equations of equilibrium)

$$\nabla^2 u_p + \frac{1+\nu}{1-\nu}\frac{\partial}{\partial x}\left[\frac{\partial u_p}{\partial x} + \frac{\partial v_p}{\partial y}\right] - \frac{1}{Gh_p}\sum_{i=1}^{I} q_x^i \delta(y-y_i) = 0 \tag{4a}$$

$$\nabla^2 v_p + \frac{1+\nu}{1-\nu}\frac{\partial}{\partial y}\left[\frac{\partial u_p}{\partial x} + \frac{\partial v_p}{\partial y}\right] - \frac{1}{Gh_p}\sum_{i=1}^{I} q_y^i \delta(y-y_i) = 0 \qquad \text{in } \Omega \tag{4b}$$

$$\gamma_{p1}u_{pn} + \gamma_{p2}N_n = \gamma_{p3} \qquad \delta_{p1}u_{pt} + \delta_{p2}N_t = \delta_{p3} \qquad \text{on } \Gamma \tag{5a,b}$$

in which $G = E/2(1+\nu)$ is the shear modulus of the plate; N_n, N_t and u_{pn}, u_{pt} are the boundary membrane forces and displacements in the normal and tangential directions to the boundary, respectively; γ_{pi}, δ_{pi} $(i=1,2,3)$ are functions specified on the boundary Γ.

b. For each beam.

Each beam undergoes transverse deflection with respect to z_i and y_i axes, axial deformation along x_i axis and nonuniform angle of twist along $\tilde{x}_i$ axis. Thus, for the transverse deflection with respect to z_i axis the equation of equilibrium employing the linearized second order theory can be written as

$$E_b^i I_y^i \frac{\partial^4 w_b^i}{\partial x_i^4} - N_b^i \frac{\partial^2 w_b^i}{\partial x_i^2} = q_z^i - q_x^i \frac{\partial w_b^i}{\partial x_i} + \frac{\partial m_{by}^i}{\partial x_i} \qquad \text{in } L_i,\ \mathrm{i} = 1,2,...,I \tag{6}$$

$$a_{1i}^z w_b^i + a_{2i}^z R_z^i = a_{3i}^z \qquad \beta_{1i}^z \theta_y^i + \beta_{2i}^z M_y^i = \beta_{3i}^z \qquad \text{at the beam ends } x_i = 0,\ L_i \tag{7a,b}$$

where $w_b^i = w_b^i(x_i)$ is the transverse deflection of the i-th beam with respect to z_i axis; I_y^i is its moment of inertia with respect to y_i axis; $N_b^i = N_b^i(x_i)$ is the axial force at the x_i centroid axis; a_{ji}^z, β_{ji}^z $(j=1,2,3)$ are coefficients specified at the boundary of the i-th beam formulating all types of the conventional boundary conditions.

Similarly, the $v_b^i = v_b^i(x_i)$ transverse deflection with respect to y_i axis must satisfy the following boundary value problem

$$E_b^i I_z^i \frac{\partial^4 v_b^i}{\partial x_i^4} - N_b^i \frac{\partial^2 v_b^i}{\partial x_i^2} = q_y^i - q_x^i \frac{\partial v_b^i}{\partial x_i} - \frac{\partial m_{bz}^i}{\partial x_i} \qquad \text{in } L_i,\ \mathrm{i} = 1,2,...,I \tag{8}$$

$$a_{1i}^{y} v_b^i + a_{2i}^{y} R_y^i = a_{3i}^{y} \qquad \beta_{1i}^{y} \theta_z^i + \beta_{2i}^{y} M_z^i = \beta_{3i}^{y} \qquad \text{at the beam ends } x_i = 0,\ L_i \tag{9a,b}$$

where I_z^i is the moment of inertia of the i-th beam with respect to y_i axis; a_{ji}^{y}, β_{ji}^{y} $(j = 1,2,3)$ are coefficients specified at its boundary; θ_z^i, R_y^i, M_z^i are the slope, the reaction and the bending moment at the i-th beam ends, respectively.

Since linearized beam bending theory is considered the axial deformation u_b^i of the beam arising from the arbitrarily distributed axial force q_x^i ($i=1,2,...I$) is described by solving independently the boundary value problem

$$E_b^i A_b^i \frac{\partial^2 u_b^i}{\partial x_i^2} = -q_x^i \qquad \text{in } L_i,\ \mathrm{i} = 1,2,...,I \tag{10}$$

$$a_{1i}^{x} u_b^i + a_{2i}^{x} N_b^i = a_{3i}^{x} \qquad \text{at the beam ends } x = 0,\ L_i \tag{11}$$

where N_b^i is the axial reaction at the i-th beam ends given as

$$N_b^i = E_b^i A_b^i \frac{\partial u_b^i}{\partial x_i} \tag{12}$$

Finally, the nonuniform angle of twist with respect to $\tilde{x}_i$ shear center axis has to satisfy the following boundary value problem [2]

$$E_b^i I_w^i \frac{\partial^4 \theta_{\tilde{x}}^i}{\partial \tilde{x}_i^4} - G_b^i I_{\tilde{x}}^i \frac{\partial^2 \theta_{\tilde{x}}^i}{\partial \tilde{x}_i^2} = m_{b\tilde{x}}^i \qquad \text{in } L_i,\ \mathrm{i} = 1,2,...,I \tag{13}$$

$$a_{1i}^{\tilde{x}} \theta_{\tilde{x}}^i + a_{2i}^{\tilde{x}} M_{\tilde{x}}^i = a_{3i}^{\tilde{x}} \qquad \beta_{1i}^{\tilde{x}} \frac{\partial \theta_{\tilde{x}}^i}{\partial \tilde{x}_i} + \beta_{2i}^{\tilde{x}} M_w^i = \beta_{3i}^{\tilde{x}} \qquad \text{at the beam ends } x_i = 0,\ L_i \tag{14a,b}$$

where $\theta_{\tilde{x}}^i = \theta_{\tilde{x}}^i(\tilde{x}_i)$ is the variable angle of twist of the i-th beam along the $\tilde{x}_i$ shear center axis; $G_b^i = E_b^i / 2(1+\nu_b^i)$ is its shear modulus; I_w^i, $I_{\tilde{x}}^i$ are the warping and torsion constants of the i-th beam cross section, respectively; $a_{ji}^{\tilde{x}}$, $\beta_{ji}^{\tilde{x}}$ $(j = 1,2,3)$ are coefficients specified at the boundary of the i-th beam formulating the most general linear torsional boundary conditions for the beam problem including also the elastic support; $\frac{\partial \theta_{\tilde{x}}^i}{\partial \tilde{x}_i}$ denotes the rate of change of the angle of twist and it can be regarded as the torsional curvature; $M_{\tilde{x}}^i$ is the twisting moment and M_w^i is the warping moment due to the torsional curvature at the boundary of the i-th beam.

Eqns. (1), (4a), (4b), (6), (8), (10), (13) constitute a set of seven coupled partial differential equations including ten unknowns, namely w_p, u_p, v_p, w_b^i, v_b^i, u_b^i, $\theta_{\tilde{x}}^i$, q_x^i, q_y^i, q_z^i. Three additional equations are required, which result from the displacement continuity condition in the direction of z_i local axes and a linear relationship between interface slip and corresponding tractions in the directions of x_i and y_i local axes at the midline of each (i-th) plate – beam interface. These conditions can be expressed as

$$w_p - w_b^i = e_{S\tilde{y}}^i \theta_{\tilde{x}}^i \qquad \text{in the direction of } z_i \text{ local axis} \qquad (15)$$

$$u_p - u_b^i = \frac{h_p}{2}\frac{\partial w_p}{\partial x} - e_{Cz}^i \frac{\partial w_b^i}{\partial x_i} - e_{Cy}^i \frac{\partial v_b^i}{\partial x_i} + \left(\phi_S^P\right)_{f_i} \frac{\partial \theta_{\tilde{x}}^i}{\partial \tilde{x}_i} + \frac{q_x^i}{k_x^i}$$

$$\text{in the direction of } x_i \text{ local axis} \qquad (16)$$

$$v_p - v_b^i = -\frac{h_p}{2}\frac{\partial w_p}{\partial y} - e_{S\tilde{z}}^i \theta_{\tilde{x}}^i + \frac{q_y^i}{k_y^i} \qquad \text{in the direction of } y_i \text{ local axis} \qquad (17)$$

where $\left(\phi_S^P\right)_{f_i}$ is the value of the primary warping function with respect to the shear center S of the beam cross section at the midline of the f_i (i-th) interface [2] and k_x^i, k_y^i are the stiffnesses of the arbitrarily distributed shear connectors along x_i and y_i directions, respectively.

In all the aforementioned equations the values of all the eccentricities e_{Cz}^i, e_{Cy}^i, $e_{S\tilde{z}}^i$, $e_{S\tilde{y}}^i$ and of the primary warping function $\varphi_S^P(\tilde{y}_i, \tilde{z}_i)$ should be set having the appropriate algebraic sign corresponding to the local beam axes.

It is worth here noting that the coupling of the aforementioned equations is nonlinear due to the terms including the unknown q_x^i and q_y^i interface forces.

3. Numerical Solution

The numerical solution of the boundary value problems described by eqns (1-2a,b), (4a,b-5a,b), (6-7a,b), (8-9a,b), (10-11) and (13-14a,b) is accomplished employing the Analog Equation Method [3].

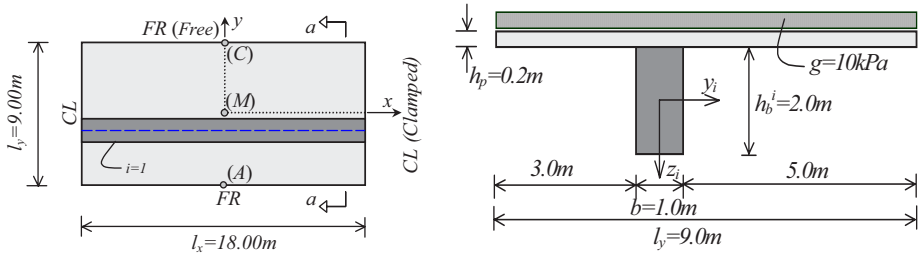

(a) Plan view (b) Section *a-a*

$$E = E_b^{i=1} = 3.00 \times 10^7\, kPa\,,\ \nu = \nu_b^{i=1} = 0.20$$

$$I_{\tilde{x}}^{i=1} = 4.5733\text{E-}01 m^4\,,\ I_w^{i=1} = 2.0326\text{E-}02 m^6$$

$$k_x^i = \lambda_x^i k_{con}^i\,,\ k_y^i = \lambda_y^i k_{con}^i\,,\ k_{con}^i = \left(750 - 200 h_b^i\right)|x|\,(kPa)$$

Fig.2. Plan view (a) and section a-a (b) of the stiffened plate.

4. Numerical examples

A rectangular plate with dimensions $a \times b = 18.0 \times 9.0\ m$ stiffened by a rectangular beam $1.0 \times 2.0\ m$ eccentrically placed with respect to the center line of the plate (Fig.2) has been studied. The plate is clamped along its small edges, while the other two edges are free according to both its transverse and inplane boundary conditions, while the beam is also clamped at its edges according to its transverse, axial and torsional boundary conditions. In Fig.3 the plate deflection w_p contour lines and its values at various points

of the fully or partially connected stiffened plate are presented as compared wherever possible with those obtained from a FEM solution employing shell finite elements, which ignore the warping of the cross section of the stiffening beam.

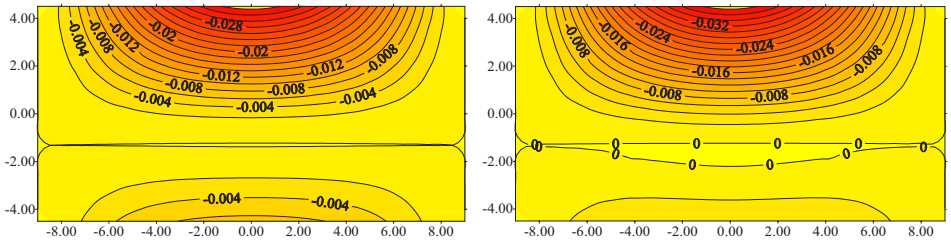

Present study AEM:
$w_p^A = 0.661cm$
$w_p^M = 0.259cm$
$w_p^C = 3.492cm$

Shell FE NASTRAN Code
$w_p^A = 0.825cm$
$w_p^M = 0.326cm$
$w_p^C = 3.585cm$

(a)

Present study AEM:
$w_p^A = 0.359cm$
$w_p^M = 0.396cm$
$w_p^C = 3.889cm$

(b)

Fig.3. Deflection $w_p(m)$ contour lines for fully ($\lambda_x^i = \lambda_y^i = 0$) (a) and partially ($\lambda_x^i = \lambda_y^i = 10$) (b) connected stiffened plate.

5. Concluding remarks

The main conclusions that can be drawn from this investigation are

a. The proposed model permits the study of a stiffened plate subjected to an arbitrary loading, while both the number and the placement of the nonintersecting stiffening beams are also arbitrary (eccentric beams are also included).
b. The proposed model permits the evaluation of both the longitudinal and the transverse inplane shear forces at the interfaces between the plate and the beams, the knowledge of which is very important in the design of prefabricated plate beams structures (estimation of shear connectors in both directions).
c. The nonuniform torsion in which the stiffening beams are subjected is taken into account by solving the corresponding problem and by comprehending the arising twisting and warping in the corresponding displacement continuity conditions.
d. The influence of the interface slip to the behavior of the stiffened plate is verified.

References

[1] E.J. Sapountzakis and J.T. Katsikadelis. Analysis of Plates Reinforced with Beams, *Computational Mechanics*, **26,** 66-74, (2000).

[2] E.J. Sapountzakis and V.G. Mokos,. Warping Shear Stresses in Nonuniform Torsion by BEM, *Computational Mechanics,* **30**(2), 131-142, (2003).

[3] J.T. Katsikadelis. The Analog Equation Method. A Boundary – only Integral Equation Method for Nonlinear Static and Dynamic Problems in General Bodies, *Theoretical and Applied Mechanics*, **27,** 13-38, (2002).

BEM and FEM Coupling in Elastostatics using a 3D Mortar Method

Luís Rodríguez-Tembleque[1], Ramón Abascal[2]

Escuela Superior de Ingenieros, Camino de los descubrimientos s/n, E41092 Sevilla, SPAIN

[1]luisroteso@us.es, [2]abascal@us.es

Keywords: Coupling, Mortar Method,Boundary Element Method, Finite Element Method.

Abstract. Conventional methods for coupling Boundary and Finite Elements Methods (BEM-FEM) have been based on the direct connection of the two solids through their common matching meshed interfaces using Lagrange multipliers. As each numerical method uses different variables, it is necessary to alter the formulation of one of the methods to make it compatible with the other. Lately, a formulation based on the localized Lagrange multipliers has established the connection of non-matching finite and boundary element meshes, increasing the number of the variables. The mortar method is another strategy to enforce constrains in the discretized systems with non matching meshes. In this work, a 3D mortar method is applied for 3D non-matching BEM-FEM and BEM-BEM meshes coupling. The formulation presented facilitates the connection of non-matching Finite and Boundary element meshes, using a more compact and reduced systems.

Introduction

Conventional methods for coupling BEM-FEM have been based on the direct connection node to node of the two solids through their common matching meshed. The Boundary Element Method uses the displacements and tractions as variables and the Finite Element Method uses the displacements and forces, so it's necessary to alter the formulation of one of the methods to make it compatible with the other. In this sense, the works of Zienkiewicz et al. [1] and Brebbia and Georgiou [2] formulate the problem using two different strategies. The first one consider the BE region as a FE region, and the second one tries to reformulate the FE region to make it compatible with the BE equations.

The number of contributions considering coupling between the FEM and the BEM when the meshes are non-matching is small. Recently, J. A. Gonzalez et al. [3] presented a a very nice coupling formulation based on the use of localized Lagrange multipliers, as and extension of the formulation proposed by Park and Felippa [4]. A discrete moving frame is interposed between the subdomains and connected to the BE or FE substructures by the localized Lagrange multipliers collocated at the interface nodes of each substructure. The implementation of their method provides a partitioned formulation and avoids the integration of the Lagrange multipliers fields but requires the solution of more variables: the two sets of multipliers and the frame displacements. The mortar method presented by Bernardi et al. [5] in domain decomposition and then revised by Wohlmuth [6], is another strategy to enforce constraints in the discretized systems with non-matching meshes. Recently Puso [7] has developed a version of the mortar method for dissimilar 3D meshes in large deformation solid mechanics, and Fisher and Gaul [8] have applied the mortar method in acoustical fluid-structure problems.

In this work a mortar method is applied to couple two substructures meshed with non-matching BE and FE meshes. The mortar method allows imposing the continuity condition at the interface. The advantage of this methodology is that avoid increasing the number of unknowns in the problem, providing the compact system of equations to solve. Also, the methodology can be applied to BEM-BEM coupling. The proposed methodology and their capabilities have been tested in a benchmark problem: a rectangular block under constant stress condition, using a BE-FE mesh.

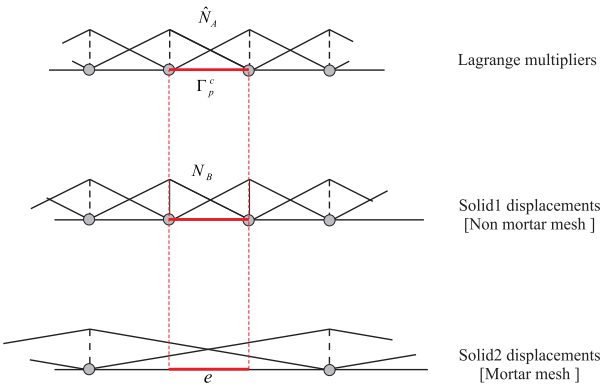

Figure 1: Shape functions for displacements and Lagrange multipliers tractions on each subdomain, in the coupling zone.

Weak Formulation

Lets consider a domain Ω divided in two coupled subdomains, Ω^1 and Ω^2. The virtual work over the tying surfaces enforces the coupling condition in a weak form, through the following expression:

$$\Pi^P = \int_{\Gamma_p} \{\lambda_j \ (u_j^1 - u_j^2)\} d\Gamma \tag{1}$$

where λ_j is the Lagrange Multipliers j-component traction field over the coupling surface, Γ_p, and u_j^1 and u_j^2 are the subdomains 1 and 2 displacements fields over the coupling surface. The variation of this form leads to:

$$\delta\Pi^P = \int_{\Gamma_p} \{\delta\lambda_j \ (u_j^1 - u_j^2)\} d\Gamma + \int_{\Gamma_p} \delta u_j^1 \ \lambda_j \ d\Gamma + \int_{\Gamma_p} \delta u_j^2 \ \lambda_j \ d\Gamma \tag{2}$$

The first term describes the fulfilment of the coupling condition, and the second and the third terms yields to the coupling tractions acting over each substructure.

Discretization

The traction λ_j and each solid displacement u_j^i ($i = 1, 2$) could be interpolated on the coupling surface Γ_p as follows,

$$\lambda_j = \sum_{A=1}^{m_e^1} \widehat{N}_A \lambda_{jA}, \ \ u_j^i = \sum_{B=1}^{n_e^i} N_B^i u_{jB}^i, \ \ (i = 1, 2) \tag{3}$$

The shape functions N_B^i are the standard bilinear shape functions and u_{jB}^i are the j-component nodal displacements numbered according for the e-element nodes on the mesh surfaces ($i = 1, 2$), n_e^i . The shape functions $\widehat{N}_A$ could be considered: bilinear or the dual basis functions introduced by Wohlmuth [9].

Piecewise linear interpolation. The Lagrange multipliers tractions are discretized using the non-mortar side displacements shape functions, like [5], so selecting the subdomain 1 as the non-mortar side, we have: $\widehat{N}_A = N_A^1$. The nodes at the boundaries of Γ_p would have to be constant fields over their elements, but this is only required to avoid the over constraint if an additional restriction is enforced.

The present formulation considers the fine mesh (the non-mortar mesh) is included on the coarse mesh, as Fig.(1) shows. Under this assumption, substituting the expressions in eq (3) in the coupling term in eq (2), it can be written as

$$\sum_{e=1}^{N_e}\sum_{c=1}^{N_c}\sum_{A=1}^{n_e^1}\sum_{B=1}^{n_e^1}\delta\lambda_{jA}\int_{\Gamma_p^c}\widehat{N}_A N_B^1\ d\Gamma\ u_{jB}^1 = \sum_{e=1}^{N_e}\sum_{c=1}^{N_c}\sum_{A=1}^{n_e^1}\sum_{B=1}^{n_e^2}\delta\lambda_{jA}\int_{\Gamma_p^c}\widehat{N}_A N_B^2\ d\Gamma\ u_{jB}^2 \tag{4}$$

where N_c and N_e are the number of elements on the non-mortar and mortar side, respectively, and Γ_p^c is the element c region. The eq (4), could be written in a matrix for as follows

$$\delta\lambda^T\ \mathbf{M}^1\ \mathbf{u}^1 = \delta\lambda^T\ \mathbf{M}^2\ \mathbf{u}^2 \tag{5}$$

being λ and $\mathbf{u}^i$ $(i=1,2)$ the nodal tractions vector and nodal displacements vectors of each mesh, and $\mathbf{M}^i$ $(i=1,2)$ the matrices obtained assembling the terms of eq (4).

Dual basis interpolation. Wohlmuth [9] introduced a dual formulation for $\widehat{N}_A$ that orthogonalizes the expressions on the left hand side in eq (4) so,

$$\int_{\Gamma_p}\widehat{N}_A N_B^1 d\Gamma = \delta_{AB}\int_{\Gamma_p} N_A^1 d\Gamma \tag{6}$$

The dual basis functions are a linear combination of the non-mortar side displacement shape functions,

$$\widehat{N}_A = \sum_{B=1}^{n_e^1}\alpha_{AB}N_B^1 \tag{7}$$

where the coeficients α_{AB} are computed for every element solving a linear sistem as a result of substituting eq (7) into eq (6) for all the elements nodes. The dual functions have been applied in 3D problems by Wohlmuth in problems with rectangular elements and by Puso [7] in arbitrari 3D problems, to have a $\mathbf{M}^1$ sparse matrix.

Boundary Element and Finite Element equations

The elastic equations for the subdomain Ω^1 using the BEM, could be written respectively, as:

$$\mathbf{H}^1\mathbf{u}^1 - \mathbf{G}^1\mathbf{p}^1 = \mathbf{b}^1 \tag{8}$$

where the vector $\mathbf{u}^1$ represents the nodal displacements, and $\mathbf{b}^1$ contains the applied boundary conditions. The eq (10) can be reorganized in the following way:

$$\mathbf{A}_q^1\mathbf{x}_q^1 + \mathbf{A}_u^1\mathbf{u}_p^1 - \mathbf{A}_p^1\mathbf{p}_p^1 = \mathbf{b}^1 \tag{9}$$

being $\mathbf{u}_p^1$ the nodal displacements on Γ_p, $\mathbf{p}_p^1$ is the nodal contact tractions, $\mathbf{x}_q^1$ is the unknown nodal displacements or tractions, and $\mathbf{A}_q^1$ is the columns of $\mathbf{H}^1$ and $\mathbf{G}^1$ matrices, depending on the boundary conditions.

The classical Finite Elements Method formulation [10], could be written using isoparametric elements, for the subdomain Ω^2 as

$$\mathbf{K}^2\ \mathbf{u}^2 = \mathbf{f}^2 \tag{10}$$

where $\mathbf{K}^2$ is the stiffness matrix, $\mathbf{u}^2$ is the nodal displacements vector, and $\mathbf{f}^2$ is the vector which groups the external forces. For the coupling problem, the equation above could be rearranged in the following way:

$$\mathbf{K}_q^2\ \mathbf{u}_q^2 + \mathbf{K}_p^2\ \mathbf{u}_p^2 - \mathbf{L}\ \mathbf{f}_p^2 = \mathbf{f}^2 \tag{11}$$

being $\mathbf{u}_q^2$ and $\mathbf{u}_p^2$ the nodal displacements out side and inside Γ_p respectively, and matrices $\mathbf{K}_q^2$ and $\mathbf{K}_p^2$, the columns of $\mathbf{K}^2$. The matrix $\mathbf{L}$ is a boolean matrix which assembles the forces on Γ_p , $\mathbf{f}_p^2$, into the global forces vector.

Relation between the Coupling Tractions λ, the BE Tractions $\mathbf{p}_p$ and the FE Forces $\mathbf{f}_p$

The equilibrium equation in the coupling zone, Γ_p, establishes the equality between the Lagrange multipliers tractions λ and the Boundary Element tractions $\mathbf{p}_p$ in the non-mortar size, only in case of piecewise linear interpolation of λ. In general cases, we have to establish the virtual work equivalence between the λ and $\mathbf{p}_p$, as follows:

$$\int_{\Gamma_p} (\delta \mathbf{u}^1)^T \ \mathbf{p}_p^1 \ d\Gamma = \int_{\Gamma_p} (\delta \mathbf{u}^1)^T \ \lambda \ d\Gamma \tag{12}$$

For the Finite Element forces in the coupling zone, we proceed in the same way:

$$(\delta \mathbf{u}^2)^T \ \mathbf{f}_p^2 = \int_{\Gamma_p} (\delta \mathbf{u}^2)^T \ \lambda \ d\Gamma \tag{13}$$

Developing the integrals, the virtual work expressions on the coupling zone, (12) and (13), could be expressed in a matrix form as,

$$(\delta \mathbf{u}^2)^T \{(\mathbf{m}^1)^T \mathbf{p}_p^1 - (\mathbf{M}^1)^T \ \lambda\} = \mathbf{0} \quad , \ (\delta \mathbf{u}^2)^T \{(\mathbf{M}^2)^T \ \lambda - \mathbf{f}_p^2\} = \mathbf{0} \tag{14}$$

where $\mathbf{m}^1$ is the assembled mass matrix.

Coupled BEM-FEM

The resulting coupled system is obtained using the boundary element equation and the finite element equation, presented in the equations (9) and (11), and the expressions (5) and (14). So the equations set is

$$\begin{bmatrix} \mathbf{A}_q^1 & \mathbf{A}_u^1 & \mathbf{0} & \mathbf{0} & -\mathbf{A}_p^1 & \mathbf{0} \\ \mathbf{0} & \mathbf{0} & \mathbf{K}_q^2 & \mathbf{K}_p^2 & \mathbf{0} & \mathbf{L}(\mathbf{M}^2)^T \\ \mathbf{0} & \mathbf{0} & \mathbf{0} & \mathbf{0} & (\mathbf{m}^1)^T & -(\mathbf{M}^1)^T \\ \mathbf{0} & -\mathbf{M}^1 & \mathbf{0} & \mathbf{M}^2 & \mathbf{0} & \mathbf{0} \end{bmatrix} \begin{bmatrix} \mathbf{x}_q^1 \\ \mathbf{u}_p^1 \\ \mathbf{u}_q^2 \\ \mathbf{u}_p^2 \\ \mathbf{p}_p^1 \\ \lambda \end{bmatrix} = \begin{bmatrix} \mathbf{b}^1 \\ \mathbf{f}^2 \\ \mathbf{0} \\ \mathbf{0} \end{bmatrix} \tag{15}$$

If we choose the Lagrange multipliers piecewise linear interpolation, the third row of eq (15) will establish the equality of the Lagrange multipliers and the Boundary subdomain 1 tractions. This fact allow to reduce the equations set, so the eq (15) can be rewritten in a more compact form as:

$$\begin{bmatrix} \mathbf{A}_q^1 & \mathbf{A}_u^1 & \mathbf{0} & \mathbf{0} & -\mathbf{A}_p^1 \\ \mathbf{0} & \mathbf{0} & \mathbf{K}_q^2 & \mathbf{K}_p^2 & \mathbf{L}(\mathbf{M}^2)^T \\ \mathbf{0} & -\mathbf{M}^1 & \mathbf{0} & \mathbf{M}^2 & \mathbf{0} \end{bmatrix} \begin{bmatrix} \mathbf{x}_q^1 \\ \mathbf{u}_p^1 \\ \mathbf{u}_q^2 \\ \mathbf{u}_p^2 \\ \mathbf{p}_p^1 \end{bmatrix} = \begin{bmatrix} \mathbf{b}^1 \\ \mathbf{f}^2 \\ \mathbf{0} \end{bmatrix} \tag{16}$$

So the number of variables doesn't increase with regard to the number of the solids variables.

Coupled BEM-BEM

Following the same philosophy as in the BEM-MEF coupling, and using the BE equations for the subdomain2, the BEM-BEM coupling equations set can be written as,

$$\begin{bmatrix} \mathbf{A}_q^1 & \mathbf{A}_u^1 & \mathbf{0} & \mathbf{0} & -\mathbf{A}_p^1 & \mathbf{0} & \mathbf{0} \\ \mathbf{0} & \mathbf{0} & \mathbf{A}_q^2 & \mathbf{A}_u^2 & \mathbf{0} & -\mathbf{A}_p^2 & \mathbf{0} \\ \mathbf{0} & \mathbf{0} & \mathbf{0} & \mathbf{0} & (\mathbf{m}^1)^T & \mathbf{0} & -(\mathbf{M}^1)^T \\ \mathbf{0} & \mathbf{0} & \mathbf{0} & \mathbf{0} & \mathbf{0} & (\mathbf{m}^2)^T & (\mathbf{M}^2)^T \\ \mathbf{0} & -\mathbf{M}^1 & \mathbf{0} & \mathbf{M}^2 & \mathbf{0} & \mathbf{0} & \mathbf{0} \end{bmatrix} \begin{bmatrix} \mathbf{x}_q^1 \\ \mathbf{u}_p^1 \\ \mathbf{x}_q^2 \\ \mathbf{u}_p^2 \\ \mathbf{p}_p^1 \\ \mathbf{p}_p^2 \\ \lambda \end{bmatrix} = \begin{bmatrix} \mathbf{b}^1 \\ \mathbf{b}^2 \\ \mathbf{0} \\ \mathbf{0} \\ \mathbf{0} \end{bmatrix} \tag{17}$$

where the first two rows are the BE each solid equation and the following two rows are the energetic equivalence between the BE tractions and the coupling tractions. Again choosing the Lagrange multipliers piecewise linear interpolation, the third row of eq (17) will establish the equality of the Lagrange multipliers and the Boundary subdomain 1 tractions. So the compact form of equation eq (17) will be:

$$\begin{bmatrix} \mathbf{A}_q^1 & \mathbf{A}_u^1 & \mathbf{0} & \mathbf{0} & -\mathbf{A}_p^1 & \mathbf{0} \\ \mathbf{0} & \mathbf{0} & \mathbf{A}_q^2 & \mathbf{A}_u^2 & \mathbf{0} & -\mathbf{A}_p^2 \\ \mathbf{0} & \mathbf{0} & \mathbf{0} & \mathbf{0} & (\mathbf{m}^2)^T & (\mathbf{M}^2)^T \\ \mathbf{0} & -\mathbf{M}^1 & \mathbf{0} & \mathbf{M}^2 & \mathbf{0} & \mathbf{0} \end{bmatrix} \begin{bmatrix} \mathbf{x}_q^1 \\ \mathbf{u}_p^1 \\ \mathbf{x}_q^2 \\ \mathbf{u}_p^2 \\ \mathbf{p}_p^1 \\ \mathbf{p}_p^2 \end{bmatrix} = \begin{bmatrix} \mathbf{b}^1 \\ \mathbf{b}^2 \\ \mathbf{0} \\ \mathbf{0} \end{bmatrix} \tag{18}$$

Examples

The proposed methodology has been tested in following examples:

1. Brick under unitary stress: The benchmark problem: a 2x2x4 mm rectangular block, with the material properties: $E = 10^4 MPa$ and $\nu = 0.3$, under unitary stress condition, have been solved successfully achieving the analytical solution. The figures (2a) and (2b) show the meshes and the results obtained in the BEM-FEM coupling. The fine mesh uses bilineal boundary elements, and the coarse mesh uses 8 nodes brick finite elements.

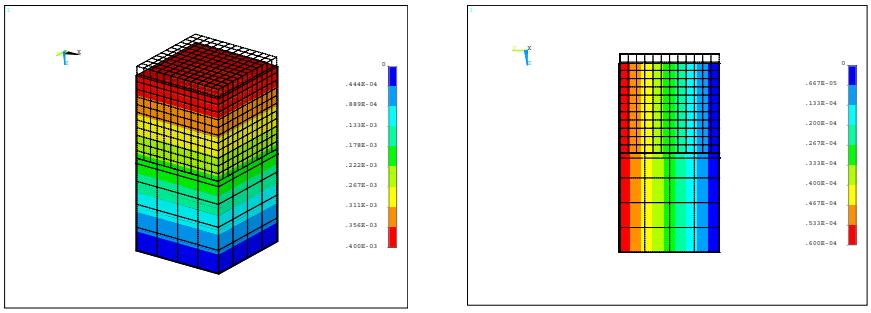

(a) (b)

Figure 2: Displacements fields: u_z (a), and u_y (b), under unitary stress condition using BE-FE non-matching meshes.

2. Two compressed rings: Two 20 mm radius rings are compressed imposing a vertical displacement on each one. Their material properties are the same, as in the previous example. These solids are modeled using the BEM with non-matching meshes, having the meshes in the coupling zone, 36 and 72 elements. The figures (3a) and (3b) show the displacements results obtained.

Conclusions

In this paper a methodology to couple two substructures meshed with non-matching BE and FE meshes based on a 3D mortar method has been proposed. One of the advantages of this methodology is that avoid to increase the number of unknowns in the problem, providing a compact system of equation to solve. Another one is that the methodology could be extensible to BEM-BEM coupling.

The proposed methodology and their capabilities have been tested successfully in a benchmark problem: a rectangular block under constant stress condition.

For the moment, the formulation has been applied with some restrictions on the meshes. So we continue working to solve more examples with more general non-matching meshes.

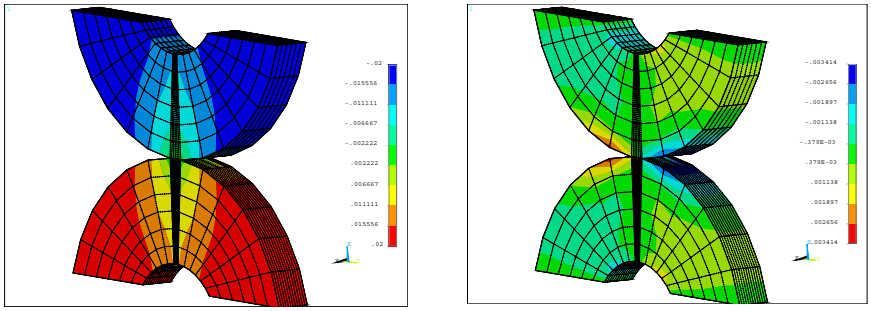

(a) (b)

Figure 3: Two compressed rings displacements fields details, u_z (a), and u_y (b), using BE-BE non-matching meshes.

Acknowledgments

This work was funded by the *Conserjería de Innovación Ciencia y Empresa de la Junta de Andalucía*, Spain, research project P05-TEP-00882, and by the *Ministerio de Educación y Ciencia*, Spain, research project DPI2006-04598.

References

[1] O.C. Zienkiewicz, D.W. Kelly and P. Bettes. The coupling of the finite element method and boundary solution procedures. *International Journal for Numerical Methods in Engineering*, **11**, 355–375 (1977).

[2] C.A. Brebbia and P. Georgiou. Combination of boundary and finite elements for elastostatics. *Aplied Mathematical Modelling*, **3**, 212–220 (1979).

[3] J.A. González, K.C. Park and C.A. Felippa. FEM and BEM coupling in elastostatics using localized Lagrange multipliers. *International Journal for Numerical Methods in Engineering*, Published Online: 31 Jul 2006.

[4] K.C. Park and C. A. Felippa. A variational framework for solution method developments in structural mechanics. *Journal of Applied Mechanics*, **65**, 242–249 (1998).

[5] C. Bernardi, Y. Maday and A. Patera. A new nonconforming approach to domain decomposition: the mortar element method. In H. Brezis and J.L. Lions, editors, *Nonlinear Partial Differential Equations and their Application*. Pitman, and Wiley: New York (1992); 13-51

[6] B.I. Wohlmuth. Discretization Methods and Iterative Solvers based on Domain Decomposition *Springer Verlag*, Berlin, Heidelberg, New York (2000).

[7] M.A. Puso. A 3D mortar method for solid mechanics. *International Journal for Numerical Methods in Engineering*, **59**, 315–336 (2004).

[8] M. Fisher and L. Gaul. Fast FEM-BEM mortar coupling for acoustic-structures interaction. *International Journal for Numerical Methods in Engineering*, **62**, 1677–1690 (2005).

[9] B.I. Wohlmuth. A mortar finite element method using dual spaces for the Lagrange multipliers. *SIAM, Journal of Numerical Analysis*, **38**, 989–1012 (2000).

[10] O. C. Zienkiewicz. and R. L. Taylor, The Finite Element Method (4th Edition). Mc Graw Hill, Vol. I (1989), Vol. II (1991).

AE signal characterization in fuel tanks through a LBIE/BEM and Time-Frequency analysis scheme

V. Vavourakis[1,3], V. I. C. Protopappas[2,4], D. I. Fotiadis[4,5], D. Polyzos[1,3]
[1] Department of Mechanical Engineering and Aeronautics, University of Patras, Patras, Greece
[2] Department of Medical Physics, Medical School, University of Ioannina, Ioannina, Greece
[3] Institute of Chemical Engineering and High Temperature Process ICE/HT-FORTH, Rio, Greece
[4] Unit of Medical Technology and Intelligent Information Systems, Department of Computer Science, University of Ioannina, Ioannina, Greece
[5] Biomedical Research Institute FORTH, Ioannina, Greece

Keywords: waveguides, dispersion curves, LBIE, BEM, Acoustic Emission, time-frequency analysis

Abstract. In the present paper a meshless Local Boundary Integral Equation (LBIE) method is properly combined with the Boundary Element Method (BEM) for the characterization of Acoustic Emission (AE) signals derived from nucleating cracks in the bottom of a fuel tank. The numerical determination of the dispersion curves associated with the guided waves propagating in the plate-like bottom of the tank is accomplished through the hydrid LBIE/BEM in conjunction with a Reassigned Smooth Pseudo Wigner-Ville (RSPWV) time-frequency analysis algorithm. Numerical results concerning the characterization of guided waves from nucleating surface-breaking and body cracks in the bottom of the fuel tank are presented. Useful conclusions for AE non-destructive testing are provided.

Introduction

According to the American Society for Testing and Materials [1], acoustic emissions are defined as "the class of phenomena whereby transient elastic waves are generated by the rapid release of energy from localized sources within the material". These waves generated after a loading of the structure, propagate through the medium and continually interact with the boundaries and the inhomogeneities of the structure. When they arrive at the material boundaries they can be detected by piezoelectric transducers. Inverting the information coming from the collected signals, the location and in some cases the type of the radiative defects can be assessed. It is immediately apparent that this NDT technique, known as Acoustic Emission (AE), detects rather the evolution of damage and not the level of damage itself as the conventional ultrasonic techniques do. Thus, the main problem associated with the AE technique is that it is very difficult to establish one correspondence between the type of the defect and the recorded signals.

In the present paper, it is shown that a numerical study on the propagation of guided waves generated by AE events can provide useful information about the type of damage. As it is indicated by the name, guided waves are disturbances propagating along the body of a structure. Since the interact continually with the boundaries of the structure, they propagate in different modes with various velocities, which depend on the frequency (dispersion). The typical numerical procedure for extracting dispersion curves for a waveguide is the use of either FEM or BEM for the determination of the time history of equally spaced points along the waveguide and then the application of the two-dimensional fast Fourier transform to convert the time-space results to frequency-wavelength domain [2,3]. An alternative and more promising approach is the use of time-frequency analysis instead of the frequency-wavelength representation [4]. Time-frequency analysis has previously been employed in studying velocity dispersion of Lamb waves in NDT applications of flaw detection and localization in aluminium and composite plates [4,5,6] as well as in the evaluation of bone fracture healing [7]. As opposed to traditional time domain and two-dimensional fast Fourier transform techniques which require the collection of multiple signals recorded at equally-spaced distances, time-frequency analysis can represent the dispersion of multiple wave modes using only a broadband signal.

The present work deals with the modal characterization of guided waves generated by AE events in the bottom of a fuel tank, which is modeled as a thin two-dimensional plate being in contact with the infintely extended storage petroleum. The initiation of AE signals is accomplishe by considering either surface-breaking or internal cracks and applying near to the tip of the crack burst tractions, as it is proposed by Arias and Achenbach [8]. The time history of the generated guided waves is taken through a hydrid numerical scheme, which combines effectively the meshless Local Boundary Integral Equation (LBIE), recently proposed by Sellountos and Polyzos [9,10] and a Boundary Element Method (BEM) suitable for solving acoustic problems [11]. The LBIE method is used for the numerical simulation of the created guided waves in the bottom of the tank, while the BEM is exploited for the simulation of the leaky waves radiated

through the liquid. More details on the meshless LBIE method and BEM one can find in references [12,13] and [14], respectively. For a given point in the bottom of the tank, the transformation of the obtained AE signals to the corresponding time-frequency diagrams is accomplished by means of the Reassigned Smooth Pseudo Wigner-Ville (RSPWV) algorithm illustrated in [7]. Finally, interesting conclusions are extracted and discussed in the framework of the AE non-destructive testing.

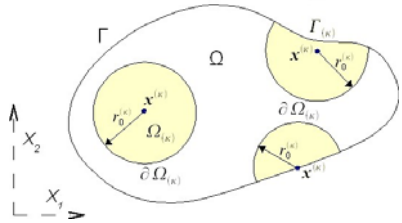

Figure 1. Support domains $\Omega_{(\kappa)}$ of internal and boundary nodes.

The meshless LBIE method in combination with the acoustic BEM.

Here, the hydrid LBIE/BEM scheme for solving a general, harmonic fluid-structure interaction problem is described in brief.

Consider an elastic body of volume Ω, bounded by a surface Γ and immersed in an infinitely extended fluid, characterized by a density ρ_a and an acoustic wave propagation speed c. The body and the boundary of the elastic material is covered by properly distributed points, as it is shown in Fig. 1. For harmonic problems without body forces, the displacement vector $\boldsymbol{u}$ at a point $\boldsymbol{x}^{(\kappa)} \in \Omega$ satisfies the well-known elastodynamic partial differential equation

$$\mu \nabla^2 \boldsymbol{u}(\boldsymbol{x}^{(\kappa)}) + (\lambda+\mu) \nabla \nabla \cdot \boldsymbol{u}(\boldsymbol{x}^{(\kappa)}) + \rho_e \omega^2 \boldsymbol{u}(\boldsymbol{x}^{(\kappa)}) = \boldsymbol{0} \quad , \tag{1}$$

where ∇ is the gradient operator, λ, μ are the Lamè constants, ρ_e is the elastic material density and ω stands for radial frequency.

Considering in eq. (1) the inertia term $\rho_e \omega^2 \boldsymbol{u}$ as a body force vector, the displacement vector at $\boldsymbol{x}^{(\kappa)}$ admits an integral representation of the form:

$$\begin{aligned} \tilde{\boldsymbol{\alpha}} \cdot \boldsymbol{u}(\boldsymbol{x}^{(\kappa)}, \omega) + \int_{\Gamma} \tilde{\boldsymbol{t}}^*(\boldsymbol{x}^{(\kappa)}, \boldsymbol{y}) \cdot \boldsymbol{u}(\boldsymbol{y}, \omega)\, dS_y = \\ \int_{\Gamma} \tilde{\boldsymbol{u}}^*(\boldsymbol{x}^{(\kappa)}, \boldsymbol{y}) \cdot \boldsymbol{t}(\boldsymbol{y}, \omega)\, dS_y + \rho_e \omega^2 \int_{\Omega} \tilde{\boldsymbol{u}}^*(\boldsymbol{x}^{(\kappa)}, \boldsymbol{y}) \cdot \boldsymbol{u}(\boldsymbol{y}, \omega)\, dV_y \end{aligned} \quad , \tag{2}$$

where $\tilde{\boldsymbol{u}}^*$, $\tilde{\boldsymbol{t}}^*$ are the static fundamental displacement and traction solutions [15], respectively, while $\tilde{\boldsymbol{\alpha}}$ represents the well-known jump tensor.

Since both kernels $\tilde{\boldsymbol{u}}^*$ and $\tilde{\boldsymbol{t}}^*$ become singular when the integration point $\boldsymbol{y}$ coincides with the source point $\boldsymbol{x}^{(\kappa)}$, eq. (2) can be written in a local form

$$\begin{aligned} \tilde{\boldsymbol{\alpha}} \cdot \boldsymbol{u}(\boldsymbol{x}^{(\kappa)}, \omega) + \int_{\partial\Omega_{(\kappa)} \cup \Gamma_{(\kappa)}} \tilde{\boldsymbol{t}}^*(\boldsymbol{x}^{(\kappa)}, \boldsymbol{y}) \cdot \boldsymbol{u}(\boldsymbol{y}, \omega)\, dS_y = \\ \int_{\partial\Omega_{(\kappa)} \cup \Gamma_{(\kappa)}} \tilde{\boldsymbol{u}}^*(\boldsymbol{x}^{(\kappa)}, \boldsymbol{y}) \cdot \boldsymbol{t}(\boldsymbol{y}, \omega)\, dS_y + \rho_e \omega^2 \int_{\Omega_{(\kappa)}} \tilde{\boldsymbol{u}}^*(\boldsymbol{x}^{(\kappa)}, \boldsymbol{y}) \cdot \boldsymbol{u}(\boldsymbol{y}, \omega)\, dV_y \end{aligned} \quad , \tag{3}$$

where $\partial\Omega_{(\kappa)}$ is the boundary of an arbitrary small circle $\Omega_{(\kappa)}$ called the support domain of point $\boldsymbol{x}^{(\kappa)}$ (see Fig. 1). The intersection of the circular local domain with the global boundary is denoted as: $\Gamma = \partial\Omega_{(\kappa)} \cap \Gamma$.

As reported in [9,13], the integrals defined on the local boundaries $\partial\Omega_{(\kappa)}$ comprising the unknown traction vectors $\boldsymbol{t}$ can be eliminated with the aid of a companion solution. Thus, eq. (3) takes the simpler form

$$\begin{aligned} \tilde{\boldsymbol{\alpha}} \cdot \boldsymbol{u}(\boldsymbol{x}^{(\kappa)}, \omega) + \int_{\partial\Omega_{(\kappa)} \cup \Gamma_{(\kappa)}} \tilde{\boldsymbol{t}}^{**}(\boldsymbol{x}^{(\kappa)}, \boldsymbol{y}) \cdot \boldsymbol{u}(\boldsymbol{y}, \omega)\, dS_y = \\ \int_{\Gamma_{(\kappa)}} \tilde{\boldsymbol{u}}^{**}(\boldsymbol{x}^{(\kappa)}, \boldsymbol{y}) \cdot \boldsymbol{t}(\boldsymbol{y}, \omega)\, dS_y + \rho_e \omega^2 \int_{\Omega_{(\kappa)}} \tilde{\boldsymbol{u}}^{**}(\boldsymbol{x}^{(\kappa)}, \boldsymbol{y}) \cdot \boldsymbol{u}(\boldsymbol{y}, \omega)\, dV_y \end{aligned} \quad , \tag{4}$$

where $\tilde{\boldsymbol{u}}^{**}$ and $\tilde{\boldsymbol{t}}^{**}$ are the new kernels defined by as the difference between the fundamental tensors $\tilde{\boldsymbol{u}}^*$, $\tilde{\boldsymbol{t}}^*$ and the corresponding companion solutions [15].

The interpolation of both displacements and tractions is accomplished by means of the Moving Least Squares (MLS) approximation scheme [9]. Thus, tractions defined on the global boundary of the body are

represented directly without the requirement of evaluating the derivatives of the MLS shape functions used for the approximation of displacements. Inserting the approximated vector fields into eq. (4) and collocating at all the considered points, one concludes to a system of linear algebraic equations having the form:

$$\tilde{\boldsymbol{H}}^{(e)} \cdot \check{\boldsymbol{u}} = \tilde{\boldsymbol{G}}^{(e)} \cdot \check{\boldsymbol{t}} \quad , \tag{5}$$

where the vector $\check{\boldsymbol{u}}$ comprises comprises all the components of the fictitious displacement vectors corresponding to N internal and L boundary nodes, while the vector $\check{\boldsymbol{t}}$ consists of the L fictitious boundary traction vectors. Matrices $\tilde{\boldsymbol{H}}^{(e)}$ and $\tilde{\boldsymbol{G}}^{(e)}$ come from the integration of the integrals containing the kernels $\tilde{\boldsymbol{u}}^{**}$ and $\tilde{\boldsymbol{t}}^{**}$, respectively. More details can be found in [9].

The problem in meshless techniques that use the MLS approximation scheme for the interpolation of the unknown parameters is the lack of Kronecker delta property [12]. Hence, no essential boundary conditions can be applied in a straightforward manner. However, as it is mentioned in [9], uniform distribution of nodes leads to MLS interpolating shape functions with delta property. Thus, considering uniform distribution of nodes the system (5) obtains the form:

$$\tilde{\boldsymbol{H}}_{\Omega}^{(e)} \cdot \check{\boldsymbol{v}} + \tilde{\boldsymbol{H}}_{\Gamma}^{(e)} \cdot \check{\boldsymbol{u}} = \tilde{\boldsymbol{G}}^{(e)} \cdot \check{\boldsymbol{t}} \quad , \tag{6}$$

where $\check{\boldsymbol{v}}$ and $\check{\boldsymbol{u}}$ represent the displacements at the interior and boundary nodes, respectively.

On the other hand, in immersed structures the guided waves can travel within the waveguide but also in the surrounding fluid as outgoing leaky acoustic waves. Considering the boundary Γ of the structure the source of the radiative acoustic energy, it is well known that the pressure field throughout the liquid admits the integral representation of the form [11,19]

$$\frac{1}{2}\, p(\boldsymbol{x}^{(\kappa)}, \omega) + \int_{\Gamma} \frac{\partial\, p^{*}(\boldsymbol{x}^{(\kappa)}, \boldsymbol{y})}{\partial \hat{n}_{y}}\, p(\boldsymbol{y}, \omega)\, dS_{y} = \int_{\Gamma} p^{*}(\boldsymbol{x}^{(\kappa)}, \boldsymbol{y})\, q(\boldsymbol{y}, \omega)\, dS_{y} \quad , \tag{7}$$

where p is the acoustic pressure, q is the normal component of the particle velocity, p^{*} is the free-space Green's function, $\boldsymbol{x}^{(\kappa)}$, $\boldsymbol{y}$ are position vectors on Γ indicating source and field points, respectively, and $\hat{\boldsymbol{n}}_{y}$ is the normal outward unit vector to the global boundary at $\boldsymbol{y}$.

Discretizing the boundary Γ with quadratic line elements and collocating eq. (7) at all boundary nodes, one obtains a final system of algebraic equations, i.e.

$$\tilde{\boldsymbol{H}}^{(a)} \cdot \check{\boldsymbol{p}} = \tilde{\boldsymbol{G}}^{(a)} \cdot \check{\boldsymbol{q}} \quad , \tag{8}$$

where vector $\check{\boldsymbol{p}}$ comprises the pressure fields of all boundary nodes, while vector $\check{\boldsymbol{q}}$ contains the normal components of the particle velocities of the same boundary nodes. Matrices $\tilde{\boldsymbol{H}}^{(a)}$ and $\tilde{\boldsymbol{G}}^{(a)}$ come from the integration of the integrals containing the kernels p^{*} and $\partial\, p^{*} / \partial \hat{n}$, respectively.

Taking into account that the nodes of the boundary element discretization are identical to the points being distributed on the surface of the waveguide by the LBIE method the assembly of eq. (6) and (8) is accomplished via the continuity conditions that connect the surface displacements $\boldsymbol{u}$ and tractions $\boldsymbol{t}$ of the elastic medium with the corresponding surface pressure p and normal pressure gradient q scalar fields, i.e.

$$\hat{\boldsymbol{n}}_{e}(\boldsymbol{x}^{(\kappa)}) \cdot \boldsymbol{u}(\boldsymbol{x}^{(\kappa)}, \omega) = -\frac{1}{\rho_{a}\omega^{2}}\, q(\boldsymbol{x}^{(\kappa)}, \omega) \quad , \quad \hat{\boldsymbol{n}}_{e}(\boldsymbol{x}^{(\kappa)}) \cdot \boldsymbol{t}(\boldsymbol{x}^{(\kappa)}, \omega) = p(\boldsymbol{x}^{(\kappa)}, \omega) \quad , \tag{9}$$

where $\hat{\boldsymbol{n}}_{e}$ is the normal outward unit vector to the interface surface of the elastic region.

Characterization of AE signals

Consider a *6mm* thick steel plate as the bottom of a fuel tank, with Young modulus, Poisson ratio and mass density being *E=200GPa*, *ν=0.29* and ρ_{e}*=7850Kg/m*^{3}, respectively. The lower surface of the plate is traction-free, while the upper one is in contact with petroleum, characterized by a pressure-wave velocity c_{p}*=1750m/s* and a mass density ρ_{a}*=881Kg/m*^{3}. Two different crack-like defects are located in the middle of the plate, as shown in Fig. 2. The depth of the vertical notch is *2mm* and the opening *3mm*. Similarly, for the internal, horizontal elliptical defect the two hemiaxes are assumed equal to 1mm and *1.5mm*. As reported in [8], the evolution of crack can be modelled by applying a sudden traction load on both surfaces of the defect as it is demonstrated in Fig. 2. In both cases the defects are subjected to impulse traction of *1MPa* with duration of *204.6μs*. The transient response at point A (see Fig. 2) of the plate is calculated via the hybrid LBIE/BEM scheme explained in the previous section. More precisely, the time-varied boundary conditions are converted to the frequency domain by means of the Fast Fourier Transform (FFT), considering N_{t}*=1024*

time steps.

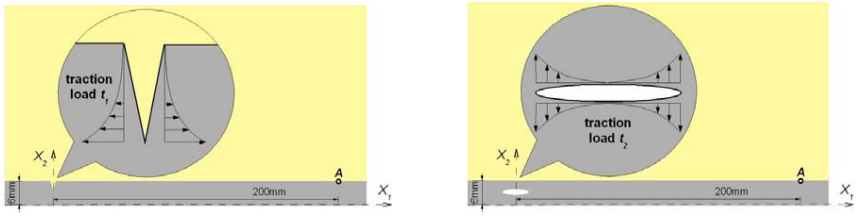

(a) (b)

Figure 2. A two dimensional steel plate being in contact with petroleum and having (a) a surface breaking crack and (b) an elliptical crack inclusion. AE signals are generated by applying burst tractions at the tip of the defects.

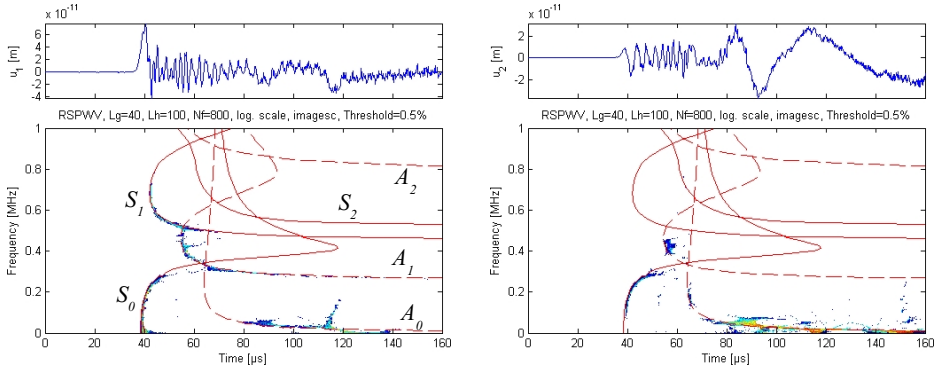

(a) (b)

Figure 3. Time-frequency representation and time response of the (a) u_1 and (b) u_2 displacement component at point A of the traction-free plate with a vertical notch, which interacts with the infinite layer of oil.

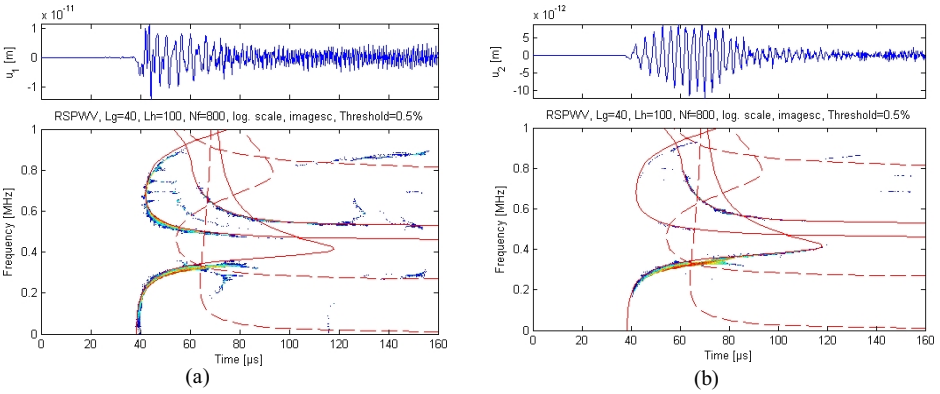

(a) (b)

Figure 4. Time-frequency representation and time response of the (a) u_1 and (b) u_2 displacement component at point A of the traction-free plate with a horizontal crack inclusion, which interacts with the infinite layer of oil.

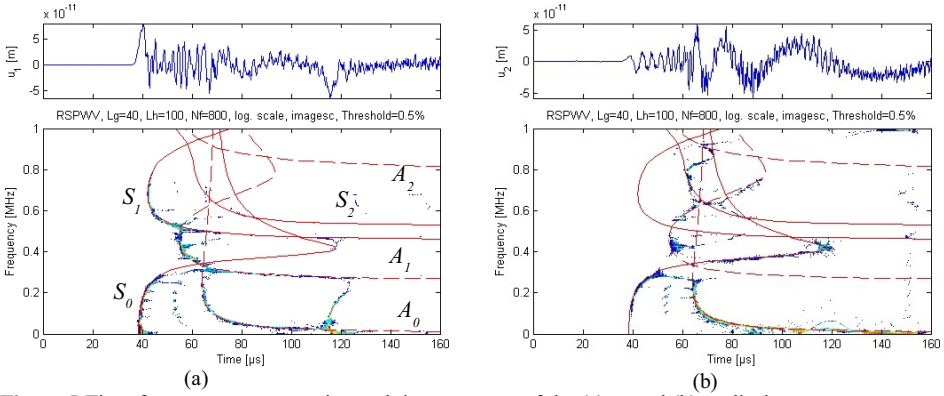

Figure 5 Time-frequency representation and time response of the (a) u_1 and (b) u_2 displacement component at point A of the traction-free plate with a vertical notch.

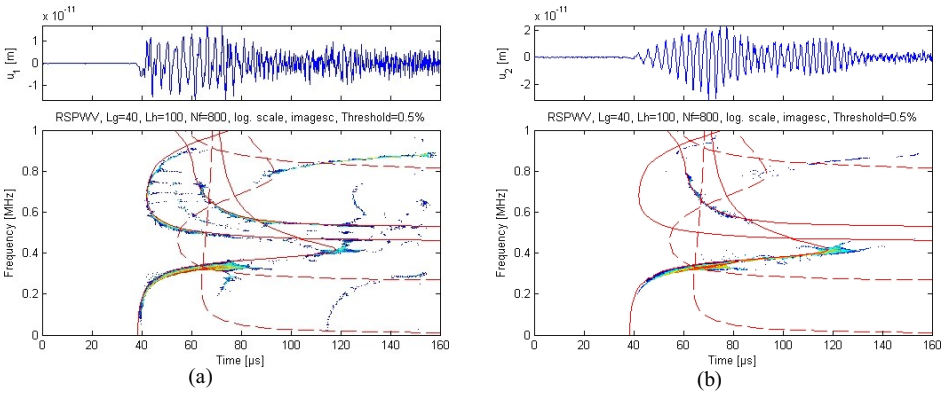

Figure 6. Time-frequency representation and time response of the (a) u_1 and (b) u_2 displacement component at point A of the traction-free plate with a horizontal crack inclusion.

The plate is covered by a uniform distribution of points, whose Euclidean distance is approximately equal to $\delta=0.3mm$. The support domain radius, used in the LBIE formulation, is $r_0^{(\kappa)}=2.1\times\delta$ the same for all nodes of the mesh, while quadratic polynomial basis is utilized for the MLS approximation scheme. All the harmonic problems (corresponding to each frequency) are solved numerically by the aforementioned LBIE/BEM algorithm. Finally, applying the inverse FFT on the above obtained frequency domain results, the time dependent signals at point A are taken.

On the numerically simulated AE signals, the Reassigned Smoothed Pseudo Wigner-Ville (RSPWV) analysis is applied in the way explained in [7]. The time-frequency diagrams for the signals captured at point A of the plate are presented in Fig. 3 for the vertical notch and in Fig. 4 for the elliptical crack-like defect. Comparisons are made with the theoretical time-frequency dispersion curves valid for a traction-free plate [7]. With the capital letters A_n and S_n indicating the antisymmetric and symmetric wave modes of the plate, respectively.

In order to have a clearer picture on the effect of the petroleum on the propagation of the guided AE signals, the time-frequency diagrams of the steel plate of Fig. 2, without the presence of the liquid, are evaluated and depicted in Figs. 5, 6 for the vertical and horizontal defects, respectively.

Comparing Figs. 3-6, the following interesting remarks related to AE signal characterization can be outlined:

- The dominant modes on the wave propagation problem of the traction-free plate, where a vertical notch defect is present, are the S_0 and A_0 ones, whereas the S_1 and A_1 wave modes are less dominant.

- The dominant modes on the wave propagation problem of the traction-free plate, where a horizontal crack-like defect is present, are the S_0 and A_1 ones, whereas the S_1 and S_2 wave modes are less dominant.
- On the case of the fluid-structure interaction problem, compared with the corresponding traction-free plate problem, the wave modes degrade in energy since a part of the propagating elastic waves diffracts to the acoustic medium.
- In both fluid-structure interaction problems, it seems that the S_0 wave mode is absent in the narrow frequency band of 400 to 500KHz, compared with the corresponding results obtained by the traction-free plate problems' analysis.

Conclusions

The LBIE method is properly combined with the BEM for the characterization of Acoustic Emission (AE) signals derived from nucleating surface-breaking and body cracks in plate-like waveguides being in contact with a fluid. Two different defects, i.e. a vertical surface breaking crack and a horizontal crack-like defect were considered. The obtained results reveal that the guided waves excited by the two defects appear significant differences as they compared to each other. Thus, Lamb mode dispersion can be very helpful in quantifying the AE inspection process.

Acknowledgements

This work is part-funded by the Greek Secretariat of Research and Technology and ENVIROCOUSTICS SA (PENED-2001 research program: NDT of fuel tanks and pressure vessels).

References

[1] American Society for Testing and Materials *ASTM E610-82: Standard definitions of terms relating to acoustic emission*, **2**, 373 (1987).
[2] D. Alleyne and P. Cawley *A two-dimensional Fourier transform method for the measurement of propagating multimode signals*, Journal of the Acoustical Society of America, **89**, 1159-1168 (1991).
[3] V. Vavourakis and D. Polyzos *A BEM/2D-FFT numerical technique for solving wave propagation problems in damaged plates*, ICCES'03 Conference, Corfu, Greece (2003).
[4] M. Niethammer, L.J. Jacobs, J. Qu and J. Jarzynski *Time-frequency representations of Lamb waves*, Journal of the Acoustical Society of America, **109**, 1841-1847 (2001).
[5] W.H. Prosser, M.D. Seale and B.T. Smith *Time-frequency analysis of the dispersion of Lamb modes*, Journal of the Acoustical Society of America, **105**, 2669-2676 (1999).
[6] R. Latif, H. Aassif, A. Moudden, B. Faiz and G. Maze *The experimental signal of a multilayer structure analysis by the time-frequency and spectral methods*, NDT & E International, 39, 349-355 (2006).
[7] V.C. Protopappas, D.I. Fotiadis and K.N. Malizos *Guided ultrasound wave propagation in intact and healing long bones*, Ultrasound in Medicine and Biology, **32**, 693-708 (2006).
[8] I. Arias and J.D. Achenbach *Use of reciprocity considerations for the two-dimensional BEM analysis of wave propagation in an elastic half-space with applications to acoustic emission*, Wave Motion, **39**, 281-294 (2004).
[9] E.J. Sellountos and D. Polyzos *A MLPG(LBIE) method for solving frequency domain elastic problems*, Computer Modeling in Engineering & Sciences, **4**, 619-636 (2003).
[10] E.J. Sellountos and D. Polyzos *A MLPG(LBIE) approach in combination with BEM*, Computer Methods in Applied Mechanics and Engineering, **194**, 859-875 (2005).
[11] J.P. Agnatiaris and D. Polyzos *A boundary element method for acoustc scattering from non-axisymmetric and axisymmetric elastic shells*, Computer Modeling in Engineering & Sciences, **4**, 197-212 (2003).
[12] S.N. Atluri *The meshless method (MLPG) for domain and BIE discretizations*, Tech Science Press, Forsyth (2004).
[13] S.N. Atluri, J. Sladek, V. Sladek and T. Zhu The local boundary integral equation (LBIE) and its meshless implementation for linear elasticity, Computational Mechanics, **25**, 180-198 (2000).
[14] O. Von Estorff *Boundary Elements in Acoustics, Advances & Applications*, WIT Press, Southampton, Boston (2000).
[15] D. Polyzos, S.V. Tsinopoulos and D.E. Beskos *Static and dynamic boundary element analysis in incompressible linear elasticity*, European Journal of Mechanics, A/Solids, **17**, 515-536 (1998).

An Optimum Drilling Pattern for Oil Reservoir

M. N. Mohamad Ibrahim[1] and S. Shuib[2]

[1]School of Chemical Sciences, Universiti Sains Malaysia,
11800 Pulau Pinang, Malaysia, mnm@usm.my

[2]School of Mechanical Engineering, USM Engineering Campus, Universiti Sains Malaysia,
14300 Nibong Tebal, Pulau Pinang, Malaysia

Keywords: boundary element method; oil reservoir; optimum drilling pattern

Abstract. This paper presents a quick and easy method to determine the best drilling pattern that should be used to develop a brand new oil reservoir. A Boundary Element approach for predicting the productivity of oil wells arranged in complex configurations within irregularly shaped reservoirs were developed. The integral equations are written for boundary points as well as for the locations of the wells which are treated as point sources and sinks with specified pressures but unknown strengths. Using this approach, the solution to the resulting matrix gives the values of the nodal boundary pressure and their normal derivatives, as well as the unknown flow rates of all the wells. Applications to regular four-spot, five-spot, seven-spot and nine-spot drilling patterns in order to determine which pattern produces the most oil for a given field are presented. Results show that the five-spot and the nine-spot patterns give the highest production rates for any number of wells for a square shaped oil reservoir.

Introduction

A simple but elegant and fast method to calculate complex well productivities located arbitrarily in irregularly shaped reservoir without resorting to finite difference simulators have been formulated [1,2]. The formulation is based on the Boundary Element Method (BEM) but with the modification that the integral equations are written for boundary points as well as for the locations of the point sources and/or sinks (producer and/or injector wells). A solution of the resulting equation gives the value of flow rate q for each of the well directly as well as the unknown boundary values of pressure p and pressure gradient dp/dn.

This paper takes the advantage of the formulation by applying it into square shaped reservoir with four commonly chosen drilling patterns *i.e.* four-spot, five-spot, direct line drive and staggered line drive. The formulation was coded into a computer program namely FORTRAN which allows a rapid analysis process. The main purpose of this study is simply to determine the optimum drilling pattern for the reservoir.

BEM Formulation

Differential equation describing the pressure distribution at all points in an oil reservoir is [1,2,3,4]:

$$\frac{\partial^2 p}{\partial X^2}+\frac{\partial^2 p}{\partial Y^2}+\frac{\mu}{k}\sum_{m=1}^{NSS} q_m\,\delta(X-X_m, Y-Y_m)=0 \qquad \text{.....eq (1}$$

where p is pressure, μ is the dynamic viscosity of the fluid, k is the permeability, q_m is the flow rate of the mth well per unit area (positive for injectors and negative for producers), δ is the Dirac delta function, X, Y are coordinates axes, and X_m , Y_m are coordinates of the mth source and/or sink where m varies from 1 to NSS.

Eq (1) can be transformed into an integral equation by multiplying it with the free-space Green's function and integrating it twice by parts. The free-space Green's function, also called the fundamental solution [5] is given as:

$$G = \frac{1}{2\pi} \ln\left(\frac{1}{r}\right) \qquad \text{.....eq (2}$$

where r is the distance between a field point (X, Y) and a point of application of a unit charge (X_C, Y_C). After standard manipulation [3], Eq (1) then becomes:

$$\alpha p\,(X_i, Y_i) = \frac{1}{2\pi} \sum_{j=1}^{N} \frac{\partial p}{\partial n_j} \int_{sj} \ln\left(\frac{1}{r_{i,j}}\right) ds -$$

$$\frac{1}{2\pi} \sum_{j=1}^{N} p_j \int_{sj} \frac{\partial}{\partial n}\left[\ln\left(\frac{1}{r_{i,j}}\right)\right] ds + \frac{1}{2\pi} \frac{\mu}{k} \sum_{m=1}^{NSS} q_m \ln\left(\frac{1}{r_{i,m}}\right) \qquad \text{.....eq (3}$$

where the boundary of the reservoir is divided into N constant elements with constant properties. α is the included angle at the ith pivot point. It is assigned a value of ½ when the pivot point is on a smooth boundary (*i.e.* not on a corner), and a value of 1 when the pivot point is inside the problem domain. The integral equations are written for boundary points as well as for the locations of the point sources and/or sinks (producer and/or injector wells). A solution of the resulting equation gives the value of flow rate, q, for each of the well directly as well as the unknown boundary values of pressure p and pressure gradient dp/dn. The formulation was coded into a computer program namely FORTRAN which allows a rapid analysis process.

Applications

Having developed the tool for calculating well flow rates, it was used to study the effect of changing the well spacing within various drilling patterns and observing the effect on the production rates of the wells in the pattern. This has direct application to the study of in-fill drilling. Consider a square, homogeneous, undersaturated and steady-state reservoir having the following properties:

L = 4,000 feet (reservoir length and width), μ = 1.0 cp, k = 100 md, φ = 0.15,
p_e = 2000 psi, h = 35 feet, ρ = 62.4 lb/ft^3, p_w = 100 psi and r_w = 0.25 feet

In each case, the reservoir is developed first with a single pattern covering the entire area. Then more wells are added to give an increasing number of patterns by reducing the pattern area or well spacing. The four drilling patterns chosen are regular four-spot, five-spot, seven-spot and nine-spot. All wells in this analysis are producers. Figures 1, 2, 3 and 4 show the well arrangements for the fully developed regular four-spot, five-spot, seven-spot and nine-spot drilling patterns respectively. A is the center point of the reservoir while B, C, D, E, F and G refer to the first, second, third, fourth, fifth and sixth stages of well

development respectively. *A* is also represent a well. Notice that Figure 2 (five-spot) has exactly the same number of wells and well locations with Figure 4 (nine-spot). Therefore, we might expect similar results for these two patterns.

A plot of the total production rate from the reservoir Q_n divided by the flow rate of the single well reservoir case Q_1 as a function of number of wells for all four drilling pattern is shown in Figure 5. The curve for a nine-spot pattern falls exactly on the five-spot curve as expected. The slope of all curves decrease as the number of wells increase and eventually approach a straight line as a consequence of the steady-state assumption. A plot of average production per well Q_{avg} as a function of number of well is shown in Figure 6. As expected, the average production per well drops as the number of wells increases (inversely proportional to the well spacing). However, the five-spot and the nine-spot have the highest Q_{avg} value for any number of wells present in the reservoir, followed by the four-spot and the seven-spot patterns. This is consistent with Figure 5. Notice also in both Figure 5 and Figure 6, initially the plots for 4-spot and seven-spot fall on the same curve until the number of wells is approximately 15 due to the arrangement of the wells for both patterns are the same. Beyond this limit, the arrangement of the wells in both patterns is no longer the same.

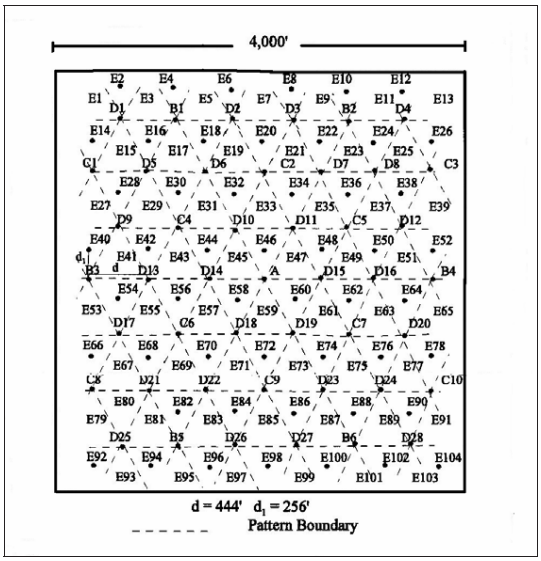

Fig. 1: Multiple four-spot pattern: 149 producing wells

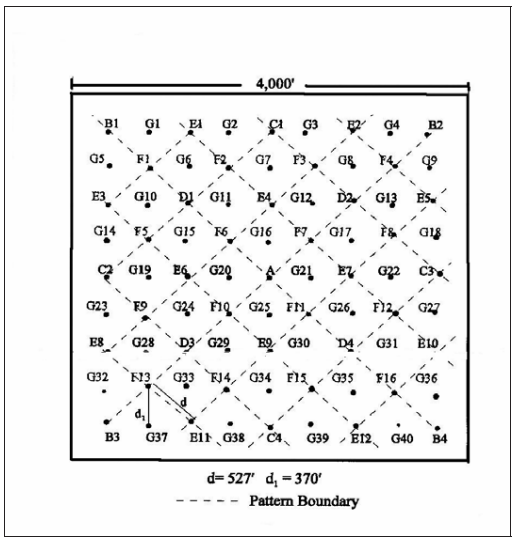

Fig. 2: Multiple five-spot pattern: 81 producing wells

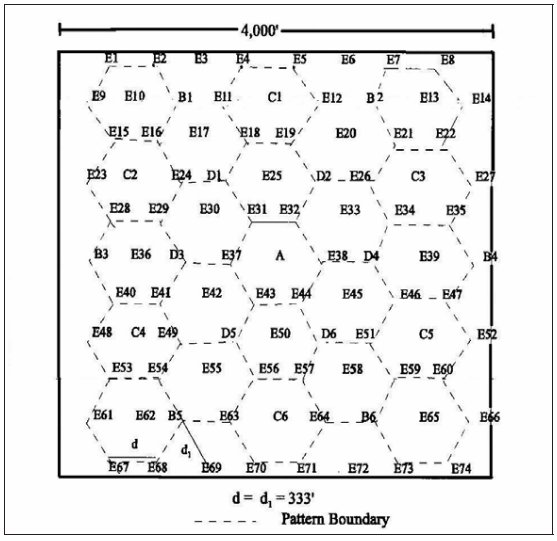

Fig. 3: Multiple seven-spot pattern: 93 producing wells

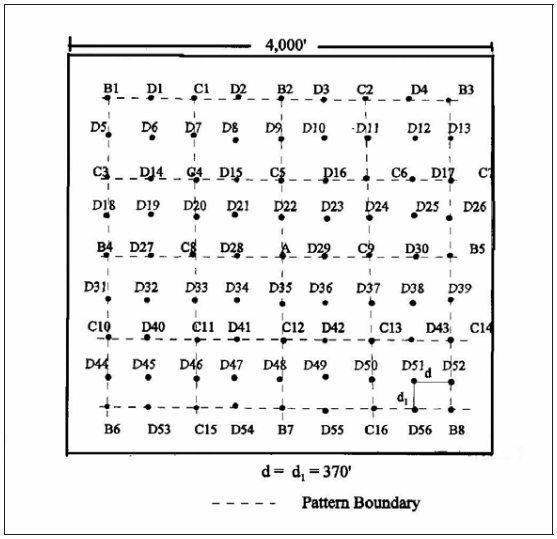

Fig. 4: Multiple nine-spot pattern: 81 producing wells

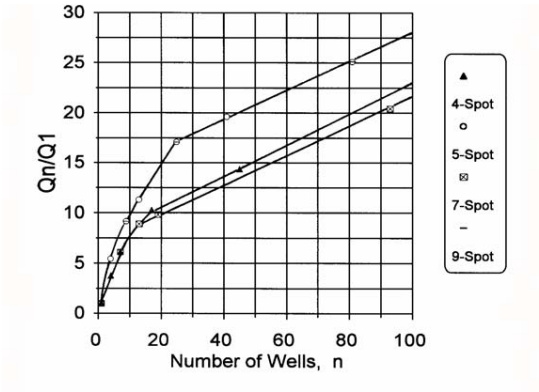

Fig. 5: Q_n/Q_1 as a function of number of wells present in the reservoir

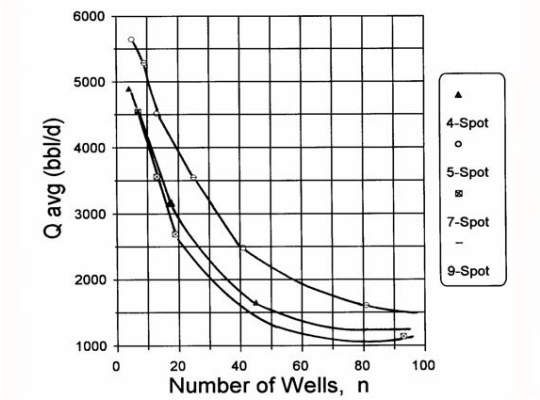

Fig. 6: Q_{avg} as a function of number of wells present in the reservoir

Acknowledgement

The first author would like to thank his beloved parents, Mrs. Saniah Abd Hamid and Mr. Mohamad Ibrahim Seeni Mohamad for their supports, sacrifices and patience throughout this project.

References

[1] M.N. Mohamad Ibrahim and D.T. Numbere *Boundary Element Analysis of the Productivity of Complex Petroleum Well Configurations*, In C.S. Chen, C.A. Brebbia and D. Pepper (Eds), *Boundary Element Technology XIII*, WIT Press. Southampton, 25-34 (1999).

[2] M.N. Mohamad Ibrahim and D.T. Numbere *Productivity Predictions for Oil Well Clusters Using a Boundary Element Method*, *J. of Physical Science*, Vol.11, 148-157 (2000).

[3] D.T. Numbere and D. Tiab *An Improved Streamline-Generating Technique That Uses the Boundary (Integral) Element Method*, *SPE Reservoir Engineering*, Vol. 3(3), 1061-68 (1988).

[4] M.N. Mohamad Ibrahim and D.T. Numbere *Boundary Shape Effects on the Productivity of Oil Well Clusters*, In *Boundary Element Technology XIV*, A. Kassab and C. A. Brebbia (Eds), WIT Press, Southampton, 293-299 (2001).

[5] C.A. Brebbia *The Boundary Element Method for Engineers*, John Wiley and Sons Inc., New York City, 46-103 (1978).

Multidomain Boundary Element Model for Cracks in Magneto-Electro-Elastic Materials

G. Davì, A. Milazzo and C. Orlando

Dipartimento di Tecnologie e Infrastrutture Aeronautiche, Università di Palermo
Viale delle Scienze, 90128 Palermo – Italy e-mail: davi@unipa.it

Keywords: Magneto-electro-elastic materials, Multidomain boundary element method, Fracture Mechanics

Abstract. A boundary element approach and its numerical implementation for the analysis of magneto-electro-elastic materials are presented with the aim to exploit their features in linear magneto-electro-elastic fracture mechanics. The problem is formulated employing generalized displacements, that is displacements and electric and magnetic scalar potentials, and generalized tractions, that is mechanical tractions, electric displacement and magnetic induction. The generalized boundary integral representation is deduced by extending the reciprocity theorem to magneto-electro-elasticity problem and the multidomain boundary element technique is employed to achieve the problem solution also for interface cracks in bimaterials. Numerical results are presented focusing on the effects of the magneto-electro-elastic coupling on the crack stress intensity factor.

Introduction

Magneto-electro-elastic materials have been recently proposed as effective for building advanced smart structures having valuable performances with respect to standard actuation materials. They show a wide range of potential applications like active structural control, sensors and actuators. Indeed, magneto-electro-elastic layers could be used in laminates so as to inherently integrate the sensing and actuating functions in the structure [1-5].

These materials demand efficient analysis and design tools to accurately predict the coupling effects of the material and then take full advantage from the smart behavior; this is crucial in presence of damage which can significantly affect the smart structure performances. Exact closed-form solutions for simply supported magneto-electro-elastic laminates have been presented [6, 7, 8]; approximate solutions based on discrete layer models have also been proposed [9, 10]. Green's functions have also been investigated for magneto-electro-elastic solids with inclusions or cracks [11-14]. However, these analytical solutions deals with simple configurations and from this point of view numerical solutions are mandatory. Both the finite element method (e.g. [15]) and the boundary element method [16] have been employed to solve problems involving magneto-electro-elastic materials.

The analysis of crack problems in magneto-electro-elastic media has been classically approached for infinite domains by analytical solutions based on the Sthro's formalism and/or the use of complex potentials theory [17-21]. Nevertheless for complex cracked configurations numerical models need to be used and the boundary element method is very well suited to this subject. Indeed the application of the boundary element approach to the fracture mechanics of cracked smart structures [22, 23] shows the skills of this method to accurately and efficiently assess the coupled field behavior inherent to smart materials.

In the present paper, a boundary element method and its numerical implementation for the analysis of magneto-electro-elastic materials are presented with the aim to exploit their features in linear magneto-electro-elastic fracture mechanics. The multifield problem is formulated employing generalized variables whose corresponding boundary integral representation is obtained by generalizing the reciprocity theorem to magneto-electro-elasticity problem. The multidomain boundary element technique is employed to achieve the problem solution so that complex configurations, multiple cracks and bimaterials interface cracks can be analyzed. Numerical results are presented focusing on the effects of the magneto-electro-elastic coupling on the crack stress intensity factor.

Boundary Integral Formulation and Numerical Model

Let a two-dimensional magneto-electro-elastic domain Ω with boundary $\partial\Omega$ lying in the x_1x_2 plane be

considered. Let us assume the magneto-electro-elastic response does not vary along the x_3 direction, so that the model reduces to a generalized plane strain elasticity problem and an in-plane magneto-electrostatic problem coupled by means of the magneto-electro-elastic constitutive equations. Extending to magneto-electro-elasticity the formalism introduced by Barnett and Lothe [24] for piezoelectrics, the problem governing equations can be expressed in terms of suitable generalized variables. These are: (i) the generalized displacements **U**, whose components are the displacements and the electric and magnetic potentials; (ii) the generalized strains $\boldsymbol{\Gamma}$ which collect the strains and the opposite of the electric and magnetic field components; (iii) the generalized stresses $\boldsymbol{\Sigma}$ collecting the stresses, electric displacements and magnetic induction components; (iv) the generalized boundary tractions **T**, whose components are the boundary tractions and the normal component of the electric displacement and magnetic induction. The governing equations of the problem expressed in terms of generalized variables formally resemble the governing equations of anisotropic elasticity and they can be rearranged to obtain the analogous to the Navier equations for the magneto-electro-elasticity [26].

According to the above-mentioned analogy the boundary integral representation of the magneto-electro-elasticity generalized variables is deduced by generalizing the reciprocity theorem. In the absence of applied body forces and free electric charge density, the boundary integral representation for the generalized displacements U at the point P_0 writes [25, 26]

$$\mathbf{c}^*\mathbf{U}(P_0) + \int_{\partial\Omega} \left(\mathbf{T}^*\mathbf{U} - \mathbf{U}^*\mathbf{T}\right) d\partial\Omega = \mathbf{0} \tag{1}$$

where the kernels $\mathbf{U}^*$ and $\mathbf{T}^*$ are the fundamental solutions matrices whose expressions can be found in [26]. It is worth to not that Eq. (1) holds also for boundary points provided that that the arising kernels singularities are taken into account by processing the integrals as their principal value and by suitably computing the matrix $\mathbf{c}^*$ [26]. When Eq. (1) is collocated at the boundary one obtains the boundary integral equations which, together with the boundary conditions expressed in terms of prescribed generalized displacement and tractions, allow to determine the unknown variables on the boundary.

The model given by the boundary integral equations is numerically solved by the boundary element method implementing the multidomain technique in order to deal with inhomogeneous bodies and cracks which are simulated through dummy interfaces [23, 27]. The multidomain approach expects to suitably subdivide the original domain into *N* sub-regions which are at the start treated as single domains. The boundary $\partial\Omega_{\langle j\rangle}$ of each subregion is discretized by boundary elements over which the generalized boundary variables U and T are expressed in terms of their respective nodal values $\boldsymbol{\Delta}_{\langle j\rangle}$ and $\mathbf{P}_{\langle j\rangle}$ by suitable shape functions, respectively. Collocating the discretized form of Eq. (1) to the boundary nodes, for each subregion one obtains a linear algebraic system, which can be compactly written as [25]

$$\mathbf{H}^{(k)}\boldsymbol{\Delta}^{(k)} + \mathbf{G}^{(k)}\mathbf{P}^{(k)} = \mathbf{0} \qquad k = 1, 2..., N\,. \tag{2}$$

where $\boldsymbol{\Delta}$ is the vector of the nodal values of the generalized displacements, **P** is the vector of the nodal values of the generalized tractions and the superscript (*k*) denotes quantities related to the *k*-th sub-region. By enforcing suitable continuity and equilibrium conditions at the interface between contiguous sub-regions (e.g. perfect bonding interface, elastic interface, contact interface) [23], and by taking the boundary conditions into account, the numerical models of the distinct subregions are coupled together to achieve the problem resolving system. Its solution directly provides the nodal values of generalized displacements and tractions on the domain boundary and along its interfaces. Once these generalized displacements and tractions are determined, the generalized displacements, strain and stresses at the generic domain point can be calculated through their discretized boundary integral representations [26].

Applications and discussion

The analysis of some cracked configurations of magneto-electro-elastic bodies are presented to show the soundness of the approach in terms of accuracy and effectiveness. The material properties employed are those of $BaTiO_3$, $CoFe_2O_4$ and a $BaTiO_3 - CoFe_2O_4$ composite whose values are given in [28]. The analyses have been performed by using linear boundary element and computing the corresponding influence coefficients by an adaptive Gauss quadrature scheme [23].

The case of a finite horizontal crack of length 2*a* in an infinite domain under uniform far-field stresses,

normal electric displacement and magnetic induction has been analyzed. This study was carried out to establish confidence and reliability in the method by comparing the present results with analytic solutions [18]. The infinite domain has been simulated by truncating it into a square having side 20 times the crack length. The analysis has been performed using 86 boundary elements for each of the two subdomains used in the modelization; this discretization scheme has been employed for all the performed applications. The generalized stress intensity factors have been ascertained by extending the displacement correlation method to magneto-electro-elastic fracture mechanics [29]. This approach is founded on the correlation of the computed generalized relative crack displacements with their crack tip asymptotic expression, according to the following relation

$$\Delta\mathbf{U}(d) = \sqrt{\frac{2d}{\pi}}\,\mathbf{Y}\mathbf{K} \tag{3}$$

where $\mathbf{K}$ is the vector of the generalized stress intensity factors, $\Delta\mathbf{U}$ is the vector of the generalized relative crack displacements, d is the distance behind the crack tip and $\mathbf{Y}$ is a material dependent matrix [18]. The normalized generalized stress intensity factors for the different far-field loading conditions are given in Tables 1 and 2 which refer to the conditions of impermeable and fully permeable crack, respectively. The results show the accuracy of the approach and its capability to model different boundary conditions applied along the crack faces. Mixed boundary conditions along the crack faces, e. g. electrically impermeable and magnetically permeable cracks or electrically permeable and magnetically impermeable cracks, are also implemented and the relative results are not given here for the sake of brevity.

Load F	$K_{II}/F\sqrt{\pi a}$	$K_{I}/F\sqrt{\pi a}$	$K_{III}/F\sqrt{\pi a}$	$K_{D}/F\sqrt{\pi a}$	$K_{B}/F\sqrt{\pi a}$
σ_{21}^{∞}	0.994 [1.000]	0.000 [0.000]	0.000 [0.000]	0.000 [0.000]	0.000 [0.000]
σ_{22}^{∞}	0.001 [0.000]	1.000 [1.000]	0.000 [0.000]	0.004 [0.000]	0.040 [0.000]
σ_{23}^{∞}	0.000 [0.000]	0.000 [0.000]	1.001 [1.000]	0.000 [0.000]	0.000 [0.000]
D_{2}^{∞}	0.000 [0.000]	0.000 [0.000]	0.000 [0.000]	1.002 [1.000]	0.001 [0.000]
B_{2}^{∞}	0.000 [0.000]	0.000 [0.000]	0.000 [0.000]	0.000 [0.000]	1.000 [1.000]

Table 1. *Generalized SIFs for horizontal impermeable crack in infinite domain with different load conditions. The values in square bracket are from [18].*

Load F	$K_{II}/F\sqrt{\pi a}$	$K_{I}/F\sqrt{\pi a}$	$K_{III}/F\sqrt{\pi a}$	$K_{D}/F\sqrt{\pi a}$	$K_{B}/F\sqrt{\pi a}$
σ_{21}^{∞}	1.003 [1.000]	0.000 [0.000]	0.000 [0.000]	0.000 [0.000]	0.000 [0.000]
σ_{22}^{∞}	0.001 [0.000]	1.001 [1.000]	0.000 [0.000]	0.158 [0.161]	6.275 [6.294]
σ_{23}^{∞}	0.000 [0.000]	0.000 [0.000]	1.001 [1.000]	0.000 [0.000]	0.000 [0.000]
D_{2}^{∞}	0.000 [0.000]	0.000 [0.000]	0.000 [0.000]	0.001 [0.000]	0.004 [0.000]
B_{2}^{∞}	0.000 [0.000]	0.000 [0.000]	0.000 [0.000]	0.000 [0.000]	0.005 [0.000]

Table 2. *Generalized SIFs for horizontal permeable crack in infinite domain with different load conditions. The*

values in square bracket are from [18].

The second example concerns with two collinear cracks having length 2*a* and distance equal to 4*a*. Both impermeable and permeable crack faces have been considered and the results are compared to the analytical ones presented in reference [18]. The comparison shows the accuracy of the approach in treating multiple cracks.

Load F	$K_{II}/F\sqrt{\pi a}$	$K_{I}/F\sqrt{\pi a}$	$K_{III}/F\sqrt{\pi a}$	$K_{D}/F\sqrt{\pi a}$	$K_{B}/F\sqrt{\pi a}$
σ_{22}^{∞}	(0.001) [0.001] *0.000*	(1.002) (1.002) *1.000*	(0.000) [0.000] *0.000*	(0.003) [0.157] *0.161*	(0.010) [6.282] *6.294*
D_{2}^{∞}	(0.000) [0.000] *0.000*	0.000 [0.000] *0.000*	(0.000) [0.000] *0.000*	1.002 [0.005] *0.000*	0.002 [0.032] *0.000*
B_{2}^{∞}	(0.000) [0.000] *0.000*	0.000 [0.000] *0.000*	(0.000) [0.000] *0.000*	(0.000) [0.000] *0.000*	1.002 [0.005] *0.000*

Table 3. *Generalized SIFs for multiple impermeable cracks in infinite domain with different load conditions. Values in round bracket are for impermeable crack, values in square bracket are for permeable crack and italic values for permeable crack are from [18].*

The proposed approach has been also tested in the analysis of a bimaterial interface crack between a piezoelastic material, namely $BaTiO_3$, and a magnetoelastic material, namely $CoFe_2O_4$. The analysis has been performed with the same discretization employed for the case 1 and the results obtained are shown in Table 4.

Load F	$K_{II}/F\sqrt{\pi a}$	$K_{I}/F\sqrt{\pi a}$	$K_{III}/F\sqrt{\pi a}$	$K_{D}/F\sqrt{\pi a}$	$K_{B}/F\sqrt{\pi a}$
σ_{22}^{∞}	(0.000) [0.000]	(1.005) [1.005]	(0.000) [0.000]	(0.003) [0.152]	(0.047) [6.339]
D_{2}^{∞}	(0.000) [0.000]	(0.000) [0.000]	(0.000) [0.000]	(1.006) [0.006]	(0.069) [0.031]
B_{2}^{∞}	(0.000) [0.000]	(0.000) [0.000]	(0.000) [0.000]	(0.000) [0.000]	(1.005) [0.002]

Table 4. *Generalized SIFs for bimaterial interface crack with different load conditions. Values in round bracket are for impermeable crack, values in square bracket are for permeable crack*

Based on the good results obtained for cracks in infinite domains, the analysis has been extended to cracked finite solids to highlight some features of the magneto-electro-elastic behavior in fracture mechanics. Results for different ratios of crack length to width are presented for a rectangular piezoelectric solid with a central crack having length 2*a*. The ratio between the specimen height and width was fixed to $h/w=1$, respectively. The analysis was performed for the specimen loaded by uniform normal tension, electric displacement and magnetic induction. Table 5 lists the normalized generalized stress intensity factors for the loading conditions considered for both impermeable and permeable crack faces. These analyses have shown the effectiveness of the approach in terms of affordable computational effort related to the generality and accuracy of the method.

Conclusions

A multidomain boundary element approach for the analysis of magneto-electro-elastic solids has been presented with the aim of exploiting its features in magneto-electro-elastic linear fracture mechanics.

The numerical results compared with analytical ones show the capability of the method to accurately assess the behavior of cracked magneto-electro-elastic bodies without assumptions on the crack tip stress and magnetoelectric states.

On this basis, investigations have been performed to calculate the generalized stress intensity factors under different loads and boundary conditions along the crack faces. The obtained results for finite domains seems to confirm (i) the electric and magnetic field intensification at the crack tip under mechanical loads for both impermeable and permeable crack; (ii) the drop off of the electromagnetic intensification at the crack tip for permeable crack under electric and magnetic loads.

	Load F	$K_{II}/F\sqrt{\pi a}$	$K_{I}/F\sqrt{\pi a}$	$K_{III}/F\sqrt{\pi a}$	$K_{D}/F\sqrt{\pi a}$	$K_{B}/F\sqrt{\pi a}$
$a/w=0.2$	σ_{22}^{∞}	(0.000) [0.000]	(1.046) [1.046]	(0.000) [0.000]	(0.000) [0.013]	(0.091) [6.274]
	D_{2}^{∞}	(0.000) [0.000]	(0.000) [1.046]	(0.000) [0.000]	(1.046) [0.024]	(0.090) [0.182]
	B_{2}^{∞}	(0.000) [0.000]	(0.000) [0.000]	(0.000) [0.000]	(0.000) [0.000]	(1.046) [0.000]
$a/w=0.3$	σ_{22}^{∞}	(0.000) [0.000]	(1.098) [1.098]	(0.000) [0.000]	(0.002) [0.014]	(0.231) [6.673]
	D_{2}^{∞}	(0.000) [0.000]	(0.000) [0.000]	(0.000) [0.000]	(1.098) [0.026]	(0.100) [0.203]
	B_{2}^{∞}	(0.000) [0.000]	(0.000) [0.000]	(0.000) [0.000]	(0.000) [0.000]	(1.098) [0.000]
$a/w=0.4$	σ_{22}^{∞}	(0.000) [0.000]	(1.170) [1.170]	(0.000) [0.000]	(0.007) [0.162]	(0.479) [7.172]
	D_{2}^{∞}	(0.000) [0.000]	(0.000) [0.000]	(0.000) [0.000]	(1.170) [0.145]	(0.068) [1.030]
	B_{2}^{∞}	(0.000) [0.000]	(0.000) [0.000]	(0.000) [0.000]	(0.000) [0.000]	(1.170) [0.000]
$a/w=0.5$	σ_{22}^{∞}	(0.000) [0.000]	(1.270) [1.270]	(0.000) [0.000]	(0.015) [0.178]	(0.796) [7.794]
	D_{2}^{∞}	(0.000) [0.000]	(0.000) [0.000]	(0.000) [0.000]	(1.270) [0.133]	(0.049) [0.951]
	B_{2}^{∞}	(0.000) [0.000]	(0.000) [0.000]	(0.000) [0.000]	(0.000) [0.000]	(1.270) [0.003]

Table 5. *Generalized SIFs for horizontal crack in finite plate with different load conditions. Values in round bracket are for impermeable crack whereas values in square bracket are for permeable crack*

References

[1] G. Harsche, J.P. Dougherty and R.E. Newnham *International Journal Applied Electromagnetical Materials*, **4**, 145-159 (1993).

[2] M. Avellaneda and G. Harsche *Journal of Intelligent Material Systems and Structures*, **5**, 501-513 (1994).

[3] C.W. Nan *Physical Review B*, **50**, 6082-6088 (1994).

[4] Y. Benveniste *Physical Review B*, **51**, 424-427 (1995).

[5] J.Y. Li and M.L. Dunn *Journal of Intelligent Material Systems and Structures*, **7**, 404-416 (1998).

[6] E.Pan *Journal of Applied Mechanics*, **68**, 608-618 (2001).

[7] E.Pan and P.R. Heyliger *International Journal of Solids and Structures*, **40**, 6859-6876 (2003).

[8] E.Pan and P.R. Heyliger *Journal of Sound and Vibrations*, **252**, 429-442 (2002).

[9] P.R. Heyliger and E.Pan *AIAA Journal*, **42**, 1435-1443 (2004).

[10] P.R. Heyliger, F. Ramirez and E.Pan *Journal of Intelligent Material Systems and Structures*, **15**, 689-709 (2004).

[11] J.Y. Li *International Journal of Engineering Science*, **38**, 1993-2011 (2000).

[12] L. Jinxi, L. Xianglin and Z. Yongbin *International Journal of Engineering Science*, **39**, 1405-1418 (2001).

[13] E. Pan *Z Angew Math. Phys*, **53**, 815-838 (2002)

[14] Q.H. Qin *Engineering Analysis with Boundary Elements*, **29**, 577-585 (2005).

[15] R. Garcia Lage, C.M. Mota Soares, C.A. Mota Soares and J.N. Reddy *Computers and Structures*, **82**, 1293-1301 (2005).

[16] D. Haojiang and J. Aimin *Computers and Structures*, **82**, 1599-1607 (2004)

[17] Z.F. Song and G.C. Sih *Theoretical and Applied Fracture Mechanics*, **39**, 189-207 (2003).

[18] C.F. Gao, H. Kessler and H. Balke *International Journal of Engineering Science*, **41**, 969-994 (2003).

[19] B.L. Wang and Y.W. Mai *European Journal of Mechanics A/Solids*, **22**, 591-602 (2003).

[20] B.L. Wang and Y.W. Mai *Mechanics Research Communications*, **31**, 65-73 (2004).

[21] K.Q. Hu, G.Q. Li and Z. Zhong *Mechanics Research Communications*, **33**, 482-492 (2006).

[22] E. Pan *Engineering Analysis with Boundary Elements*, **23**, 67-76 (1999).

[23] G. Davì and A. Milazzo *International Journal of Solids and Structures*, **38**, 7065-7078 (2001).

[24] D.M. Barnett and J. Lothe *Phys. Stat Sol(b)*, **67**, 105-111 (1975).

[25] M. H. Aliabadi, *The Boundary Element Method, Vol.2 Application in Solids and Structures*, Wiley, 2002.

[26] A. Milazzo, I. Benedetti and C. Orlando *Computer Modeling in Engineering and Science*, **15**, 17-30 (2006).

[27] M.H. Aliabadi *Applied Mechanics Review*, **50**, 83-96 (1997).

[28] B. Wang and J. Han *Acta Mechanica Sinica*, **22**, 233-242 (2006).

[29] Z. Suo, C.M. Kuo, D.M. Barnett and J.R. Willis *Journal of Mechanics and Physics of Solids*, **50**, 739-765 (1992).

Local versus non-local boundary conditions for the BEM in acoustics

Stefan Schneider
CNRS-LMA, 31 chemin Joseph-Aiguier 13402 Marseille cedex 20, France
e-mail: schneider@lma.cnrs-mrs.fr

Keywords: Absorbing materials, fast boundary element methods, non-local boundary conditions

Abstract

To influence the acoustical characteristics of enclosures or to reduce noise pollution often walls are equipped with sound absorbing materials. To predict their effects using numerical models based on the boundary element method, these models must take into account for the treatment of the walls by the means of a boundary condition. In general this is done by using a surface impedance or admittance condition to couple sound pressure and velocity at a point on the surface.
Modelling the absorbing material using the Biot-theory reveals that using a local surface impedance or admittance condition is inaccurate under certain conditions. Nevertheless, the complete model of the absorbing material is far too expensive from a numerical point of view. Therefore, in the paper we study possible extensions of the model of a local boundary condition by finding a compromise between accurate prediction given by the complete model and efficiency of the resulting numerical model. Such an extension was found to be necessary to describe correctly the acoustical behaviour of complex shaped acoustic linings in the low frequency range. The results of the study will be used to represent the acoustic lining of an anechoic chamber by a special boundary condition. This new boundary condition will then be used to simulate the acoustical behaviour of an anechoic chamber. To evaluate the quality of the developed boundary condition numerical results are compared with experimental data.

1 Introduction

To reduce noise pollution in urban areas or to influence the acoustical characteristics of enclosures often walls are equipped with sound absorbing materials. To predict their effects the acoustic treatment of the walls must be taken into account for in an appropriated way. In a numerical model the presents of the acoustic lining is in general represented by the means of a boundary condition at the air/lining interface Γ_Y without modelling the absorbing material itself. In the most general form this boundary condition can be expressed in the form

$$v_\nu(x) = Y(x,y)p(y) \quad \forall\, x,y \in \Gamma_Y\,. \tag{1}$$

In this form the normal fluid velocity v_ν at a single point $x \in \Gamma_Y$ is linked to the sound pressure p at all points on the air/lining interface Γ_Y via the function $Y(x,y)$ often referred to as acoustic admittance. It is pointed out that the function $Y(x,y)$ can be complex valued and frequency dependent. Using the above relation enables to replace the unknown surface velocity v_ν appearing in the surface integrals of the weak formulation of the time harmonic Helmholtz equation. Thereafter, the sound pressure p is the only unknown for a numerical solution of the corresponding equations.

The present study compares two different numerical models to take into account for the acoustic lining of an anechoic chamber in the 20 to 200 Hz frequency range using the boundary element method. This specifically low frequency range is typical for anechoic chambers as the applied acoustic treatment is of significant thickness –.5 to 1.5 m– unusual for applications in field of reduction of noise pollution in urban areas. However, results of the present study are applicable to acoustic linings of a common thickness when considering a corresponding higher frequency range.
The original objective of the numerical analysis was the prediction of the 1.5 dB region of an anechoic chamber either based on experimental data obtained from an impedance tube experiment carried out on a sample of the lining or, even more general, based on the knowledge of the acoustical properties of the material where the lining will be made from. Hence, the prediction of the quality of a future anechoic chamber in its planning stage. Experimental data obtained from measurements carried out in the large anechoic chamber of the Laboratoire de Mécanique et d'Acoustique (LMA) serve as reference to judge the quality of the different numerical models.
The paper is organized as follows. Section two studies the performance of the often applied model of a local admittance. In section three a surface admittance obtained by the localisation of a non-local surface admittance is studied.

2 Model of a local admittance condition for an absorbing layer

The most common geometry model of an enclosure, used for a numerical prediction of the effect of an acoustic treatment, is the model of a more or less rectangular cavity. In such a model the real geometry of the acoustic lining is replaced by a flat surface. The latter is equipped with an appropriated surface admittance to take into account for the behavior of the applied acoustic treatment. The advantage of such a model is twofold. First, this simple geometry is easy to handle using either FEM, BEM or the image source model. Secondly, easily available results of an impedance tube experiment are

often used to derive the required surface condition. However, the fact that this measured value is valid only for normal incident of plane waves is often neglected.
The quality of such a simple model will be studied based on the experimental data obtained from measurements carried out in the large anechoic chamber of the LMA. The 1.5 dB region in the 20 to 200 Hz frequency range was obtained by measuring the sound pressure radiated by a bass-reflex box. For a detailed description of the experiment we refer to [12]. Out of the measured sound pressure p_{exp} and the sound pressure p_{inc} generated by the sound source the deviation from free-field conditions of the chamber was calculated as

$$L_{\mathrm{p}}(x) = 20 \log \left(\left| \frac{p_{\mathrm{exp}}(x)}{p_{\mathrm{inc}}(x)} \right| \right) . \tag{2}$$

The maximum allowed difference between the measured and theoretical free-field levels according to ISO 3745 and ANSI S12.35 is ± 1.5 dB at frequencies lower than 630 Hz. A region where the difference is smaller than the required ± 1.5 dB will be called the 1.5 dB region. The size of this region may depend on the frequency and the location of the acoustic source in the chamber. The upper left sub-figure of Fig. (1) and Fig. (2) show this 1.5 dB region in the large anechoic chamber at the LMA for two different positions of the sound source. Blank areas indicate regions not belonging to the 1.5 dB region.
The simple model of a rectangular cavity with the walls equipped with a local admittance condition will be used to predict the measured 1.5 dB regions of the anechoic chamber. Three different surface admittance values were used to represent

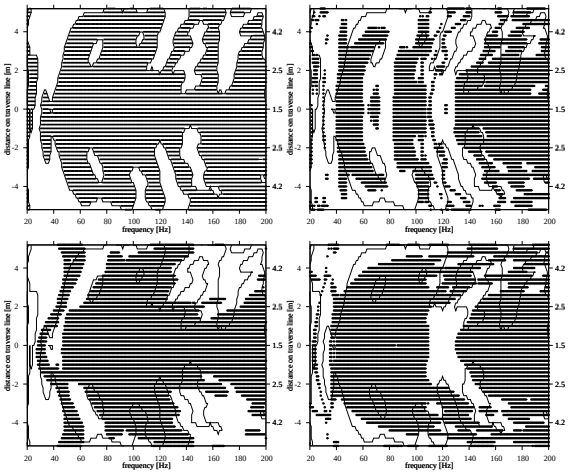

Figure 1: Measured 1.5 dB region of the large anechoic chamber of the LMA (upper left sub-figure) and 1.5 dB region obtained using numerical simulation with different local surface admittances. Upper right sub-figure, admittance obtained from numerical simulation. Lower left sub-figure, admittance obtained from results of an impedance tube experiment and lower right sub-figure, real valued admittance from numerical simulation. Sound source place in the center of the chamber.

the behavior of the acoustic lining of the large anechoic chamber of the LMA:

1. a surface admittance measured in the large impedance tube of the LMA for a 4×4 sample of wedges of the acoustic lining. Wedges were placed in the tube without any additional fixation. In the anechoic chamber wedges are held in place by an iron wire frame.

2. Surface admittance obtained from numerical simulation of an impedance tube experiment taking into account for the mounting conditions of the wedges as present in the anechoic chamber. Numerical simulation was found to be necessary as the specific configuration, wedges held in place by an iron wire frame, could not have been analysed using the experimental facilities available at the LMA.

3. Surface admittance calculated via

$$Y = \frac{1}{\varrho c} \frac{1 - \sqrt{1-\alpha}}{1 + \sqrt{1-\alpha}} \tag{3}$$

out of the absorption coefficient α obtained from the numerical experiment. This reflects the situation that often only the absorption coefficient of a material is communicated by manufacturers.

Sound propagation in the chamber was modelled using the boundary element method. Results of the numerical simulation are compared in Fig. (1) and Fig. (2) with the experimental data obtained for two different positions of the sound source.

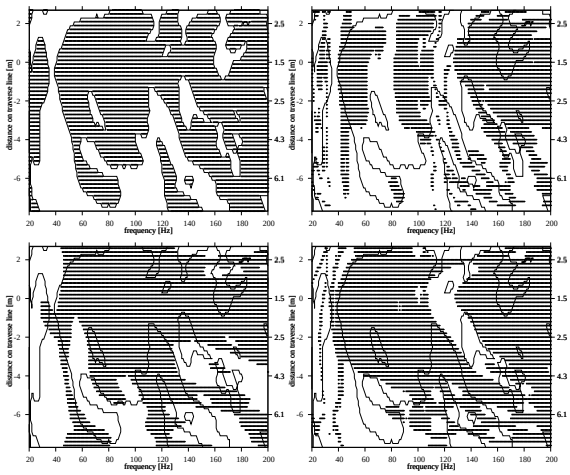

Figure 2: Measured 1.5 dB region of the large anechoic chamber of the LMA (upper left sub-figure) and 1.5 dB region obtained using numerical simulation with different local surface admittances. Upper right sub-figure, admittance obtained from numerical simulation. Lower left sub-figure, admittance obtained from results of an impedance tube experiment and lower right sub-figure, real valued admittance from numerical simulation. Sound source place at a eccentric position in the chamber.

The model of a local admittance condition fails to predict the chambers quality for frequencies lower than 150 Hz regardless the applied admittance. In this frequency range sound propagation in the absorbing material cannot be neglected as it is done when assuming a local admittance. Surface admittance 2 and 3 gave acceptable results for frequencies higher than 150 Hz. It is pointed out that the real valued admittance 3 does overestimate the absorption of the material. This is caused by the fact that eq (3) always leads to $\varrho c Y \leq 1$ what does not reflect most material's behaviour especially at low frequencies. Surface admittance 1 does not reflect the behavior of the acoustic lining in the chamber. This failure may be attributable to the fact that the mounting conditions of the lining in the anechoic chamber, did not have been taken into account for when carrying out the experiment in the impedance tube. This shows the significant influence of the mounting conditions on the performance of an acoustic treatment.

3 Model of a localised admittance condition for an absorbing layer

In the previous section it has been shown that the model of a local surface admittance cannot be used to predict the effect of the acoustic lining of an anechoic chamber for frequencies lower than 150 Hz. This was due to the fact that sound propagation in the absorbing material has been neglected. A numerical method is now presented that take into account for –at least partly– the effect of sound propagation in the absorbing layer. The new boundary condition enables to extent the frequency range where the effect of acoustical treatments of objects can be predicted numerically in the planing stage.

The following situation is considered. Sound propagation within the fluid domain Ω_{F} is of interest. The domain Ω_{F} has a common boundary Γ_{Y} with a second domain Ω_{B} occupied by an absorbing material. Sound propagation in Ω_{B} is modelled using the equivalent fluid or the Biot model together with a finite element method. The influence of the presents of the domain Ω_{B} on sound propagation in Ω_{F} is to be studied, but sound propagation in Ω_{B} is of subordinate importance. Under these prevailing circumstance the following relation between the vector of the nodal sound pressures $p^{\Gamma_{\mathrm{Y}}}$ and the nodal normal surface velocities $v_\nu^{\Gamma_{\mathrm{Y}}}$ on the common boundary Γ_{Y}

$$p^{\Gamma_{\mathrm{Y}}} = Z(\omega) v_\nu^{\Gamma_{\mathrm{Y}}} \tag{4}$$

can be established. The dense and frequency dependent matrix $Z(\omega)$ represents a non-local impedance condition on the boundary $\Gamma_{\rm Y}$. After a possible regularisation the matrix Z can be inverted to obtain a relation as in eq (1). Except for special cases where the discretization of $\Omega_{\rm B}$ leads only to a moderate number of unknowns, for example a small absorbing object embedded in an acoustic fluid, the numerical evaluation of $Z(\omega)$ in eq (4) is far too expensive. Hence a suitable truncation of that matrix is to be found. Here the following strategy is suggested. Representing the sound pressure $p^{\Gamma_{\rm Y}}$ by the use of the basis functions φ_i used for the discretisation of the sound pressure in $\Omega_{\rm F}$ yields

$$v_\nu^{\Gamma_{\rm Y}} = Y p^{\Gamma_{\rm Y}} = Y \sum_i \beta_i \varphi_i = \sum_i \beta_i Y^i \varphi_i \tag{5}$$

where Y^i denotes the restriction of Y to the support of the basis function φ_i. It is pointed out that the discretisation of $\Omega_{\rm B}$ and $\Omega_{\rm F}$ may be different. If the domain $\Omega_{\rm B}$ possesses a periodic geometry then with a proper choice of the basis functions all matrices Y^i are identical. However, the matrix Y^i still couples the basis function φ_i to all points on $\Gamma_{\rm Y}$ and is thus still a non-local coupling condition. A localisation of this non-local behavior can be achieved by neglecting entries of the vector $v_\nu^{\Gamma_{\rm Y}}$ that correspond to points that are far away from the support of φ_i. That is keeping only the first $n_{\rm T}$ rows of Y^i

$$v_\nu^{\Gamma_{\rm Y}}(\varphi_i) \approx \begin{bmatrix} {v_\nu^{\Gamma_{\rm Y}}}_i \\ 0 \end{bmatrix} = \begin{bmatrix} Y^i_{<1:n_{\rm T},:>} \\ 0 \end{bmatrix} \beta_i \varphi_i = Y^i_{n_{\rm T}} \beta_i \varphi_i \tag{6}$$

and assuming that the discarded velocity components are of minor importance. The rows of Y^i are supposed to be ordered such that the first $n_{\rm T}$ rows correspond to the points the closest to the support of φ_i. The quality of the proposed localization highly depends on the behavior of the absorbing material in the frequency range of interest. The more the material is absorbing the smaller $n_{\rm T}$ can be chosen as sound propagation in the material is less relevant. Thus the value of $n_{\rm T}$ where the matrix is truncated determines the accuracy of the approximation but also the numerical costs. A measure for the truncation error depending on a specific incident sound field can be defined as follows

$$\varepsilon^{n_{\rm T}}(p_{\rm inc}) = \frac{\|(Y^i - Y^i_{n_{\rm T}}) p_{\rm inc}\|}{\|Y^i p_{\rm inc}\|} \,. \tag{7}$$

The dependency of the error measure on a certain sound field has been introduced to account for the type of application we have in mind. At low frequencies the sound field in an enclosure is not arbitrary. In general it can be represented –or at least approximated with a sufficient accuracy– using a set of monopole sound sources. Therefore, a set of monopole sources placed at a certain distance from the support of the basis functions φ_i can be used to generated a sound field that is fairly similar to that of the real application.

The quality of the presented localisation of the non-local admittance condition has been tested using two different materials. Material A is a polyester fibrous material used to manufacture acoustic linings of anechoic chambers. The acoustic parameters as given in [8] have been used. The second material is the melamine foam used as acoustic lining in the anechoic chamber of the LMA. Both sets of parameters are given in Table (1). To model the melamine foam the Biot model [2, 3, 6, 4, 1] has been used, whereas material A was modelled using the equivalent fluid model as proposed in [8]. Each

material	Young's module E [N/m^2]	Poisson ratio ν	density ϱ [kg/m^3]	flow resistivity σ [Ns/m^4]	porosity Φ	tortuosity α_∞	characteristic dimensions Λ [m]	Λ' [m]
melamine	.16e+6	.44	8.35	1.2e4	.99	1.0	.8e-4	.28e-3
Material A	-	-	-	3.0e3	.98	1.0	.2e-3	.3e-3

Table 1: Material parameters of the melamine foam and material A.

of the individual elements of the acoustic lining consists of a base of .3×.3 m^2 and .4 m in length and a tapering section of .7 m in length. An array of 7×7 and 9×9 wedges for material A and an array 5×5 and 7×7 wedges for the melamine foam were used for numerical simulations. The incident sound pressure was applied to the central wedge of the arrays. The error as defined in eq (7) is shown in Fig. (3) for the two materials. For material A, even when truncating the vector $v_\nu^{\Gamma_{\rm Y}}$ after the central wedge ($n_{\rm T}$ =1), the error according to eq (7) is less than 50%. Taking into account also for the adjacent wedges the error drops down to less than 10%. In addition the error is almost independent on the total size of the array as results for the array of 7×7 and 9×9 wedges are almost undistiguishible. The situation is less favorable for the melamine foam. To have the truncation error smaller than 50% over the entire frequency range at least the two adjacent layers of wedges must be used. However, for frequencies higher than ≈100 Hz using only the adjacent layer of wedges results in a truncation error less than 50%. The domaine $\Omega_{\rm B}$ which is used to evalutate Z in eq (4) has been truncated according to $n_{\rm T}$. This must be seen as compromise between numerical efficiency and accuracy. For frequencies lower than 100 Hz the non-local

behavior of the material cannot be neglected and the fully coupled fluid/structure–interaction problem must be considered.

The proposed localized admittance condition was used to predict the 1.5 dB region of the large anechoic chamber of the LMA. In contrast to Sec. (2) now the real geometry of the lining will be taken into account. The lining consists of 3720 melamine wedges as described above. As all of the wedges are identical only a single matrix $Y^i_{n_\mathrm{T}}$ is needed. However, to take into account for the anisotropy of the melamine foam three different matrices $Y^i_{n_\mathrm{T}}$, representing the three different material orientations, have actually been used. They were precalculated in the frequency range of 20 to 200 Hz with a frequency resolution of 1 Hz using a finite element method. To avoid meshing the domain Ω_F, with its complex shape caused by the geometry of the acoustic lining, the boundary element method has been used for the numerical simulation. Hence the total sound pressure $p = p_\mathrm{inc} + p_\mathrm{scat}$ within the chamber was obtained solving

$$p(y) + \int_{\Gamma_\mathrm{F}} \frac{\partial \phi(x,y)}{\partial \nu} p(x)\, d\Gamma_\mathrm{F} - a \int_{\Gamma_\mathrm{F}} \phi(x,y) Y p(x)\, d\Gamma_\mathrm{F} = p_\mathrm{inc}(y) + \int_{\Gamma_\mathrm{F}} \frac{\partial \phi(x,y)}{\partial \nu} p_\mathrm{inc}(x)\, d\Gamma_\mathrm{F} - a \int_{\Gamma_\mathrm{F}} \phi(x,y) \frac{\partial p_\mathrm{inc}}{\partial \nu}\, d\Gamma_\mathrm{F} \quad (8)$$

with p_inc the incident and p_scat the scattered sound field and the matrix $Y(\omega) \in \mathbb{C}^{324\times 36}$. Each of the wedges has been modelled using 9 elements resulting in a mesh size of .3 m. Linear discontinuous basis functions [7] together with a multilevel fast multipole [10, 9, 5] accelerated collocation method have been used. The linear system with N=138280 unknowns was solved using the GMRes [11] solver. Depending on frequency 80...120 iterations were necessary to obtain a residual of $\varepsilon = 1.e-6$. The total solution time was 2.5...4 hours per frequency on a SGI Origin3800 of the Center for Information Services and High Performance Computing of the Technische Universität Dresden, Germany. Numerical results are compared with experimental data in Fig. (4) for two different source positions. A solid dot represents the numerical result. The bounds of the 1.5 dB region obtained from experimental data are represented by a solid line. For both source positions numerical and experimental results agree well for frequencies higher than 100 Hz. But even below that frequency accuracy is better than indicated by the error measure eq (7).

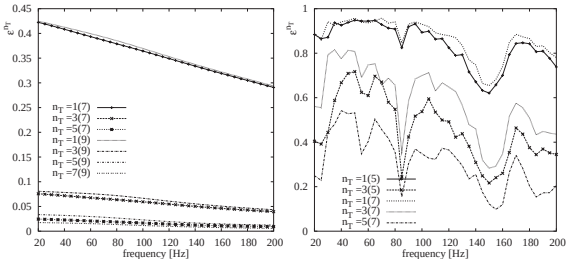

Figure 3: Truncation error eq (7) for different values of n_T. The given values for n_T represent the size of the truncated array and the numbers in brackets give the total size of the array. Left sub-figure material A and right sub-figure melamine.

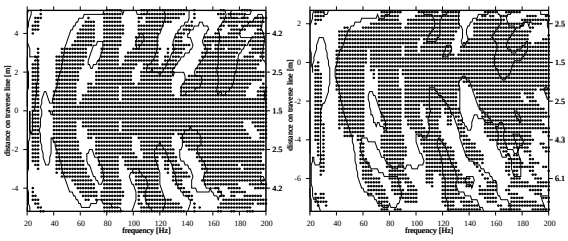

Figure 4: 1.5 dB regions for two source positions in the chamber obtained using numerical simulations with the localized surface admittance.

Conclusion

It has been shown that at low frequencies the presents of sound absorbing materials cannot be modelled using a local surface admittance. This is due to the fact that at low frequencies the material is not sufficiently absorbing such that sound propagation within the absorbing material can not be neglected. Taking into account for these propagation effects in the vicinity of an observation point leads to an admittance matrix instead of a scalar admittance. This localised boundary condition can be used in a boundary element context with nearly no extra numerical costs. But this new type of boundary condition enables a reliable numerical prediction of the effect of the acoustical treatment in the low frequency range. Furthermore, a measure has been proposed that can be used to determine what kind of boundary condition must be applied depending on the frequency range and the acoustical and geometrical properties of the acoustic treatment.

Acknowledgments

The author was financed by a grant from the "Deutsche Forschungsgemeinschaft". Numerical simulations were run on a SGI Origin3800 at the Center for Information Services and High Performance Computing at the Technische Universität Dresden, Germany. The author likes to thank C. Kern who made available the experimental data of the anechoic chamber.

References

[1] N. Atalla, R. Panneton, and P. Deberge. A mixed pressure-displacement formulation for poroelastic materials. *Journal of the Acoustical Society of America*, 104(3):1444–1542, 1998.

[2] M. A. Biot. Theory of propagation of elastic waves in a fluid-saturated porous solid. I. low-frequency range. *Journal of the Acoustical Society of America*, 28(2):168–178, 1956.

[3] M. A. Biot. Theory of propagation of elastic waves in a fluid-saturated porous solid. II. higher frequency range. *Journal of the Acoustical Society of America*, 28(2):179–191, 1956.

[4] J.-F. Champoux, Y. Allard. Dynamic tortuosity and bulk modulus in air-saturated porous media. *Journal of Applied Physics*, 70(4):1975–1979, 1991.

[5] E. Darve. The fast multipole method I: Error analysis and asymptotic complexity. *SIAM Journal on Numerical Analysis*, 38(1):98–128, Feb. 2001.

[6] D. Johnson, J. Koplik, and R. Dashen. Theory of dynamic permeability and tortuosity in fluid-saturated porous media. *Journal of Fluid Mechanics*, 176:379–401, 1987.

[7] S. Marburg and S. Schneider. Influence of element types on numeric error for acoustic boundary elements. *Journal of Computational Acoustics*, 11(3):363–386, 2003.

[8] X. Olny. Acoustical properties of multiscales absorbing porous materials. In *Proceedings of Sapem 2005*, pages 273–286, ENTPE Lyon, 2005. CD.

[9] J. Rahola. Diagonal Forms of the Translation Operators in the Fast Multipole Algorithm for Scattering Problems. *BIT*, 60(2):333–358, 1996.

[10] V. Rokhlin. Diagonal Forms of the Translation Operators for the Helmholtz Equation in Three Dimensions. *Applied and Computational Harmonic Analysis*, 1:82–93, 1993.

[11] Y. Saad and M. H. Schultz. GMRES: a generalized minimal residual algorithm for solving nonsymmetric linear systems. *SIAM Journal on Scientific and Statistical Computing*, 7(3):856–869, 1986.

[12] S. Schneider, C. Kern, and H.-J. Hardtke. Characterization of the large anechoic chamber of the Laboratoire de Mécanique et d'Acoustique. *Journal of the Acoustical Society of America*, 2006. submitted for publication.